The Ionocraft: Flying Microrobots With No Moving Parts

Daniel Drew

Electrical Engineering and Computer Sciences
University of California at Berkeley

Technical Report No. UCB/EECS-2018-164
http://www2.eecs.berkeley.edu/Pubs/TechRpts/2018/EECS-2018-164.html

December 10, 2018

The Ionocraft: Flying Microrobots With No Moving Parts

by

Daniel S. Drew

A dissertation submitted in partial satisfaction of the

requirements for the degree of

Doctor of Philosophy

in

Engineering - Electrical Engineering and Computer Sciences

in the

Graduate Division

of the

University of California, Berkeley

Committee in charge:

Professor Kristofer S. J. Pister, Chair
Professor Michel Maharbiz
Professor Liwei Lin

Fall 2018

The Ionocraft: Flying Microrobots With No Moving Parts

Abstract

The Ionocraft: Flying Microrobots With No Moving Parts

by

Daniel S. Drew

Doctor of Philosophy in Engineering - Electrical Engineering and Computer Sciences

University of California, Berkeley

Professor Kristofer S. J. Pister, Chair

Enabling a future full of insect-scale robots will require progress on a huge number of fronts, one of which is the development of mobility platforms designed to operate beyond the scaling frontier of commercially available solutions. The vast majority of researchers seeking to create functional centimeter-scale flying robots have turned towards biomimetic propulsion mechanisms, specifically flapping wings. In this work I take a very different tack, investigating a propulsion mechanism with no natural analogue — electrohydrodynamic thrust.

Electrohydrodynamics (EHD), specifically in the context of corona discharge based systems, has been a long studied and, until relatively recently, often poorly understood phenomenon. The beginning of this dissertation focuses on the theoretical underpinnings of the thrust mechanism. The bulk of my work has focused on developing proof of concept demonstrators for EHD at the meso-scale. Starting with rapidly prototyped materials and quickly moving to microfabricated electrodes, a series of prototypes elucidate the potential for EHD to yield high thrust-to-weight ratio fliers. Initial demonstrations have been backed up by more rigorous investigations of electrode geometric and density effects.

Quadrotor systems begin to suffer from decreased performance at and below the centimeter scale, especially with regards to increasing demands on durability of rotory components (which may not exist at scale), efficiency of available DC motors, and propeller figures of merit [64]. Simply replacing the rotors with EHD thrusters, however, allows us to sidestep some of the unfavorable scaling laws of propeller-based propulsion while maintaining the ability to transfer domain knowledge from the rich world of quadcopter design and control. Demonstrating repeatable takeoff and rudimentary (open-loop) attitude control is trivial with external power supplied to the simple quad-thruster design. Through a combination of design and methodology (e.g., with regards to assembly) improvements, functional EHD-based "ionocraft" can now be built in about half an hour, with near 100% success rate. Controlled flight is now within reach.

Merely hovering with tethered power and an off-board controller is only the beginning. The final sections of this work outline a variety of paths forward, towards better performance

of a meso-scale ionocraft, autonomous operation, and further miniaturization. Ultimately, I believe the future is bright for ionocraft. While electrohydrodynamics may not be the most power efficient mechanism, nor the easiest to grasp conceptually, it is certainly the simplest to design; put two asymmetric electrodes close to eachother, apply a high voltage, and away it goes! In the words of a respected professor, how hard could it be?

To all the amazing people who have entered my life these past six years, and those from before who have supported me from afar

Contents

List of Figures

List of Tables

Acknowledgments

I chose to attend Berkeley for graduate school largely because, even during visit day, there was a palpable air of enthusiasm, camaraderie, and excitement during the various events. It didn't let me down.

Since the first day walking up the fire trails talking about Sandkings, Kris Pister has been an inspiration. You have taught me how to chase dreams while playing the game just right. Maybe you didn't realize it, but your evident confidence in me as I became a more senior researcher was very important to me. This is not the end; let's write some science fiction ("grants") together.

Bjoern Hartmann, my unofficial co-advisor, was instrumental to my success. Thanks for giving me a different perspective and pushing me towards excellence in my writing and editing process. Your class, and our subsequent research together, have changed my career and my life.

Emily Marron, you have been the greatest force of good in my life I ever could have imagined. Your empathy, patience, and humor are incredible. I could not imagine these past years without you and could not imagine taking the next steps with anyone else; I love you.

My parents, Terry and Scott Drew. Thank you for being my constant champions. I couldn't ask for more supportive sources of unconditional love. Thank you to my sisters, Lauren and Samantha, for being such sources of joy for our parents and for keeping me on my toes.

Joey Greenspun, you're the brother I never had; we are alike enough to have fun and work well together, different enough to push each other (and get on each others nerves) in just the right way. Thank you for being there for me through this whole thing, from visit day hosting to graduation, and almost every big adventure in between.

Thanks to all the members of the Pister lab. I feel honored to have been among you these years; there aren't many places you can be surrounded by such intelligent, pleasant coworkers. To the older students - thank you for charting a course through, at times, uncertain waters. To the younger ones - thank you for keeping things fresh and forcing me to be a better, more patient, mentor.

Friends and loved ones like Riley, Yukiko, Dan Crankshaw, Michelle, Galen, Kathleen and Mike Marron, Corin, Alicia, thank you for making me feel loved and supported through these years. Thanks for all the good times we have had together.

To the stalwart adventurers of Varisia; thank you for your companionship through the years of struggle to prevent the return of Karzoug. We had lots of laughs, beer, and pizza together. I am so grateful to have friends who could have fun flexing their imaginations with me.

To the members, old and new, of Playa Circuit Boogie; thank you for keeping that part of my life a source of excitement and wonder. Let's keep getting dusty.

I can't name everyone who has made an impact on my life through these years. Honestly, I have never before been surrounded by so many people I truly respect, appreciate, and *like*. Thanks to all of you.

Chapter 1

Introduction

1.1 A Future Full of Microrobots

Motivation

With the inception of the internet, inter-personal communication was changed forever. Now, both information and social engagement can be shared and explored at will, subject only to the ever-spreading availability of network connections. The incredible advances of the semiconductor and electronics industries brought the size of an equivalent computer from a building, to a room, to a desk, to a box of tissues, to a deck of cards, in a remarkably short amount of time. But the smartphone did more than just increase internet usage; it put incredible computing power, and versatile integrated sensors, in every pocket, opening a huge new space of applications just by virtue of it being *with* us. Now, spreading connectivity to the things that *surround* us— objects, rooms, clothing — is the dream of the Internet of Things, which has taken almost every market sector by storm.

All of these advancements have come short of fulfilling the true dream of the Internet; a whole world, indelibly and effortlessly connected. Despite it being increasingly difficult to imagine a world without connected objects and environs, the digital world and our access to it remains almost entirely mediated by the glass windows in our pockets. Since Kris Pister's "Smart Dust," the tantalizing image of ubiquitous, distributed sensing and actuation has floated just out of reach despite major academic and commercial interest, largely supplanted in recent years by a (in my opinion, regressive) march towards embedding computers into consumer products. By shoving the internet into a wine bottle we tie ourselves to it and other locii, increasing specificity of our connections while relying more and more on obtuse statistical methods to extract generality from whatever meager trickles of data we can (or are allowed to) siphon; we instead can dream of a future where the *user* possesses the power to extract information from the world around them at will.

I believe that one of the greatest barriers to realization of "Smart Dust" was over-reliance on static nodes. Paradoxically, it seems that some major industrial sectors (e.g. oil and gas) have actually been at the vanguard of implementing the systems that may move us closer

to the greater dream of wireless sensor networks. Research has been focused on increasing "autonomy" through efficiency, either delaying the inevitable replacement of batteries or compromising functionality until they can function with fully harvested energy. A human is typically still required for installation, maintenance, and even data retrieval. Efficiency of this cycle is largely tied to the application environment; a mote deployed indoors may not harvest energy the same as one outside. Being forced to train and employ human operators for these networks (as well as the relatively high unit cost) has led to relatively few implementations — and those that do exist are relatively sparse. A technology that could deploy itself, maintain and reconfigure itself, and add a physical traffic layer to its data transmission would make a huge change in the current economic calculus.

Mobile sensing and actuation platforms already exist; they're called robots. Development of both fully autonomous and semi-autonomous robots is an active research topic being explored for a huge variety of applications. The majority of robotics research, however, has a vision somewhat orthogonal to that of "Smart Dust." In a quest to make ever more functional robots capable of performing all the myriad of tasks currently performed by humans, researchers have packed more and more system components into platforms expanding in size, complexity, and cost. A ubiquitous platform, however, will need to be small enough to be placed unobtrusively, inexpensive enough to be purchased in enormous quantities, and both simple and versatile enough to be easily deployed across a large swath of potential scenarios. Luckily, nature has provided a blueprint for such a system.

Besides micro-organisms, the most successful story of life on Earth may be from the insects. The estimated 17 quintillion insects alive at any time is a number that boggles the mind. Although an individual ant may only have around 250,000 neurons, supercolonies of over 300 million individuals are not uncommon; this collective intelligence would contain over 75 trillion total neurons, compared to the around 100 billion in a human brain. Insects have a variety of amazing sensing capabilities, including reliably detecting specific chemicals and visual cues at astounding distances, decoding visual and sonic messages from their neighbors, and reading ambient airflow to feel a predator coming before they can see them [75, 88, 60]. Insects can work together to build structures tens of thousands of times larger than themselves, form bridges and rafts out of their own bodies, and work together to collectively transport objects hundreds of times their own weight [35]. Clearly, there is the possibility for incredible functionality at the centimeter scale; what challenges do we face in getting there?

Sensor miniaturization has been progressing for decades, with significant gains made largely through the success of MEMS and continued progress in CMOS. Chip-scale inertial measurement units, microphones, and cameras can all be found with impressive functionality for their size and cost. Modern system-on-chip (SoC) integrated circuits combine digital logic with wireless transceivers in small, affordable packages. Low-power embedded networking architectures now exist to make the most of the limited battery life of autonomous motes. Despite all this, developing centimeter- and millimeter- scale actuation capabilities remains a significant challenge. Resource scarcity at the centimeter scale complicates things further; many robotic control algorithms are prohibitively expensive in terms of both computation and power for a centimeter scale SoC and battery, and there is no budget for either dedicated

navigational sensors or inefficient actuation schemes. Ultimately, the core challenge of developing an insect-scale robot is one of systems engineering; every piece must be streamlined and multifunctional, with minimal overhead. This makes every prospective implementation walk a fine line between functionality and versatility. Even optimistic views on what is achievable with current technology put a centimeter-scale autonomous robot just at the bleeding edge of what is possible — and that's part of what makes it such an interesting problem.

Arguments for Scale

The most common question raised when discussing microrobots is – "why bother making them so small?" While few question the massive impact robotics stands to make across every aspect of our lives, it seems to be moving along just fine without devoting such a significant amount of effort to miniaturization. I think that answering this question well (and succinctly) is both *extremely important* to the future of the field of microrobotics as well as *extremely difficult*.

I believe that there are at least three different directions to formulate an answer from — the following are Properties of Microbots:

Well-suited for applications where wide area dispersion and/or data granularity are key. While modern drones can fly autonomously and can carry a sizable suite of sensors, they can still only be in one place at a time, and commercial work has largely focused on single-drone deployments. For example, state of the art precision agriculture practice typically involves flying a single drone through the farm over the course of a day, then stitching together and analyzing the data offline; this will be repeated only a handful (e.g. three) times a year. A swarm of artificial insects dispersed throughout the farm, persistently monitoring conditions in real-time at the individual row or even individual plant level, could afford unique opportunities for pest and disease control as well as extremely precise nutrient delivery.

A small form factor confers specific advantages for certain applications. Consider the use of microrobots for search and rescue operations. Besides the advantage of wide area dispersion from large numbers of agents, there is the additional benefit of being able to more easily maneuver in tight or crowded environments due to scale; a robotic cockroach would be much better suited for exploring a collapsed building than a humanoid biped.

Low unit cost through batch fabrication techniques leads to both disposability and democratization. The ability to fabricate an entire swarm for a fraction of the cost of a single large robot opens up some interesting use cases. Instead of closely guarded, carefully maintained institutional or industrial investments, microrobots may serve as practically single-use ("on a whim") tools. For the cost of a cordless drill you could put a pack of microrobots in your toolbox, using them as needed without a significant care for whether they get damaged or lost.

Candidate Propulsion Mechanisms for Flight

Focusing more narrowly on flying microrobots, the next question to answer is – "why use atmospheric ion thrusters?" Conventional wisdom would be to draw on either well-understood mechanisms or inspiration from nature when designing systems with as many (figurative) moving parts as a flying microrobot. This section will attempt to outline some of the advantages and disadvantages of using EHD force for propulsion versus the two most popular mechanisms at this scale, spinning rotors and flapping wings. Comparisons of these mechanisms in theory and in implementation are shown in Table 1.1 and Table 1.2, respectively.

Table 1.1: Qualitative comparison between actuation candidates for centimeter-scale flight based on theory. X = Worst, XXX = Best

	Propellers	**Flapping Wings**	**EHD Thrust**
Mech. Complexity	XX	X	XXX
Control Complexity	XXX	X	XX
Mech. Efficiency	XX	XXX	X
Thrust-to-weight	X	XX	XXX
Robustness	X	XX	XXX

"Pico" air vehicles [95, 16], under 5cm and 500mg, sit in a unique aerodynamic position compared to typical man-made flying vehicles. While everything larger than a bird (Re > 10,000) can take advantage of the high lift to drag ratios possible due to the dominance of inertial forces, the scale and flight speed of a pico air vehicles places it much closer to a fully laminar region (Re < 2,500). Viscous drag begins to dominate, lift to drag ratio decreases drastically, and new "unsteady" dynamics become possible for flight. In nature this manifests itself as a stark transition between a soaring flight mode found in the majority of birds and the flapping wing mechanism used by insects.

The quadcopter is by far the most popular archetype for modern autonomous flying robots. Typical quadcopters are on the order of a meter in size, but consumer models as small as 5cm exist (e.g. the CX10). Reynolds number of the propeller airfoil tips for a typical centimeter-scale quadcopter is on the order of 10,000, right around the turbulent to laminar transition flow region [64]. Although even small quadcopters demonstrate impressive performance, they suffer from extremely short flight time (on the order of minutes) and extreme fragility. Using actuator disk theory, thrust from a propeller can be expressed as:

$$T = k_t \rho n^2 D^4 \tag{1.1}$$

where k_t is the thrust coefficient (a function of propeller design and geometry), ρ is the fluid density, n is the propeller angular velocity, and D is the propeller diameter. Even a naive approach to scaling therefore shows that as critical dimension of the propeller decreases,

Table 1.2: Quantiative comparison between actuation candidates for centimeter-scale flight. It should be noted that in some cases, data for the comparison chart on the right has been estimated or derived with some assumptions from published work.

Type	**Source**	**Meas. Force [N]**	**Thrust [N/m^2]**	**Thrust Eff. [N/W]**	**Thrust-to-weight**	**Largest dim. [cm]**	**Mass [mg]**
Nano-quad, coreless DC	bitcraze	0.55	86.5	0.039	2.04	13.7	27000
Fixed-wing, EHD	[96]	3.2	3	0.005		500	
Flapping, piezo	[94]	1.14e-3	5.7	0.03	1.9	3	60
Flapping, electrostatic	[51]	7.92e-5	0.4	0.05	0.16	5.6	50
Flapping, electromag.	[52]	1.17e-4	0.39		0.13	3	90
Ionocraft, EHD	[17]	1.2e-3	7.6	0.002	4	2	30

rotational speed must increase dramatically to maintain the same thrust levels. This problem is further compounded by the decreased lift coefficient of airfoils (i.e. the propeller section) at low Reynolds numbers regimes [5] and the fact that viscous drag is proportional to the speed of rotation. Miniature brushless DC motors capable of the RPM required by centimeter-scale propellers (typically on the order of 50,000) are fragile and more inefficient than larger versions [64].

As we scale increasingly smaller, fighting against the physics doesn't make sense; we can instead turn to nature for a solution. Flapping wing micro air vehicles (FMAVs) represent a biologically inspired mechanism for centimeter scale flight. Significant progress has been made, including: controlled flight of a flapping wing robot with a piezoelectric actuator [94]; takeoff of a robot with an electromagnetic actuator [99]; measured thrust using an electrostatic actuator [51]; and even wireless takeoff using an external laser pointed at a high voltage PV cell on a piezo-actuated flier [36]. Nevertheless, biomimetic fliers are difficult to design, build, and control. Engineers face a constant tradeoff between size, mass, and efficiency of mechanical motion, as the flapping wing mechanism functions increasingly well at smaller Reynolds numbers (and worse at higher Reynolds numbers). Incorporating all the system components necessary for an autonomous robot, while maintaining the scale and therefore Reynolds number regime of a flying insect, will test the limits of packaging, electronics, and actuation in even the most optimistic case. A notable exception to this constraint of scale is

the hummingbird, which has evolved an extremely complicated mechanical transmission able to produce fast wing motions (Re $>$ 7000) that allow it to fly like an insect while massing about five grams. While the systems engineering efforts of nature are worthy of aspiring to, it may not be the path of least resistance.

Electrohydrodynamic thrust is a propulsion mechanism that is silent, has no mechanical moving parts, is mechanically trivial to design, and theoretically simple to use for controlled flight. It has unparalleled potential for robust construction, a high thrust-to-weight ratio, and retaining functionality through a wide range of Reynolds numbers. The thrust itself is scale invariant, indicating a favorable scaling to low-mass systems. Just as importantly, the mechanism is relatively underexplored for propulsion; I believe that the future is filled with important discoveries that will further increase the advantages of EHD while diminishing the downsides (e.g., high voltage operation, lower mechanical efficiency than wings).

Contributions

The summarized contributions of my dissertation work are as follows:

- *Elucidation and exploration of the scaling of corona discharge based electrohydrodynamic force.* Related work at the millimeter or submillimeter scale typically relies on incomplete or inconsistent theoretical backing, empirical models with decreasing relevance at this scale, or simplifying assumptions that simply do not apply. I believe that I provided one of the more thorough (and candid) investigations of the physics of corona discharge based EHD at this size scale.

- *Novel proof of concepts demonstrating implementation possibility of meso- and microscale EHD systems.* It has been decades since the last large wave of serious academic effort devoted to electrohydrodynamic force based propulsion. I believe that by demonstrating the viability of systems created with both standard commercial materials and rapid prototyping techniques, as well as techniques specific to the semiconductor industry, others will be encouraged to study EHD for meso-scale and smaller propulsion applications.

- *Exploration of geometric effects and assembly techniques specific to MEMS-based electrodes.* Although on one hand modern photolithography affords tremendous freedom for design, on the other there are significant constraints imposed by planar MEMS subtractive manufacturing. I have investigated various designs for electrode sets as well as various assembly methods for their integration. I believe that both my quantitative as well as qualitative results are valuable for future researchers on this topic.

- *Design, fabrication, and characterization of a centimeter-scale flying robot with no precedent and no natural analogue.* The ionocraft is the smallest EHD-powered flying robot to ever exist. It has a relatively high thrust to weight ratio compared to other pico air vehicles; this lets it carry state of the art commercial sensors for control. The

fabrication is simple and amenable to batch processes that could result in an extremely low unit cost. Although comprised of many discrete components, the assembly process is mechanically simple and could be performed by a commercial pick and place machine.

- *A research roadmap towards the creation of a future autonomous ionocraft.* I use my accrued domain knowledge to chart out some future directions for researchers seeking to use EHD for propulsion, as well as to provide some design guidelines for a future autonomous system.

1.2 Electrohydrodynamic Force for Propulsion, In Brief

What follows is a colloquial explanation of corona discharge-based electrohydrodynamic force:

Assume two electrically conductive structures are separated by a dielectric fluid, in this case air at atmospheric pressure. An applied voltage between geometrically asymmetric electrodes will result in a non-uniform electric field, with higher relative magnitude in the proximity of the electrode with a higher surface charge density (e.g., one with a small radius of curvature). Given a sufficiently high field strength, an initial ambient electron will gain enough kinetic energy to ionize a neutral molecule of air, "freeing" another electron. Assuming that the electric field magnitude is high enough for this electron to regain enough kinetic energy for another impact ionization event before its next collision (or recombination with the electrode surface), this effect will continue, growing the number of generated ions geometrically. At some distance r from the surface of the electrode, the electric field will decrease below the criterion for continued ionization events between collisions; electrons will instead recombine with ions or attach to neutral air. As a result, with the applied voltage constant, a stable bipolar plasma region is formed around the "sharp" electrode. Outside the plasma region, a unipolar drift region is established between the two electrodes as ions are ejected. A closed circuit of ion current is formed between the two electrodes — collectively, this stable atmospheric plasma (the "corona") and the ion current (the "discharge") form the phenomenon known as corona discharge (see Figure 1.1).

Electrohydrodynamic (EHD) force refers to the kinetic energy transfer between charged particles and a neutral fluid. In the case of corona discharge, the energy transfer occurs via collisions between the ions in the discharge and the neutral air molecules occupying the electrode gap. It is worth noting that negligible net force is produced from the collisions occurring within the bipolar plasma region. Momentum transferring collisions occur in a specific direction, resulting in a net vertical acceleration of neutral air evacuating the gap. As pressure decreases, new air is pulled into the system, effectively creating a fluid accelerator much like a propeller or jet engine. Viewed one way, EHD is a direct transduction of electrical input power to output mechanical work in the form of accelerated air; viewed another, it is instead a conversion from the mechanical work of the moving ions to mechanical work of

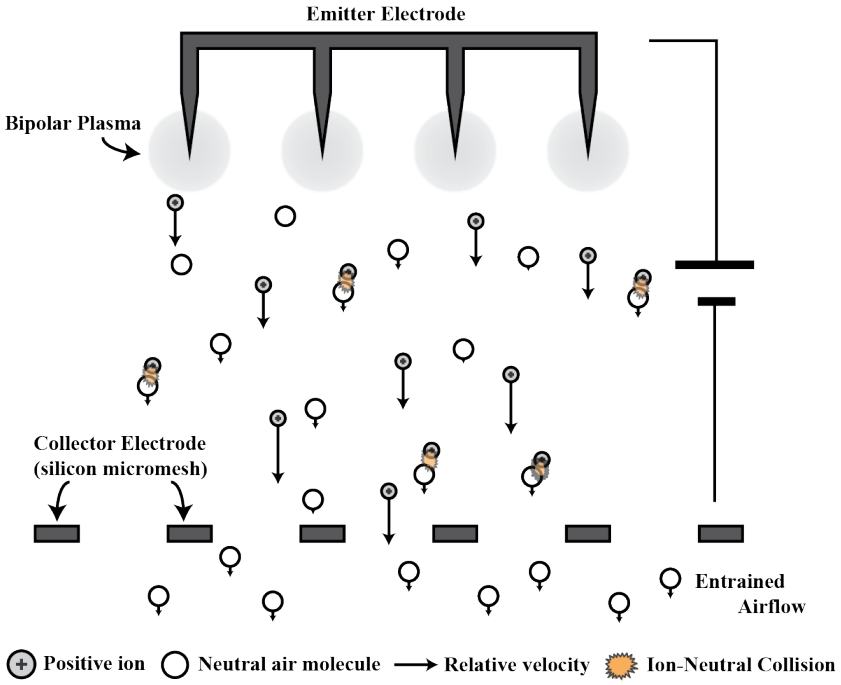

Figure 1.1: Schematic depiction of the cross-sectional view of an emitter wire and collector grid electrode pair. Thrust is produced when ions, drifting in the applied electric field, collide with neutral air molecules and impart momentum. Bipolar ions are generated in the corona plasma region localized at the sharp tips of the emitter electrode, but only positive ions (mainly N_2^+) will drift towards the collector grid.

moving air. Although similar in some ways, EHD force is not electrostatic in the same way as a standard MEMS actuator; the ion discharge results in a DC current, and the electric field strength is a function of the space charge distribution of the ions themselves until a steady state (i.e., space charge limited) current is reached.

1.3 A Brief History and Modern Applications of Corona Discharge and EHD

This section is intended not as a comprehensive survey of the field of electrohydrodynamics, but instead as a succinct overview of the scientific study (and when possible, general scholarly perception) of EHD force through its history. Although more complete reviews exist (see end of section), it is worth repeating if only due to the number of incredible minds (and far-flung ideas) which have populated the field. It should be noted that within the majority of literature, EHD and corona discharge are used almost interchangeably. Technically, the

corona discharge is only the ion source that leads to the resultant electrohydrodynamic force; alternate mechanisms for ion generations, and their implications on EHD performance, are discussed in later sections.

Accelerated air resulting from EHD force was recorded as early as 1709, when Francis Hauksbee of the Royal Society reported a blowing sensation by holding a charged tube to his face. Interestingly, in investigating this effect he also ended up recording some of the first notes on electrostatic precipitation (i.e., removal of fine particles from air using an electrostatic charge). This finding was later replicated by both Isaac Newton and Benjamin Franklin; the former endowing the phenomenon with its first name, the "electric wind", in 1718. It is also worth noting that as early as 1750, Wilson of the Royal Society proved that this effect only occurred in the presence of air. As is a common thread in the history of EHD, this knowledge was either lost or forgotten by the many researchers who labored to demonstrate EHD force in vacuum at the end of the 20th century. It is especially ironic in light of Robinson's note of surprise in [76] regarding the seemingly inadequate communication between scientists of the previous century leading to many independent "discoveries" of the electric wind.

Both Faraday (1838) and Maxwell (1873) also contribute to the history of electrohydrodynamics. The former was among the first to attribute the "electric wind" to kinetic energy transfer between charged and uncharged particles. Maxwell took the theory further by qualitatively describing the corona plasma region and correctly attributing the source of ions to a breakdown of air due to a sufficient electron energy. Neither man was able to fully explain the phenomenon, largely because the gaseous ion was not discovered until later in 1896. It is interesting that, although Maxwell had seemingly explained the phenomenon with remarkable precision (given the additional knowledge of gaseous ions to his description), researchers in the 20th and even 21st century continued to attribute some degree of mystery to the electric, or later, ion wind.

Thomas Brown, in collaboration with Paul Biefeld, filed a 1960 patent for an "Electrokinetic Apparatus" that kicked off a new frenzy of interest in EHD force. Brown wrongly attributed his "discovery" of EHD force to some kind of antigravity effect despite a severe lack of evidence, and it is unfortunate that this belief persisted among both hobbyists and the occasional researcher alike for over 50 years. The "Biefeld-Brown effect" was investigated for use in aircraft in the early 1960s, even being featured on the front cover of *Popular Mechanics* in August 1964. At the time of the *Popular Mechanics* article, the most successful demonstration of EHD thrust was with the "lifter" model now popular with students and hobbyists. The lifter is on the order of 0.1 to 1 square meter, typically constructed from balsa wood and aluminum foil, and can take off when connected to a high voltage (30 kV) power supply. These supplies can be easily sourced from standard microwaves or older (e.g. CRT) televisions and monitors, but are heavy and quite dangerous.

Important fundamental research from investigators including Christenson, Moller, and Robinson realigned this effort with previous investigations of electrohydrodynamic force in the mid to late 1960s. Ultimately, the effect was deemed to have too low of a thrust aerial density and too low of an efficiency for human-scale flight [77, 12]. The theoretical framing

as well as many of the fundamental governing equations for EHD force found in these works are correct. Nevertheless, uncertainty surrounding the thrust persisted until much later; a NASA technical report was commissioned in 2004 after researchers in the Army Research Lab concluded that "at present, the physical basis for the Biefeld-Brown effect is not understood" — in 2002. Unsurprisingly, they concluded that the thrust could only be attributed to electrostatic forces on ions causing momentum transferring collisions [7]. More recent theoretical work has seemingly confirmed earlier conclusions that electrohydrodynamic thrusters are not well suited for human-scale propulsion applications [71, 30]. The first wireless EHD propelled fixed wing vehicle was recently demonstrated [96]. Generating sufficient lift to carry the power supply unit necessary for the 40kV thrusters (around 600W) required a wingspan of five meters; no other useful payload was demonstrated. While an important achievement in systems engineering and as a proof of concept, it still indicates, to me, that we are better off looking towards miniaturization as the prime use case for EHD.

Modern applications of corona discharge based electroydrodynamics can be broadly separated into two categories: ones that take advantage of corona discharge specifically as an ion source mechanism, and ones that primarily utilize the resulting EHD airflow. Corona discharge in air has been found to be a relatively stable, repeatable, and high current ionization source for ion mobility spectrometry [83], industrial electrostatic precipators [97], photocopiers and jet printers, surface treatment systems [78], and ozone producers [81]. Microfabricated corona discharge based devices have shown promise as portable airborne particle analyzers and separators [13]. The largest current driver of miniaturization of corona discharge based EHD devices is for thermal management applications (IC cooling). A review of this research can be found in [90]. It should be noted that millimeter-scale devices are rare. Ong et al. demonstrated microfabricated devices with onset voltages around 1.1kV, but their low current makes them unsuitable for thruster applications [68]. The important metric of thrust to weight ratio is also unique to thruster applications and is relatively unexplored in literature.

Further reading: Myron Robinson, one of the first investigators to rigorously study the effect, also reviewed the history [76]. Interestingly, Robinson references an even earlier historical review paper by Lehman in 1897 summarizing the knowledge up until the turn of the century, but the paper itself is not archived. A more recent and thorough review on the history as well as contemporary applications of EHD force (specifically resulting from corona discharge) can be found in [29]. It is a testament to the intriguing nature of the effect that it has generated so much scholarly interest, over such an extended time period, without (yet) finding a significant foothold in an industry sector.

Chapter 2

Theoretical Framework and Numerical Modeling

This chapter attempts to provide a basis for understanding the fundamentals of corona discharge and electrohydrodynamics. While the material is sufficient for understanding the experimental work in later chapters, it is by no means complete. When possible, I have inserted nearby references to the best related material I have come across. The chapter concludes with an investigation of a unified numerical model, coupling corona discharge and electrohydrodynamics through a commercial multiphysics software package (COMSOL). While I make no strong claims as to whether this model in and of itself constitutes a research contribution, I have both attempted to make the model easily replicable and have pointed out shortcomings and room for improvement.

Research questions to answer:

- Where and why do standard models for corona discharge begin to fail?
- What typical simplifying assumptions for EHD fail or change at the meso- to micro-scale?
- Can a numerical model be developed that would actually serve as a useful design aid for EHD propulsion?

2.1 Corona Discharge

The most common method of atmospheric ion generation for EHD thrust is through the atmospherically-stable corona discharge phenomenon. Corona discharge is characterized by a self-sustained plasma localized around a charged conductor, the "emitter", and ionic current flowing to a second electrode, the "collector". The magnitude of the discharge is typically space-charge limited, with the polarity determined by whether positive voltage is

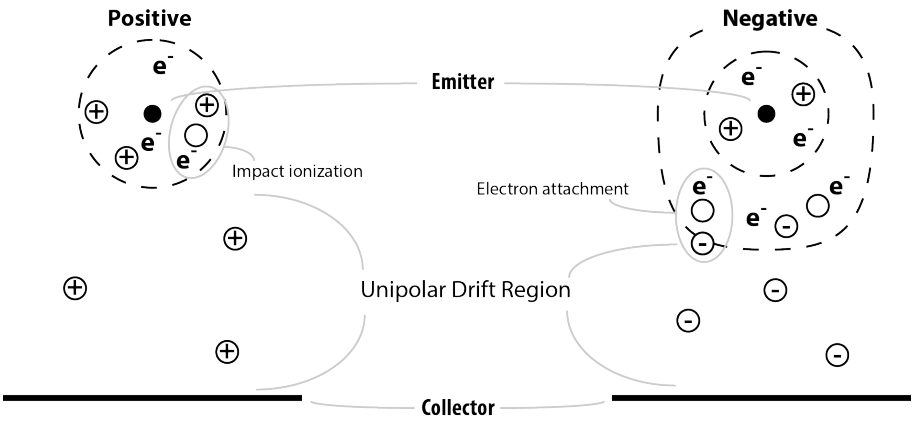

Figure 2.1: Schematic depiction of positive and negative polarity corona discharges in a point to plane configuration. Relative species concentrations and device geometries have been exaggerated for clarity.

applied to the so-called emitter ("positive corona discharge") or the collector ("negative corona discharge") [8].

Positive Versus Negative Corona Discharge

Polarity in a corona discharge process refers to the sign of the emitter electrode relative to the collector; a positive corona discharge will have a positive bias applied to the emitter, and vice versa. This is a non-trivial distinction that has ramifications on everything from ignition voltage to resultant EHD force. A schematic depiction of both polarities is shown in Figure 2.1. Excellent summaries of the two corona discharge polarities can be found in [10, 9].

In a positive corona discharge, ionization occurs due to inelastic collisions between electrons and neutral gas molecules. These impact ionization events release free electrons which are subsequently accelerated by the electric field, leading to further ionization events (an "avalanche" effect). The secondary electron source for sustaining the plasma is from photoionization of neutral gas via high energy photons emitted during de-excitation of ions following impact ionization. The primary mechanism for negative ion formation would be electron attachment, but the rate coefficients are small compared to those for impact ionization at the electron energies present within the plasma region; the corona plasma region can therefore be assumed to be a bipolar mixture primarily composed of positive ions and free electrons. Naturally occurring free electrons in the inter-electrode gap provide the seed for initial formation of the plasma.

A negative corona discharge has a more complicated plasma region, as there is both a layer composed of positive ions generated by impact ionization alongside free electrons as well as an electron attachment region where the bulk of the negative ions are formed prior to

unipolar drift. The primary source of secondary electrons used to sustain the plasma is via photoemission from the emitter electrode surface, which is a function of the work function of the material. Naturally occurring ionization events (e.g. photoionization) provide the seed for initial formation of the plasma. Negative corona discharge has been widely reported as a less qualitatively uniform phenomenon, with plasma appearing as discrete points or "tufts" along the emitter.

There are numerous reasons to use a positive corona discharge for propulsion applications, including: reduced ozone generation compared to negative corona discharge, which makes future systems safer to operate indoors in large quantities; the lower ion mobility of positive ions (N_2^+) compared to negative (O_2^-) in air leading to higher force output (see Section 2.2); reduced corona ionization region thickness, leading to an increased unipolar drift region length and hence output force; reduced dependence on electrode material selection due to not using the electrode itself as a secondary electron source for sustaining the plasma, opening up the design space; and improved plasma uniformity near the ignition voltage for greater predictability of performance. Throughout the remainder of this section (and throughout my research efforts) I have used a positive corona discharge. Although I will not include data, I have periodically validated this choice during device characterization; negative corona has performed worse in every trial.

Empirical Models and Simplifying Assumptions for Corona Discharge

The vast majority of literature taking advantage of corona discharge relies on a largely empirical/phenomenological theoretical foundation. An equation of the form shown below, sometimes referred to as "Townsend's relation," has been experimentally confirmed over a wide range of geometries and is assumed true for space-charge limited discharges such as corona [77].

$$I = CV(V - V_c) \tag{2.1}$$

Where V_c is the corona inception voltage and C is a constant with units of A/V^2 that depends on a combination of device geometry and ion mobility. Analytical values for C exist for a few simple geometries, e.g. concentric cylinders [26], but are typically extracted from experimental data.

Peek provided solutions for the critical surface field to initiate corona discharge for various geometries [70]. Peek's experiments were carried out with centimeter- to meter- scale electrode gaps and millimeter- to centimeter- radius emitter wires. For example, the empirically calibrated equation for the critical field (the electric field necessary to initiate a corona discharge) in a parallel wire electrode geometry is:

$$E_c = E_0\delta(1 + \frac{c}{\sqrt{\delta r}}) \tag{2.2}$$

Peek derived this critical field from the critical potential for corona onset, which between two symmetrical conductors is given as:

$$V_c = E_c r ln(\frac{S}{r}) = E_0 \delta r (1 + c/\sqrt{\delta r}) ln(\frac{S}{r}) \tag{2.3}$$

Where S is the distance between the wire centers in centimeters, c is an empirical dimensional constant equal to $0.301 cm^{1/2}$ for parallel wires, r is the wire radius in centimeters, δ is a density correction factor N/N_0, where $N_0 = 2.5 \times 10^{25} m^{-3}$ at STP, and E_0 is the bulk breakdown field strength in air (approximately $30 kV/cm$).

This equation is widely used in literature and consistently produces predicted voltages accurate to within about 10%. The pressure correction term is typically minor and ignored. Peek further stated that the radius of the plasma region would be equal to $c\sqrt{r}$, as that is the distance from the wire surface where the bulk breakdown field will be reached. The portion of Equation 2.3 which does take into account the gap is from a simplified version of the wire to plane electric field equation which assumes d is much larger than r.

Peek derived the complete equation for the electric field along the center axis between two parallel wires in [70] as below:

$$E(x) = \frac{V\sqrt{S^2 - 4r^2}}{(r + x)(S - 2r) ln(\frac{S}{2r} + \sqrt{(\frac{S}{2r})^2 - 1})} \tag{2.4}$$

Where r is the radius of the wire and S is the distance between the centers of the wires, $S = d + 2r$. Assuming that $S >> r$, this equation then simplifies to:

$$E(x) = \frac{VS}{(r + x) S ln(\frac{S}{2r} + \frac{S}{2r})} = \frac{V}{(r + x) ln(\frac{S}{r})} \tag{2.5}$$

Then solving for the critical potential, defined as the voltage where the electric field at $x = c\sqrt{r}$ is equal to the breakdown field:

$$E(c\sqrt{r}) = E_0 = \frac{V_c}{r + c\sqrt{r} ln(\frac{S}{r})} \tag{2.6}$$

$$V_c = (r + c\sqrt{r}) E_0 ln(\frac{S}{r}) = E_0 r (1 + \frac{s}{\sqrt{r}}) ln(\frac{S}{r}) = E_c r ln(\frac{S}{r}) \tag{2.7}$$

$$\tag{2.8}$$

The c term was empirically derived by Peek; because the electric field between the electrodes is a function of both radius and distance it is clear that this empirical relationship, which depends only on the electrode geometry (e.g. wire to wire vs sphere to sphere), cannot hold true for all values of the ratio d/r.

For our devices we are interested in a wire to plane solution, not the electric field between parallel wires (for Peek, the latter was interesting due to high voltage transmission lines). Th full parallel wire equation 2.4 is equivalent to an image charge solution to a wire-to-ground plate problem with twice the distance S between conductors (see Figure 2.2). Substituting into Equation 2.4, we find the electric field between a wire and a ground plane:

$$E(x) = \frac{V\sqrt{4S^2 - 4r^2}}{(r+x)(2S-2r)ln(\frac{S}{r} + \sqrt{(\frac{S}{r})^2 - 1})} \tag{2.9}$$

Assuming that $S >> r$, this equation then simplifies to:

$$E(x) = \frac{V}{(r+x)ln(\frac{2S}{r})} = \frac{V}{(r+x)ln(\frac{2d+4r}{r})} = \frac{V}{(r+x)ln(\frac{2d}{r})} \tag{2.10}$$

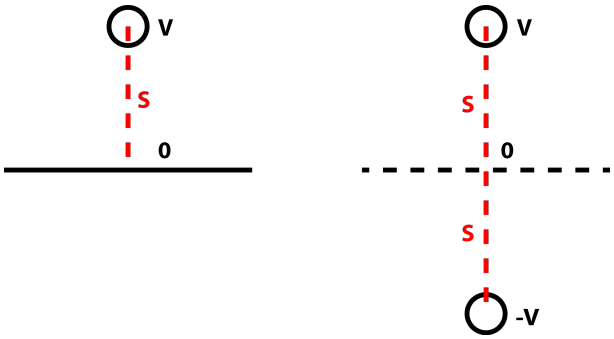

Figure 2.2: Schematic depiction of the wire to plane versus wire to wire geometries, and how the image charge method can be used to derive the former from a solution to the latter.

The geometry and relevant parameters are shown and labeled in Figure 2.3. Electric fields in the vicinity of the emitter wire as calculated by (2.10) versus the full version (2.9) can deviate by as much as 50% for d/r ratios less than 20. These shortcomings may help explain why research exploring sub-millimeter corona discharge with d/r ratios on the order of 15 have seen greater divergence from Peek's formulas [85]. While Peek stated that corona discharge would occur at d/r ratios down to about 3, Peek (and others [85]) have seemingly been unable to measure corona discharge before sparkover below a ratio of about 10.

Analytic Models for the Corona Plasma Region

A fully analytic model for corona discharge would allow for more accurate onset voltage prediction at the scales where Peek's empirical formula break down, as well as more accurately predict resultant EHD force production due to a better accounting of both plasma region thickness as well as space charge interactions.

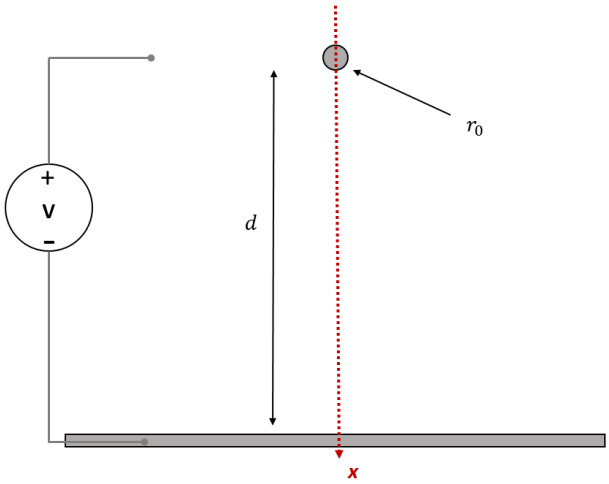

Figure 2.3: Schematic depiction of the wire to plane two dimensional geometry, with parameters relevant to calculating the electric field labeled.

Most work focuses on either the discharge initiation, e.g., the kinetics and sustaining reactions of the corona plasma, or the development of subsequent ion current with space charge effects taken into account. In the latter case, inception voltage and some current trends are typically taken from experimental data. A method of solving for the corona inception voltage as a function of electrode geometry outside the usable range of Peek's criterion would be a valuable tool for design; unfortunately, existing analytic models are typically confirmations of Peek's equations for simple geometries (e.g. concentric cylinders [26]) at >mm gaps. An interesting exception is [61], which claims greater accuracy for their analytical model at small gaps and for small emitter radii, although still only for concentric cylinder geometries.

A widely used method to determine the corona inception voltage for complex geometries is to arbitrary define a plasma radius, r_0, and then iteratively solve for electric field magnitude at this distance from the emitter electrode until it reaches a breakdown field magnitude, typically $E = 3MV/m$. This electric field magnitude, however, is not the true breakdown field strength at all electrode distances and conditions.

A more satisfying method of determining onset voltage is through the effective ionization criterion defined as:

$$\alpha_{eff} = \alpha_i - \eta \tag{2.11}$$

where α_i is the ionization rate coefficient and η is the electron attachment rate coefficient. A $\alpha_{eff} = 0$ would signify the boundary of the bipolar corona plasma region as free electrons would all be consumed [9].

One method of using this method is through arbitrarily defining a plasma radius, r_0, and then iteratively solving for α_{eff}, where both rate coefficients are functions of the reduced

electric field. When the electric field at r_0 is found to make this effective rate equal to zero then the critical inception voltage has been found.

It is obviously not satisfying to define a corona plasma radius a priori. Another method uses the integral:

$$\int_0^{r_0} \alpha_{eff}(r)dr = K \tag{2.12}$$

Where K is a dimensionless parameter known as the "ionization integral." Values of K have been empirically determined in the range of 5-20 [53]. Solving for the corona inception voltage for complex geometries would then be a process of iteratively integrating this quantity until it matches the a priori determined K. Unfortunately, K has only been analytically determined for simple geometries [65].

The Limits of Corona

At the extreme limit of scaling, as the inter-electrode decreases to some smaller multiple of the electron mean free path in air (about 200 nm at low electron energies [92]), sustained Townsend avalanche breakdown ceases to be the dominant charge generation mechanism. At some point, the required electron energy (and therefore electric field) required for impact ionization will become larger than the required electric field for a new mechanism to take place: field emission. This phenomenom and its potential for use in EHD is discussed more in Section 5.5.

2.2 Electrohydrodynamic Force

Electrohydrodynamics (EHD), sometimes referred to as electro-fluid-dynamics, electrokinetics, or ion drag pumping, refers to the motion of fluids with diffuse charged species under the influence of an applied electric field.

A one dimensional model for electrohydrodynamic thrust based on the Coloumb electrostatic force on a volume of ions leads to an expression for force in terms of ion current, I, distance the ions travel d, and the ion mobility, μ. Here V is the applied potential and A is the ion volume cross-sectional area. This assumes all ion current is due to applied drift field as opposed to bulk fluid motion, an assumption [77] proved accurate for the $3m/s$ maximum air velocities measured in this work versus ion velocity that is on the order of $100m/s$.

$$F = \int \rho E dV = \int \rho E A dx = \int \frac{Id}{\mu V A}\frac{V}{d}Adx = \frac{Id}{\mu} \tag{2.13}$$

This represents the theoretical maximum force from an EHD thruster. The fundamental electrostatic force given in (2.13) is proportional to ion drift distance; if the ratio of ionization

radius to gap distance is significant, then simply using the electrode gap to determine theoretical force is incorrect. This ratio is typically small for high d/r ratio devices and is safely ignored. However, Vuhuu and Comsa experimentally measured ionization radii on the order of hundreds of micrometers [89], which would be a significant fraction of a sub-millimeter discharge. For consistency with literature I have maintained d as the full inter-electrode gap when using this equation and reporting deviations from theoretical maximums. The relative ratio of ionization region to drift gap can be encompassed in a "loss factor," β:

$$F = \beta \frac{Id}{\mu} \tag{2.14}$$

Future investigations would do well to separate the factors out for analysis.

The Mott-Gurney law for space charge limited current density (2.15), which assumes that only one type of charge carrier is present in the drift field, that the carrier material is not conductive, and that carrier mobility (actually, a weak function of electric field) and permittivity are constant throughout the device, is assumed valid for a corona discharge based in-air system. Based on the Mott-Gurney law, the equation for the electrohydrodynamic force derived for the 1D simplifying case can instead be expressed in terms of applied drift field E and air permittivity ϵ_0:

$$I = \frac{9\epsilon_0 \mu A V^2}{8d^3} \tag{2.15}$$

$$F = \frac{Id}{\mu} = \frac{9\epsilon_0}{8} A E^2 \tag{2.16}$$

Note that this is force acting on the ions; direct translation of this to thrust requires that all momentum is transferred in the preferred thrust direction by ion-neutral collisions. Deviation from this assumption is also encompassed in the β factor of Equation 2.14. Assuming applied voltage is the same as the drift field potential and that ion current is the only current flow, this yields a thrust efficiency in terms of N/W of:

$$\begin{aligned} P = IV &= \frac{9}{8}\epsilon_0 \frac{A}{d^3} \mu V^3 \\ \frac{F}{P} &= \frac{d}{\mu V} = \frac{1}{\mu E} \end{aligned} \tag{2.17}$$

Note that this thrust efficiency also has a dependence on freestream air velocity, v, in its full form:

$$\frac{F}{P} = \frac{1}{\mu E + v} \tag{2.18}$$

which indicates that thrust efficiency of an EHD thruster will, unlike a jet or turbofan, become less efficient at higher speeds (i.e., as v approaches μE). For the projected drag-limited airspeeds of a centimeter-scale ionocraft (i.e., 1-10 m/s) this is largely not an issue;

ion drift speed will range from approximately 100m/s at a field of 5×10^5 V/m to 600m/s at a drift field of 3×10^6 V/m, corresponding to an efficiency deviation of about 1%.

Power efficiency, however, in terms of produced mechanical power per input electrical power, has been shown to increase with freestream air velocity in experiment from less than 1% to 7.5% at freestream velocities of 50 ms^{-1} [4]. To directly compute the output mechanical power requires integration of the velocity distribution over the local electric force density. For simplification we can assume an equation of the form below, although it will overestimate efficiency:

$$\frac{P_{out}}{P_{in}} = \frac{F(v + v_{acc})}{F(\mu E + v)} = \frac{v + v_{acc}}{\mu E + v} \tag{2.19}$$

where v is the freestream air velocity and v_{acc} accounts for accelerated outlet velocity. Assuming a standard commercial airplane cruising velocity of 240 m/s, a thruster operating with a 5×10^5 V/m drift field for higher efficiency, a 300% increased ion mobility due to being at 10km altitude [3], and that v_{acc} is 10 m/s, power efficiency would reach approximately 46%.

Ion Mobility

Ion mobility is a key factor in determining the thrust efficiency of EHD (Equation 2.17). The ion species, ambient air pressure and temperature, and relative humidity all affect mobility. A summary of these effects is shown in Table 2.1.

Table 2.1: How varying environmental factors affect ion mobility.

	Value	*Mobility*	*Notes*
Pressure (Pa)	⇑	⇓	Thrust efficiency will decrease by 80% from 0km to 25km due to this change [30]
Temperature (K)	⇑	⇓	Complicated dependency, $<$ 10% change from 87C to 250C [41]
Humidity (%)	⇑	⇓	Decreases by approximately 10% from 70% RH to 80% RH [28]

It is also worth noting that N_2^+ mobility is approximately 70% that of O_2^- [25] in air.

A consistent challenge when evaluating EHD systems is in deciding on an ion mobility constant to use in analysis. Direct measurement at test time is not feasible, and literature values for positive ions in air range from $1.6 \times 10^{-4} m^2 V^{-1} s^{-1}$ to $3.0 \times 10^{-4} m^2 V^{-1} s^{-1}$ [86, 62, 71]. Determining a thrust loss factor with any accuracy is therefore nigh-impossible

between different experimental setups and conditions; it implies that only measurements taken in the same location, at about the same time, can be trusted for any precision. It is interesting to note that corona discharge is actually a stable enough plasma mechanism for use in ion mobility spectrometry given a controlled instrument environment [83]. Lacking such a controlled environment, a closed loop feedback controller for an EHD thruster would likely benefit from real-time recalibration of the voltage-force transform using active current measurement.

2.3 FEA for Corona-discharge Based Electrohydrodynamics

Motivation and Description

A large amount of work has been performed simulating corona discharge-based EHD systems. The typical approach combines the critical field criterion established by Peek with the Kaptsov hypothesis [40], which stipulates that the electric field on the corona emitter surface remains constant at Peek's critical value even as applied voltage increases; the ionization region radius is typically ignored or assumed a constant (e.g. the same as emitter diameter). Surface charge density and subsequently the space charge region can then be solved for, yielding a numerical solution for ion current due to drift. Typical simulation performed in this manner agrees to within about 10% with experimental values [1]. Combining this approach with a diffuse species collision model and a flow model yields a simulated measure of air flow as a result of EHD ion-neutral collisions; this approach has also been verified experimentally [98]. Although there are obvious limitations with this approach as an a priori design tool for corona discharge, there are still possibilities for FEA to make an impact. I believe that two promising areas are in investigations of ion field path shape as a vertical thrust "loss" mechanism, and in design of mass- and flow- efficient collector electrodes.

The canonical expression for electrohydrodynamic force, where output force is directly proportional to ion current, assumes one-dimensional momentum transfer and ducted flow. In reality, ions will typically be traveling with some horizontal momentum at time of impact. This component of the momentum transfer is therefore, at least partially, lost as useful vertical thrust. Ion and electron beam systems in other applications often contend with this problem, going to great lengths to collimate their beams (i.e., minimize those undesired path components). Many of these approaches, such as external electromagnets or physical grates, are unfeasible for a mass-limited propulsion system. It may turn out that an important aspect of EHD thruster design is proper placement and shaping of the electrodes, not just to affect corona ignition properties, but also to shape the shape charge distribution and resultant field paths in order to maximize vertical momentum transfer. Concretely, a question that could be asked is, for a system with multiple emitter wires per collector grid, is there an emitter wire spacing that actually impinges the "interior" space charge region flow, creating more of a "jet" profile? Finite element analysis provides an answer.

Previous work has noted that collector electrode geometry significantly affects both corona current and the resultant flow rate, with grid electrodes performing better than rings [63]. Literature on airflow through micromeshes on the size scale relevant for centimeter-scale ionocraft is extremely sparse. A further consideration is how the micromesh geometry affects the electric field profile of the device. Maxwell claimed that at gap distances equal to or greater than the grid separation, the grid will look virtually identical to a solid plane at the emitter wire [57]. If this holds true for corona discharge devices, decreasing gap distance will necessitate a decreased grid separation and therefore presumably a higher drag coefficient. A multiphysics simulation model would allow for designers to view both the expected flow properties (e.g., coefficient of drag) of their systems as well as minimize the chance of "reverse corona" (e.g., if the grid pitch is too high, the grid wires will look like corona emitters of the opposite polarity). Key challenges include properly designing the simulation geometry, and inserting proper boundary conditions, such that the flow properties can be trusted. For example, right angles (e.g., the edge of a rectangular simulated geometry) have dramatic effects on flow, dramatically enhance electric field, and are likely non-physical.

Methods: COMSOL Multiphysics Simulation

The finite element method (FEM) is a computationally tractable way of solving a complex group of partial differential equations given a set of boundary conditions. This method, which organizes a system into a "mesh" where each mesh boundary represents a system of equations to be solved, is known as finite element analysis (FEA) when applied. COMSOL Multiphysics is a commercial FEA and simulation tool which includes multiple physics modules (e.g. electrostatics, fluid flow) that can be explicitly and implicitly coupled during FEM solving. Although many groups have applied numerical methods to corona discharge and electrohydrodynamics (e.g. [6]) using tools such as OpenFOAM, COMSOL is probably the most widely used FEA tool for this purpose [37]. Its graphical interface, active community, and large amount of documentation make it relatively straightforward to use. As always, a solid grasp of the theory *prior* to jumping in to the modeling is recommended.

Momentum-transferring interactions with neutral molecules can be modeled as an external force (i.e. Coulomb force) in the Navier-Stokes flow equation. This modeling assumes that the electrostatic force on the ions is exactly equal to the kinetic energy transfer to the neutral molecules. Coupling the electrostatics module with diffuse species flow and fluid flow models results in ion current density, j, as a sum of three different contributing terms:

$$j = qN_i(\mu E + v) - qD\Delta N_i \tag{2.20}$$

where D is the diffusion rate related to ion mobility and temperature, T, through Einstein's relation. These terms correspond to drift due to electric field, advection in a fluid media, and diffusion through the carrier fluid. For most arrangements, it is expected that ion current will be dominated by the drift term. A common challenge when modeling corona discharge is handling the charge injection mechanism. Here, I have assumed a uniform initial

charge distribution on the emitter electrode corresponding to the inception field. This assumption seems plausible if the Kaptsov assumption and the assumption that plasma radius is negligible compared to drift distance hold, but is an obvious failure source for miniaturized devices or ones with more complicated electrode geometries. Nevertheless, as long as the model is not being used as a predictor of voltage-current transforms or inception voltage, this simplifying assumption represents a fine initial path.

Table 2.2 shows the physics modules, most relevant governing equations within each module, and the boundary conditions used for this COMSOL coupled model. Alone, this is not enough to generate a coupled simulation; without coupling parameters specified, the physics modules will either be solved independently, giving false solutions, or will solve to zero due to under specified initial conditions. The mass transport and fluid flow models are coupled via convection, i.e. the movement of ions in the free airstream. The mass transport and electrostatics modules are coupled through the "migration in electric field" option as well as by setting the space charge density explicitly equal to the concentration of dilute species. The electrostatics module is tied to the fluid flow model by adding a volume force to the fluid flow equivelant to ρE. Screenshots of relevant input fields in COMSOL are shown in Figure 2.4. Excluded in my model is the thermal domain; some prior work has attempted to model it, coupling with Joule heating due to the ion current and buoyancy volume forces produced via temperature gradients [6]. It is uncertain how much thermal effects change the results, and while it may be a vital domain to cover for heat transfer applications, it is unclear how much it matters for propulsion.

Table 2.2: Overview of Multiphysics FEA Setup: Modules

Physics Description	*COMSOL Module*	*Governing Equ.*	*Boundary Conds.*
Electrostatics	Electrostatics	Gauss, Poisson	DC voltage at emitter, ground at collector
Mass Transport	Transport of Dilute Species	Nernst-Planck	Concentration at emitter surface, outflow at collector surface
Fluid Flow	Laminar Flow	Navier-Stokes	No slip at all surfaces, outlet (zero pressure/stress) at model bottom

Geometry and Mesh Definition

For the fully coupled simulations I have used a 2D model in the interest of convergence, time per simulation, and ease of use. Simulations with the level of mesh refinement required

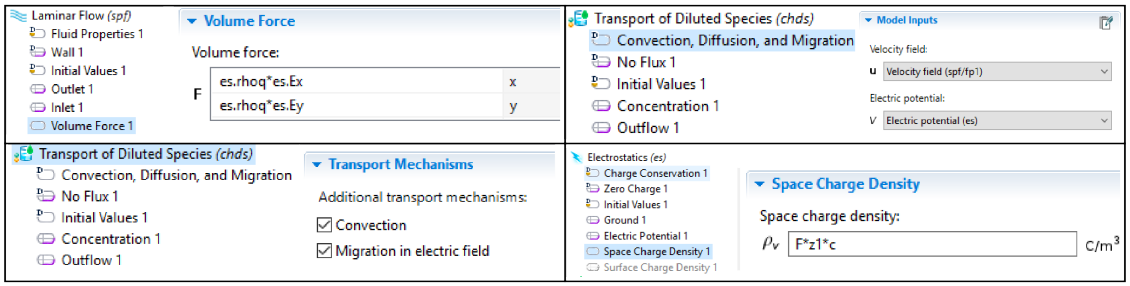

Figure 2.4: Screen captures of the exact COMSOL fields in which coupling between the physics modules is achieved.

for well-behaved coupled electrostatic and fluid flow modules are extremely inefficient when performed on a consumer PC. The geometry of my ion thrusters is largely axi-symmetric, and edge effects (e.g. flow around the collector grid "frame") can still be captured in two dimensions. Other authors have shown transferability of their 2D models to experimental results in the past. As corona discharge inception is not the focus of this modeling effort, a circular geometry is used for the emitters to simplify convergence. As fluid flow models have difficulty converging for flat planes and right angles, circular geometries are also used for the collector grid lines. This is obviously non-physical; more rigorous experimental validation would be needed to properly assess a radius of curvature to use for rectangular wire geometries.

Convergence of the electrostatic and fluid flow modules requires refinement around flow boundaries as well as the charge injection point, i.e., the collector grid and emitter wires (Figure 2.5). There is an additional trade-off between model boundary size and convergence time. Too small of a model boundary and the conditions specified at the walls (e.g., outlet or no flow) will unduly influence behavior; too large, and convergence will take extremely long as the solver works on "useless" nodes. Unfortunately, I think that the compromise must be found largely on a case-by-case basis.

Results and Discussion

Simulations investigating the effect of emitter spacing were performed (Figure 2.6 and 2.7). Although I am hesitant to make statements about the validity of these results without experimental validation, I believe the method is sound to allow for some qualitative comparison. Note that an emitter separation of 500μm is nearly enough to isolate the resulting flow regions for an inter-electrode gap of 750μm. This may indicate agreement with analytic models developed by Gilmore et al in [30] which state that optimal emitter wire spacing is at roughly 70% of the inter-electrode gap.

Simulations were also performed that investigate the effect of emitter point alignment with the collector grid (Figure 2.8). Consider a series of emission points above a mesh; given perfect assembly, a designer has the choice of aligning each point above either grid crosspoints

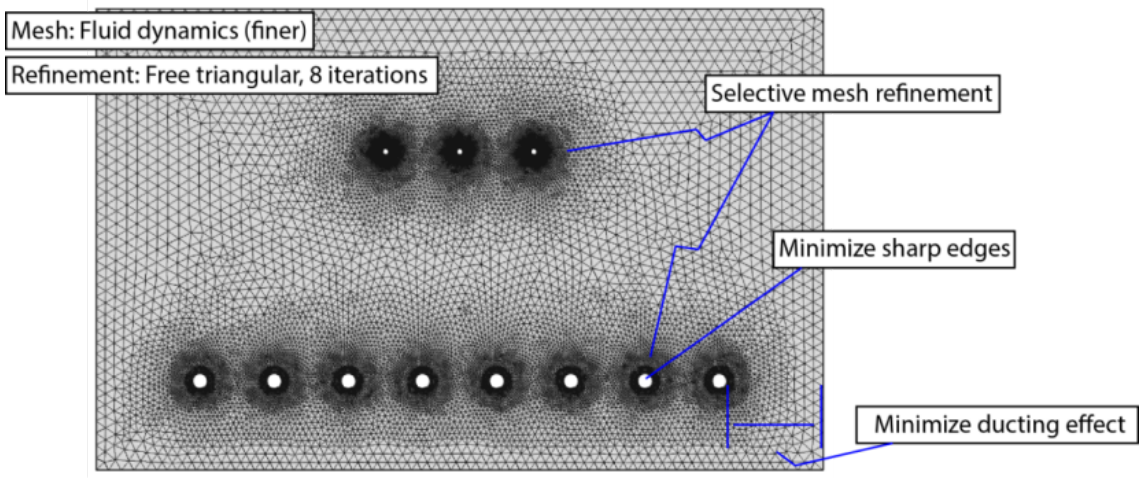

Figure 2.5: Meshing strategy for COMSOL multiphysics coupled FEA. Refinement around the emitters and around flow barriers such as the collector grid is critical for convergence.

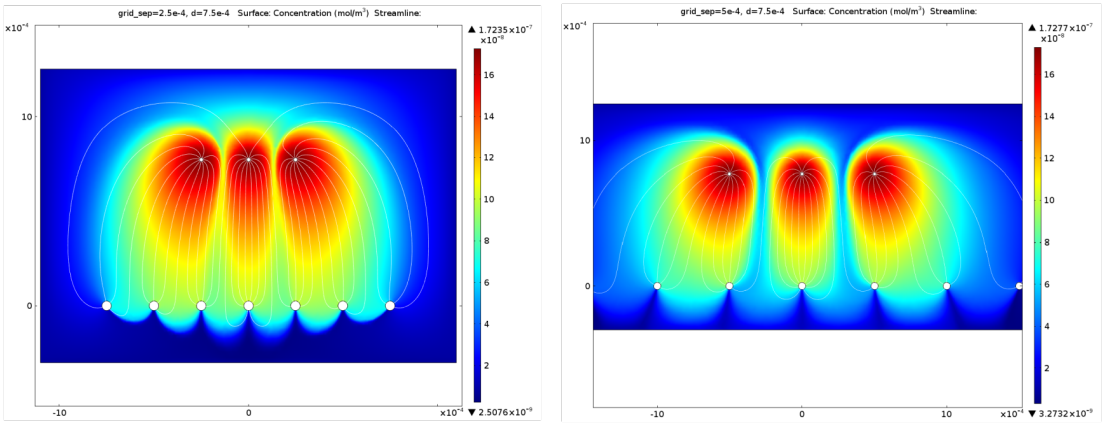

Figure 2.6: Plots of the space charge distribution given a static applied voltage, assumed to be above the corona ignition voltage. The spacing between both emitter wires and collector grid lines are varied, although only the former is assumed to be significant electrostatically. It is clear that emitter wire neighbor spacing affects space charge distributions of both the interior and exterior wires; although closer spacing may impinge interior flow and create a more uniform vertical "jet", it also creates an elongated horizontal distribution at the exterior (clearly visible in the plotted white field lines).

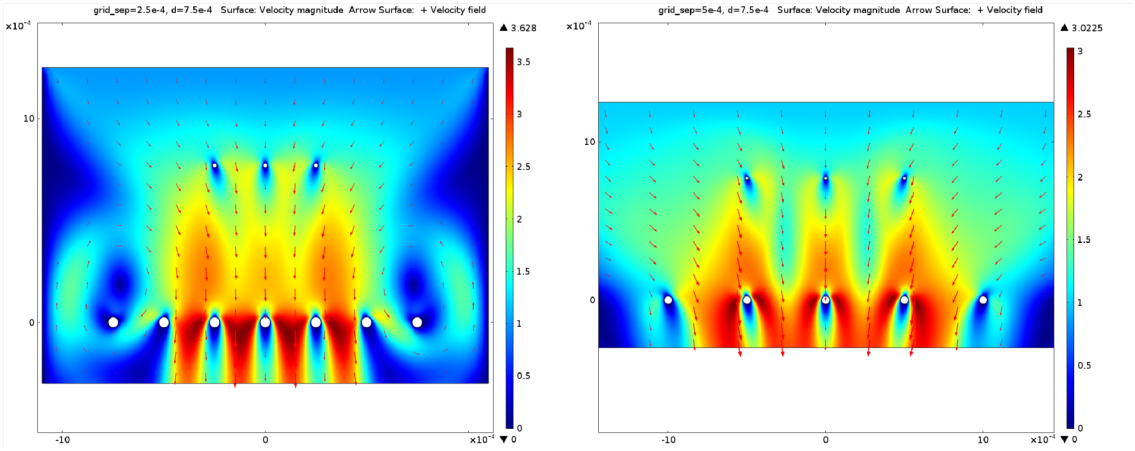

Figure 2.7: Plots of the resultant fluid velocity at a given applied voltage, assumed to be above the corona ignition voltage. The spacing between both emitter wires and collector grid lines are varied. For the closer wire pitch, impinged flow case, recirculation patterns are evident at the collector electrode.

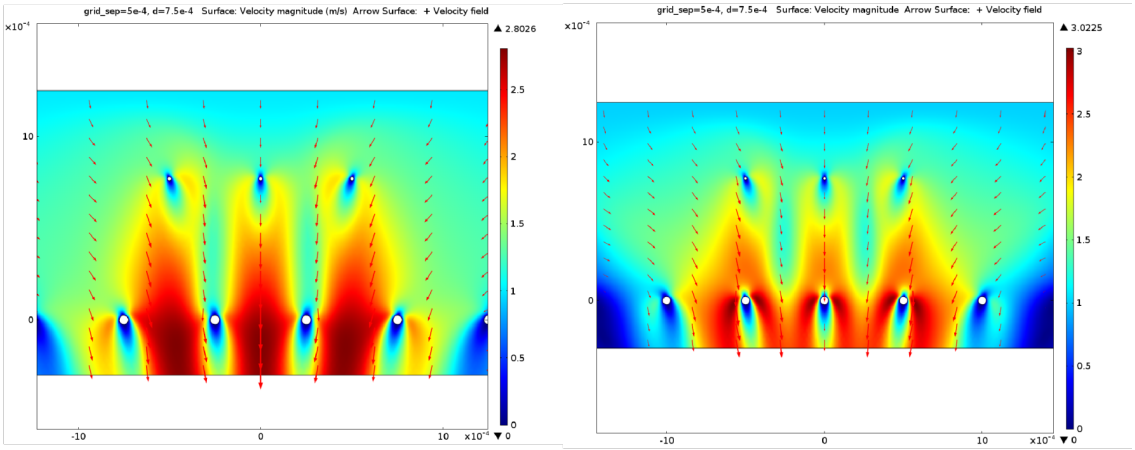

Figure 2.8: Plots of the resultant fluid velocity at a given applied voltage, assumed to be above the corona ignition voltage. In this case, the alignment between the emitter wires (i.e., whether emitters fall directly over grid crosspoints or over open spaces) is varied. The assumption would be that the former is "better" electrostatically, while the latter is better for aerodynamic drag. The latter result seems supported by the simulation results (i.e., the wires present less of a flow boundary and there is less of a drag "bubble" underneath them), but would require experimental validation.

or open areas. Obviously, doing so would prohibit certain emitter point spacings and emitter wire densities; simulation should be able to provide some indication of whether drag benefits are worth this choice. Unfortunately, although simulation shows a large qualitative difference between the two cases, imperfect assembly techniques made experimental validation difficult without more focused effort.

A three dimensional model was also created to study purely the aerodynamic drag through the collector grid. O'Hern and Torcyznski measured drag coefficients on the order of 1-5 from photoetched meshes with wire widths of 50 μm, thickness of 50 μm, and separations of 318 μm at similar Reynolds numbers to those expected in EHD microrobots [67]. Computational values for drag coefficient from this work were found to be sensitive to mesh wire cross section, and later experimental results showed a strong dependence on wire separation, with drag coefficient increasing by about 50% for a 20% lower open area fraction (i.e., more of the total grid area is solid).

Concretely, using the results of Figure 2.9 (e.g., averaging the pressure below the grid), solutions for drag coefficient and Reynolds number could be computed:

$$Re = \frac{\rho U D_{wire}}{\mu} \tag{2.21}$$

$$c_d = \frac{\Delta p}{0.5 \rho U^2} \tag{2.22}$$

Where ρ is the air density of $1.225 kg/m^3$ and μ is the dynamic viscosity of $1.82 * 10^{-5} kg/ms$. For the geometry shown, computed drag coefficient is approximately 4.0, which is well in line with literature values for similarly sized micromeshes. This indicates potential for 3D FEA to be used as a design tool for collector electrodes.

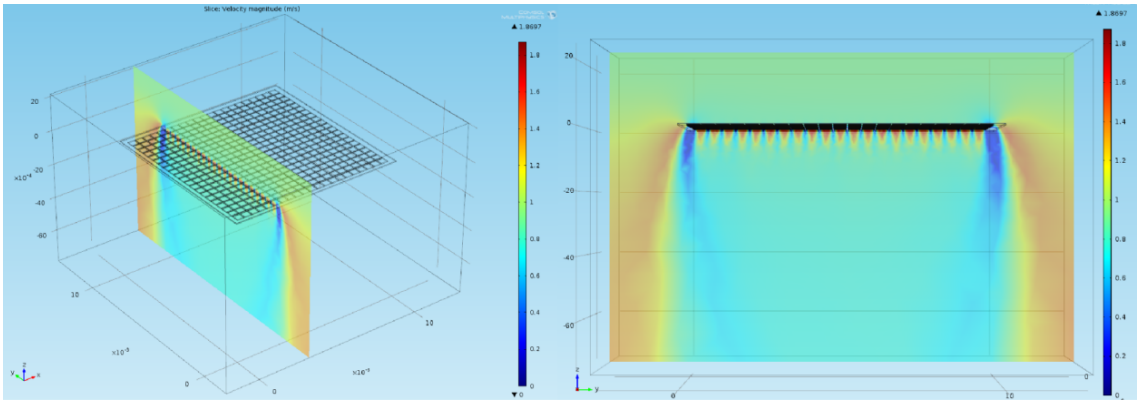

Figure 2.9: Plots of the resultant fluid velocity through a three-dimensional microgrid given an inlet at the top of the model. Although the flow would be ducted by the boundary conditions of the model sides, they are placed far enough to not affect the grid flow. Not shown is the associated pressure plot from which drag coefficient can be extracted.

Contributions and Conclusions

I believe that this section could serve as a strong starting point for someone looking to perform FEA of corona discharge based electrohydrodynamics. Personally, I struggled with properly coupling the multiphysics modules in order to get proper convergence, and this section would have helped me. I think that, unfortunately, FEA is not yet a true a priori design tool for EHD propulsion, and needs extensive experimental validation with each use — hopefully someone will take it a step further in the future.

I do think that some conclusions can be drawn from this work with a decent amount of confidence, namely: it is possible to explore the effect of space charge region impingement due to neighboring emitters as a function of electrode spacing with FEA; FEA could serve as a tool for investigating mass optimization of electrodes (e.g., when do extra grid wires only add more drag and mass); and FEA gives reasonable estimates for drag through a micromesh in 3D, pointing to future success as a design tool.

Chapter 3

Experimental Scaling Validation and Proof of Concepts

While on paper electrohydrodynamic thrust scales well enough to justify its use for insect-scale flight, this conclusion was completely lacking in experimental validation when I started my graduate career. My initial effort focused on, essentially, proving that this was an idea worth pursuing. Although there existed some prior work on sub-millimeter corona discharge and some prior work on heat transfer using the resultant EHD flow, the question remained as to whether a propulsion system (e.g. a free-standing device with directed air acceleration) could be created. Additionally, prior work had largely looked at static measurements; there was an open question about the possibility of feedback control of an EHD system, especially with high enough frequency for stability at the centimeter scale.

Research questions to answer:

- Is corona discharge a reliable effect at the millimeter- and sub-millimeter- scale for producing directed EHD force?
- Can thrust-to-weight ratio be increased by aggressively scaling electrode dimensions, without influencing the produced force?
- How does electrode geometry and separation affect corona discharge and EHD force production at the sub-millimeter scale?
- Is it possible to implement real time feedback control of an EHD thruster?

3.1 A Rapidly Prototyped Meso-scale EHD Flier

Some of this work was presented at the Robot Makers (RoMa) workshop at the Robotics: Science and Systems 2014 conference.

Motivation and Brief Description

The first step in investigating EHD for insect-scale robots was to experimentally verify scaling relationships at the meso scale. The standard "hobby model" ionocraft uses balsa wood, aluminum foil, and magnet wire as components, and is cut and assembled by hand. If the force is indeed electrostatic and scale invariant, then shrinking the size of the model could only help in thrust-to-weight ratio. Hand fabrication at the centimeter scale is difficult, so we turned to rapid prototyping techniques. Using laser cutters and 3D printers allowed us to quickly make and test design modifications as well as achieve some degree of fabrication precision.

Methods

Accurately measuring changes in mass to within 0.1 mg would typically require the use of an enclosed digital scale, but available tools were found to be inaccurate in the presence of high electric fields. To combat these issues, a 3D printed testing apparatus was developed. With this setup, the forces on the craft could be measured accurately and easily. The 3D printed system is made up of two separately printed pieces: an ionocraft frame and a measurement base (Figure 3.1).

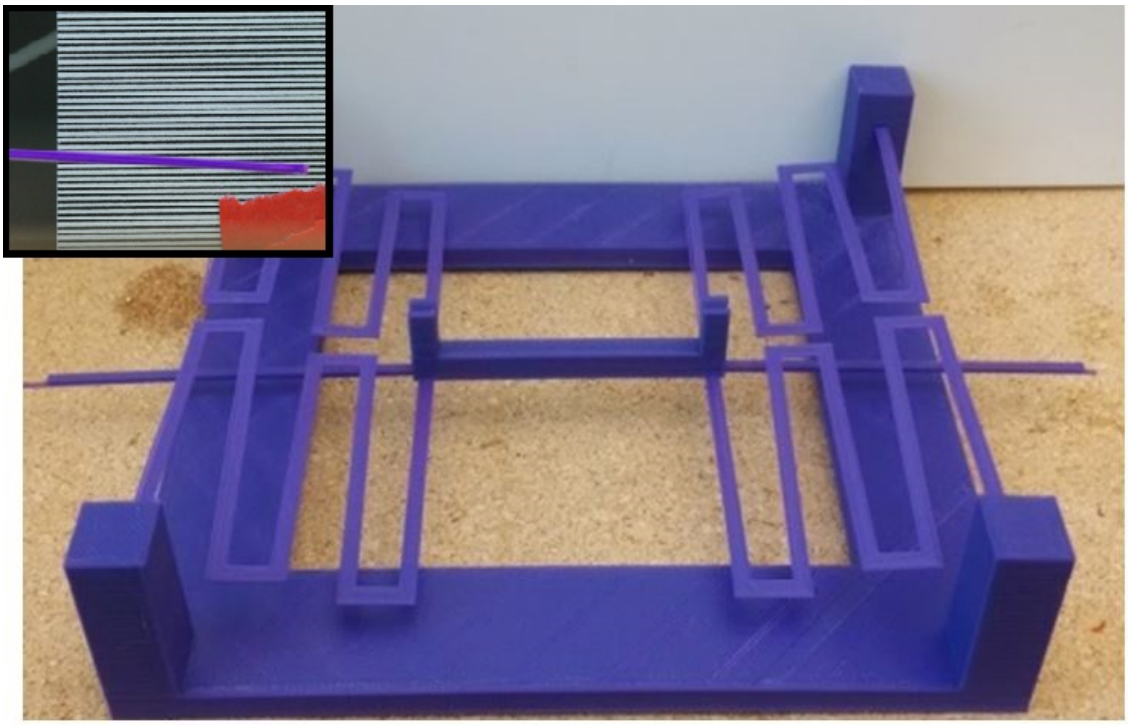

Figure 3.1: A fully assembled testing aparatus used to determine ionocraft output force. It is comprised of two 3D printed components: a serpentine spring frame and a square base.

The ionocraft frame functions as the internal structure and support. The capability for rapid iteration provided by the 3D printer allows for testing of the relationship between geometry and output force. Two notched posts allow for suspension of a wire across them while the curved bottom section allows for a bottom electrode or "skirt", in this case made of aluminum foil, to be stretched across it. The three main parameters then varied are wire to skirt distance as controlled by the post height, skirt radius, and skirt length. The ionocraft frame has long folded springs that are inserted into the measurement base. This suspends the ionocraft frame in the air so the balance of forces between its weight and produced thrust can be measured. These 3D printed springs were found to be linear in the desired region of operation and to have a total spring constant between 1-2 N/m.

A test setup was developed to measure the current consumption as well as the output force of the ionocraft. A resistor was connected in series with the ionocraft to measure current, and a high resolution camera was used to measure output force. The two long beams that extend axially from the 3D printed device shown in Figure 3.1 are used to measure the displacement of the ionocraft that has been assembled at the center. This is accomplished by placing one of these beams directly in front of a repeated black and white striped pattern of known period. The experiment is performed by increasing the voltage across the ionocraft in discrete increments. For each voltage value, the voltage across the 2MΩ series resistor is measured to determine the current, and an image is taken.

To determine the force output from the ionocraft, the displacement of the long beam must be determined. This beam can be located precisely by fitting a Gaussian profile to a filtered form of the image shown in Figure 3.1 (inset). This filter amplifies the purple signal of the beam while filtering out the black and white lines. Once this beam's location is known relative to the image, the black and white periodic signal is used to determine the absolute displacement of this location from the beam's original location. This displacement is then multiplied by the previously measured spring constant to find the ionocraft output force.

With experimental results demonstrating the feasibility of electrohydrodynamic flight at this scale, the next step was to fabricate a full, free-standing ionocraft with minimal total mass. Balsa wood was chosen for the frame material due to its extremely low density and ability to function as an electrical insulator. However, even though balsa is typically considered an easy material to work with, the required sub-millimeter precision necessary for these craft was not attainable with hand tools. The solution was to use a laser engraving machine, allowing fabrication of designs starting from computer drawings reproducibly, quickly, and in batches. Additionally, a wet etchant was used to decrease the mass contribution of the aluminum "collector." Combining these methods yielded ionocraft prototypes with total mass under 100mg (see Figure 3.2).

For control, a microcontroller (GINA [58]) containing a 9-axis IMU was used to determine the angular displacement in real time and transmit the data wirelessly. A PD controller was implemented using the PWM output voltage of the microcontroller as the control signal in conjunction with the high-voltage control circuit; the full system diagram is shown in Figure 3.3. Measurements from a three-axis gyroscope are used with a quaternion transformation to find the current angle of the ionocraft. Because the device geometry affords only

Figure 3.2: Fabricated meso-scale ionocraft. Components: Tungsten wire (50μm diameter), aluminum mesh, balsa wood frame.

one degree of freedom for thrust, it was necessary to constrain the other axes with a simple "seesaw" test setup.

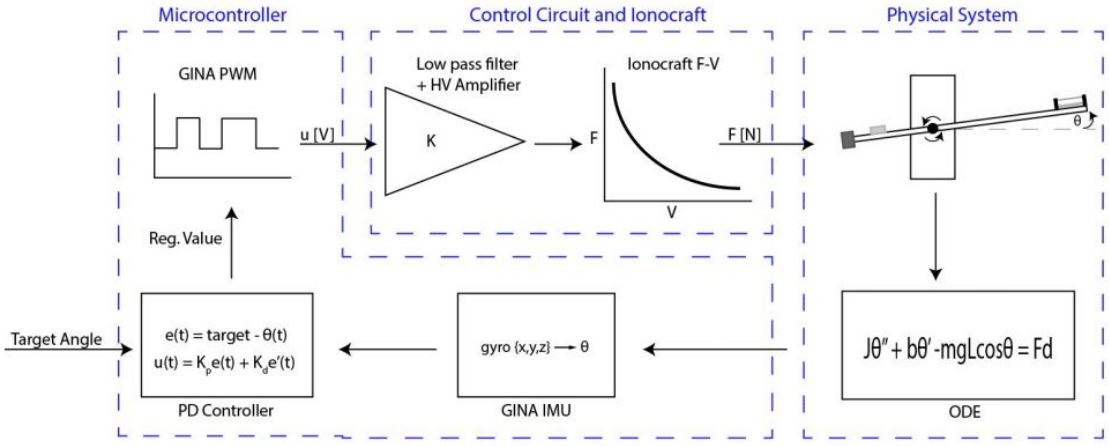

Figure 3.3: Full system block diagram.

Results and Discussion

In the fabricated device there is not a uniform 2D body of charge as assumed in the standard EHD force equation. However, agreement between the theoretical and experimental force curves in Figure 3.4 implies the device is generating thrust at a magnitude approaching the theoretical limit. As the characterized device masses about 75mg, generated force of roughly 0.75mN is the minimum for tethered flight; the peak measured force exceeds a thrust to weight ratio of 1.5:1, indicating controllable flight is possible.

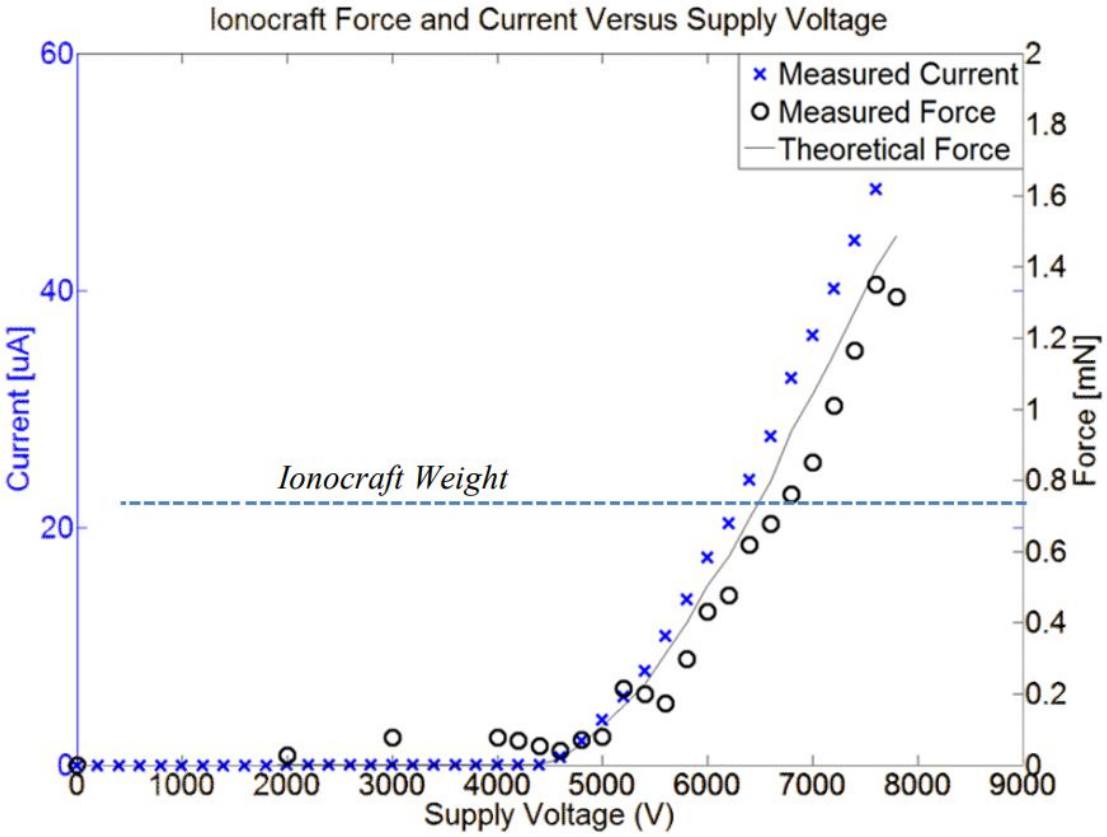

Figure 3.4: Plot showing measured force and current versus supply voltage for ionocraft with a 4mm gap between electrodes.

The system was modelled in MATLAB for design of the feedback controller. Model parameters were first tuned to fit empirical data. Despite the linearization of multiple system blocks, the experimental step input response was similar to the simulated performance, as can be seen in Figure 3.5. Attitude-based feedback control was successfully demonstrated. Nonlinearities in the physical test setup led to more repeatable performance when the system was underdamped. The presence of steady state error indicates an integrator term should be incorporated in future versions of the controller.

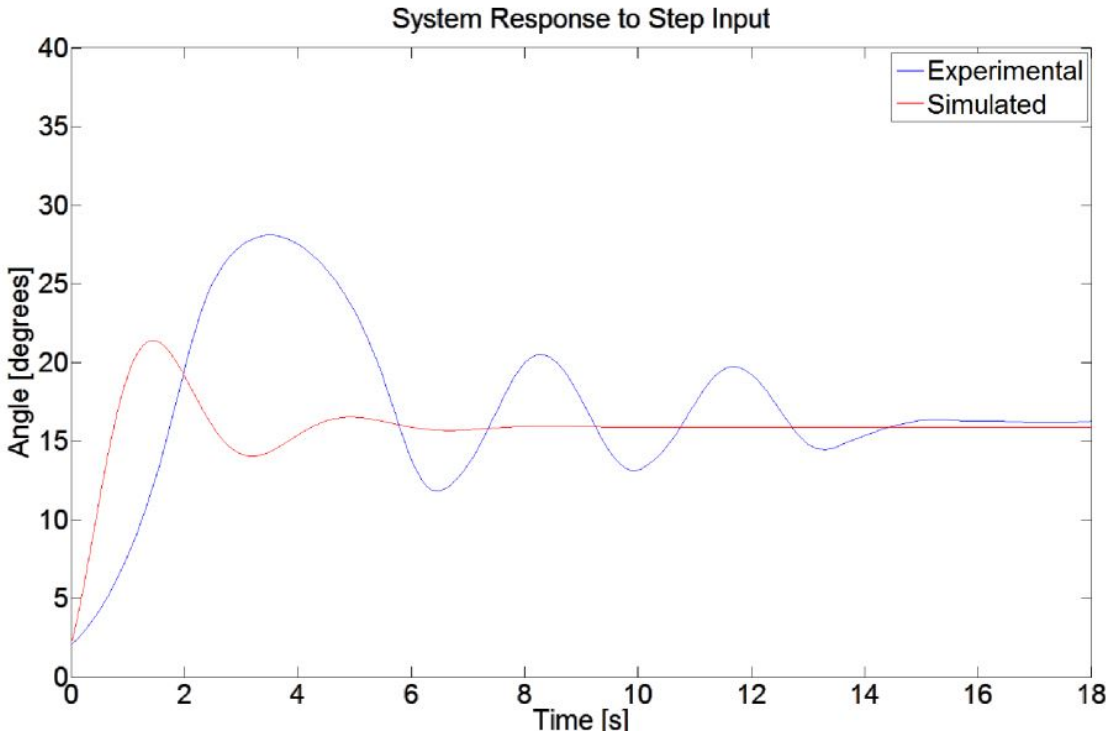

Figure 3.5: Simulated and actual system responses with PD controller implemented. The presence of ringing and a significant settling time in the experimental data indicate the system is underdamped. Kd = 0.183, Kp = 0.43.

Contributions and Conclusions

Succinctly, the contributions of this work were:

- The smallest, lowest voltage EHD-powered flier to demonstrate repeated takeoff.
- The first documented feedback control of an EHD-powered flier in a constrained environment.

The largest challenge was with repeatable operation. There was a good deal of device variation stemming from both fabrication and assembly. For example, if the emitter wire was not properly tensioned, it would be electrostatically attracted towards the collector and create a failure point wherever it was lowest. Surface breakdown along the balsa wood dielectric standoffs was a significant problem, as they seemed to pick up static charge worse than expected. Oxidation of the tungsten emitter wire was evident over time; although it could be (carefully) cleaned by hand, this limited experimentation time. Overall, the conclusion was that while this was a strong indicator that we would be successful in scaling an EHD-powered flier down to the centimeter-scale, we would require significant advancements in electrode fabrication and robot assembly.

3.2 An EHD Thruster Using Microfabricated Silicon Electrodes

This work was published and presented at the 2017 International Conference on Micro Electro Mechanical Systems (MEMS) [20].

Motivation and Brief Description

If, in theory, EHD electrodes are only required to be electrically active and not used structurally, then we should be able to produce devices with a high thrust-to-weight ratio by using very thin planar geometries. Given a positive corona discharge, material choice should not actually matter (See Section 2.1). Standard MEMS techniques allow for the definition and release of planar structures ranging in thickness from a single to dozens of microns.

Prior work had identified the need for extremely uniform electrodes, ideally without the need for external fixtures for tensioning/stretching. Prior work had also demonstrated that even 40μm thick silicon (SOI device layer) was remarkably simple to handle with tweezers. Microfabricating individual electrodes and assembling a millimeter-scale thruster by hand seemed like a natural evolution given the research group's expertise in SOI wafer processing.

Electrical characterization was performed to analyze the effect of inter-electrode gap and emitter electrode width on corona discharge and compare findings to simulation; this would be an important test of microfabricated silicon as a replacement for more standard electrode materials.

Methods

Devices are fabricated in a two mask SOI process and individually plasma diced. The corona emitter wires have cross sections ranging from 10µm × 40µm to 50µm × 40µm. The collection grids were typically 6mm squares, with 50µm wires on 500µm centers, a compromise between smooth electric fields (approximating a point-plane system) and lower air flow resistance.

For electrical characterization, glass cover slips are used to vary the inter-electrode distance (Figure 3.6). High voltage was supplied to the emitter wire by a Gamma High Voltage 10kV supply and current was measured by a benchtop ammeter connected to the collector grid. The power supply is current limited to protect the ammeter. Contact is made with tungsten probe tips.

Outlet air velocity measurements were performed using a TSI AVM430 hot wire anemometer placed two millimeters below the collector grid.

Results and Discussion

The presented data is from a range of fabricated devices, replaced when failure during testing caused obvious damage (e.g. arcing events).

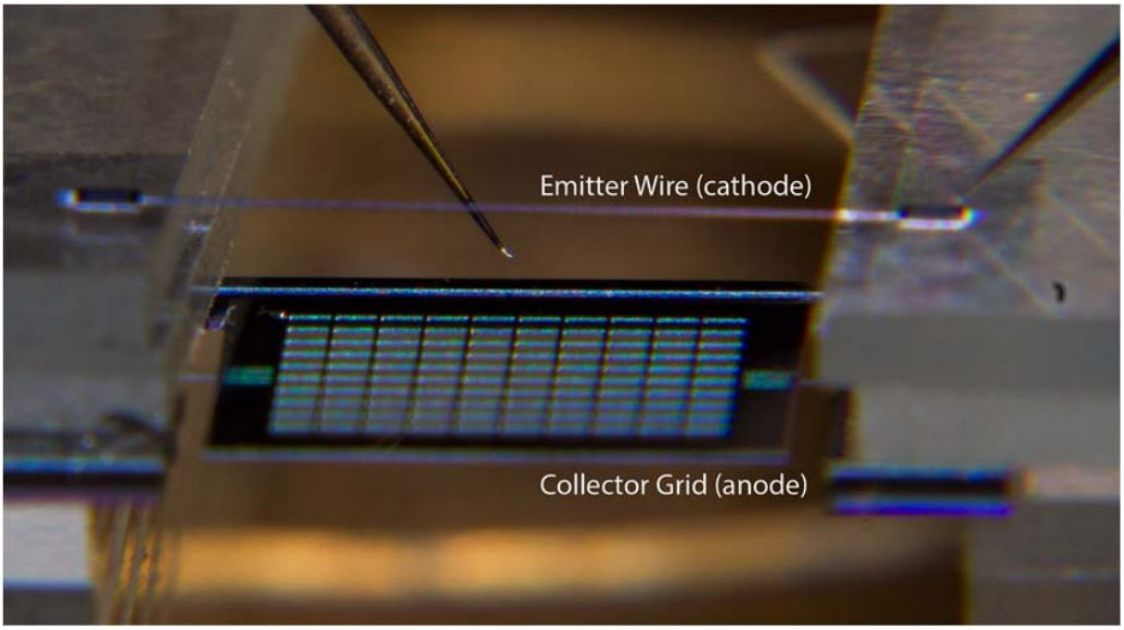

Figure 3.6: Electrical testing was performed at a probe station. Glass cover slips were used to vary the inter-electrode distance and contact was made via tungsten probe tips. The collector grids were elevated from the probe station chuck by glass slips.

Electrical Characterization

Figure 3.7 shows measured voltage versus current relationships for devices with three different inter-electrode spacing. A 50μm wide emitter wire is used for each. Figure 3.8 shows measured IV curves from devices with a constant inter-electrode spacing and varying emitter wire widths.

Plotting I/V as a function of V allows us to relate this gathered electrical data to the Townsend relationship (Equation 2.1). The value of C can be found from the slope, while the intercept represents the corona onset potential. Onset potential found by this method, through the simulation method described previously (Section 2.3), and by Peek's analytical formula are shown in Table 3.1. It is important to note that both the Peek's equation and the simulation method treated the emitting wire as having a circular cross section equal to the wire width instead of the actual rectangular cross section.

The results show that scaling the rectangular wire width does not strongly correlate with a decreased corona inception voltage as would be predicted from our circular cross section approximation. The experimental results for varying gap distance of the 50μm wire agree with simulated and analytic results within 10%. Lack of agreement for the 10, 20, and 30μm values indicate that scaling the wire width does not change the critical radius of curvature that amplifies the local emitter field.

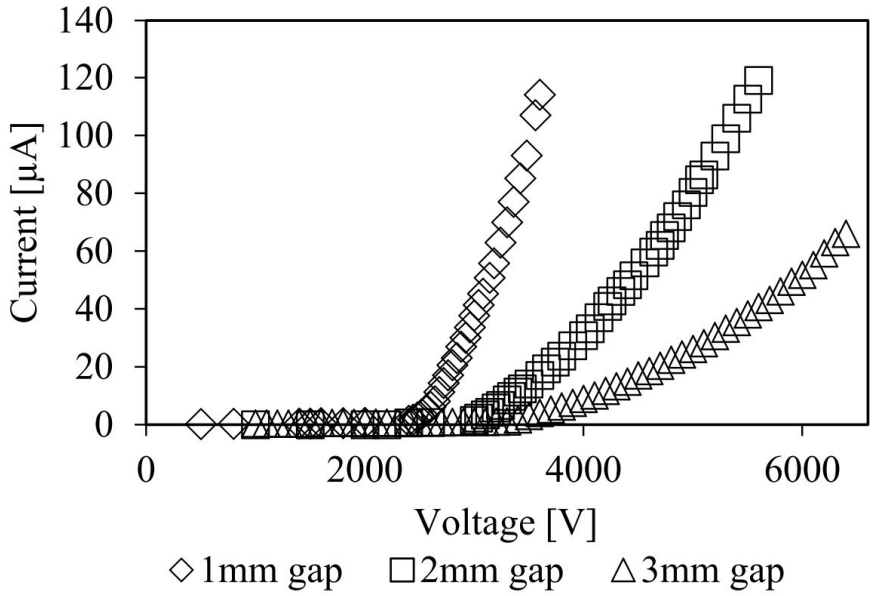

Figure 3.7: Current versus voltage for varying inter-electrode gaps: 50μm wide wire, 6mm × 6mm grid.

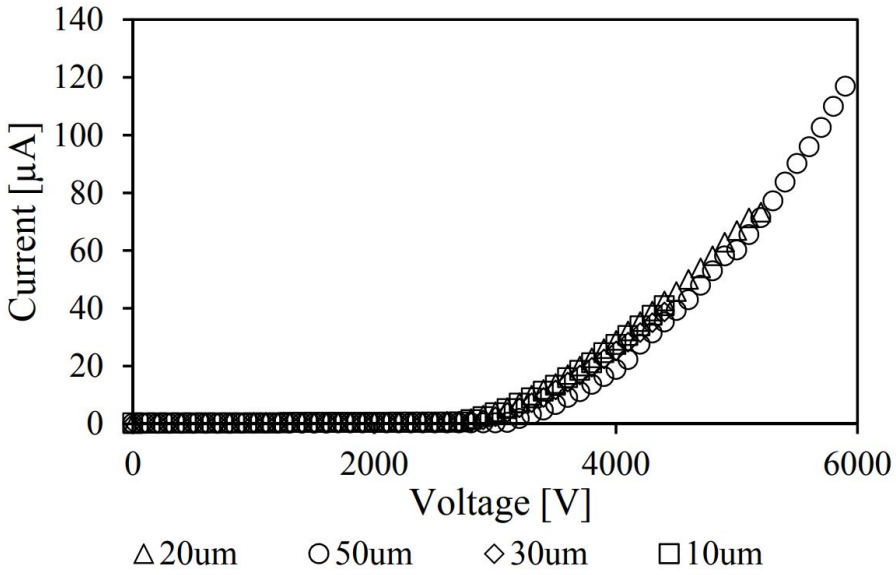

Figure 3.8: Current versus voltage for varying emitter wire widths: 2mm inter-electrode gap, 6mm × 6mm grid

Table 3.1: Corona inception voltage (in kV) calculated by three different methods for varying electrode geometries.

Width (μm)	10	20	30		50	
Gap (mm)	2	2	2	1	2	3
Peek's	1.45	1.89	2.21	2.31	2.67	2.89
Sim.	1.50	2.00	2.35	2.50	2.85	3.25
Exp.	2.76	2.75	2.85	2.51	2.99	3.28

Thrust Measurements

Thrust produced by the engines was first characterized indirectly by the outlet air velocity as measured by hot wire anemometer. The results for 2mm and 3mm electrode gaps with a 50μm wide wire over a 6mm grid are shown in Figure 3.9.

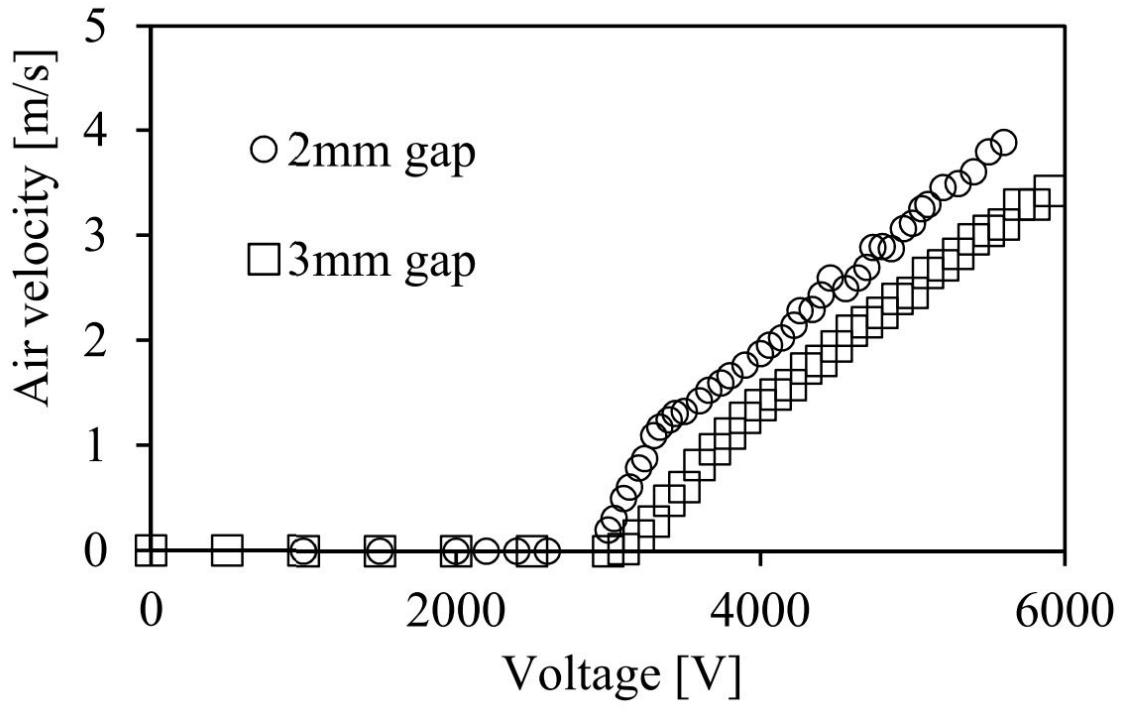

Figure 3.9: Air velocity versus voltage for varying inter-electrode gaps: 50μm wide wire, 6mm $\times$ 6mm grid.

Using the grid without its surrounding frame as the control area, thrust can be deduced

from the simple mass flow equation, with A representing the flow outlet area, ρ the density of air, and v_e the outlet flow velocity:

$$F = ma_e = \rho A v_e^2 \tag{3.1}$$

Thrust was then measured directly by assembling a thruster on the end of a roughly one-meter long balsa wood pendulum with a pin pivot at the top. With the total mass and center of mass known, observing the angular deflection at the tip of the rod and solving the torque balance equation determined the output force. The resulting rod deflection for various data points is shown in Figure 3.10. Tests were performed with a 50µm wide wire and a 2mm electrode gap.

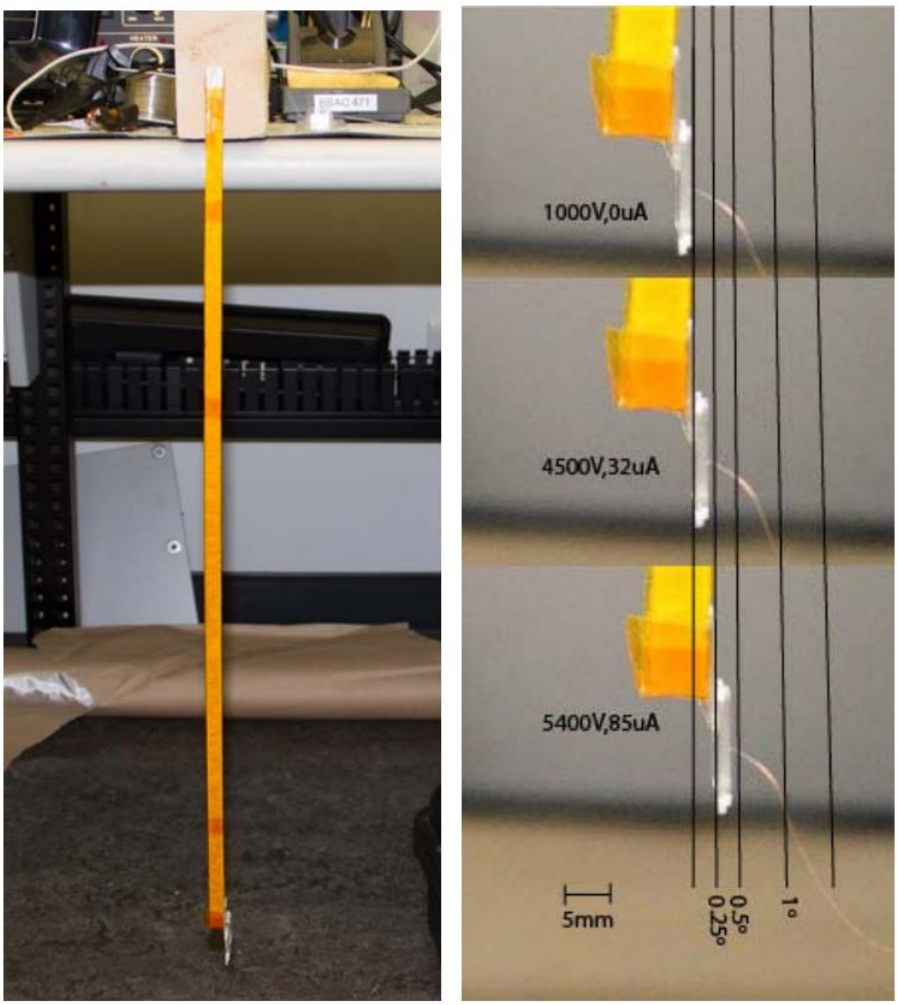

Figure 3.10: Direct thrust measurements by deflection of a physical pendulum. Current and voltage information was collected alongside video and then still frames were extracted to take individual data points.

The forces, measured directly by the deflection of the pendulum and indirectly by the outlet air velocity, are compared to the theoretical electrostatic force to find the geometric loss factor (Equation 2.14). The two methods agree to within 20% and yield an average loss factor of 48% ($\beta = 0.52$). These results are shown in Figure 3.11. Possible sources for this loss factor include drag on the grid wires, horizontal force vector components due to electrode asymmetry, and atmospheric conditions affecting ion mobility.

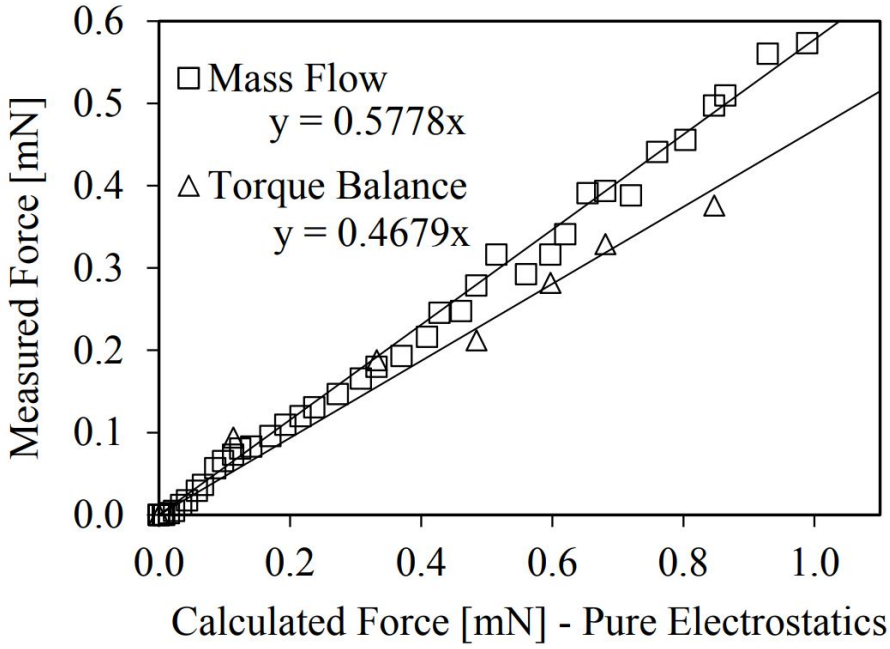

Figure 3.11: Plotting theoretical electrostatic force versus experimentally measured force for extraction of the geometric loss factor.

Outputs were stable over a roughly ten second period per each data point during the mass flow experiments. Devices could be retested with consistent results after the thirty-minute experiment was complete.

Assembly

Dielectric standoffs as tall as the desired inter-electrode gap are necessary to produce a low-mass free-standing device with the microfabricated electrodes. Re-designed structures include an attachment mechanism consisting of guiding slots and locking cantilevers. Coated silica capillary tubes with 450µm OD and 25µm wall thickness were inserted into these points and then secured with UV-cured epoxy applied by probe tip. This process leads to the type of device shown in Figure 3.12, with a total mass of 2.5mg.

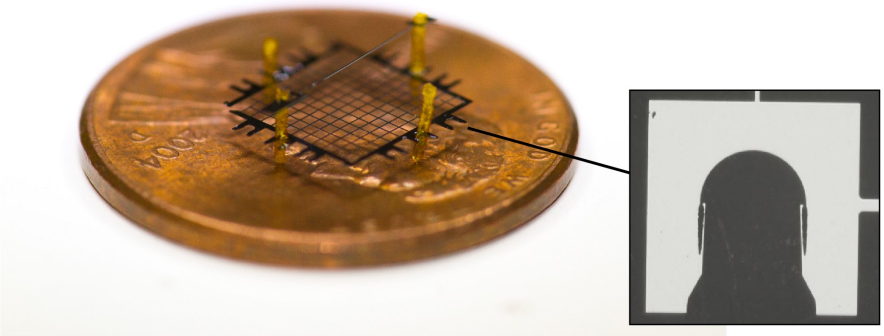

Figure 3.12: The microfabricated silicon components and silicon capillary tubes were assembled by hand. This roughly 100 cubic millimeter device has a mass of about 2.5mg. Inset: Attachment mechanism with guiding slot and locking cantilevers.

Contributions and Conclusions

Succinctly, the contributions of this work were:

- A feasibility proof for hand-assembly of microfabricated silicon electrodes for use in a standalone EHD device.
- A roughly 100 cubic millimeter, 2.5mg thruster was assembled with a thrust to weight ratio exceeding 20. This is the smallest, highest thrust-to-weight ratio standalone EHD thruster ever demonstrated.
- Electrical characterization and direct force measurement from microfabricated silicon EHD thrusters, the latter being a novel measurement.

This work was a sufficient demonstration of EHD from microfabricated silicon electrodes to warrant further investigation. There was still a distinct need to improve operating voltage, device assembly, and to further investigate thrust efficiency loss mechanisms. In particular, the fact that operating voltage was not a function of drawn emitter wire "width" showed that the naive approach to improving the emitter geometry would not work. The various failure modes stemming from poor design choices (e.g. not rounding the emitter wire "handling tabs") were all important to keep in mind for future work.

3.3 Pushing the Limits of Corona Scaling for Microfabricated Silicon Electrodes

This work was published in the journal Micromachines as an invited contribution to the Microplasmas special issue [19].

Motivation and Brief Description

Prior work had shown that there is a limit to the operating voltage scaling of microfabricated silicon electrodes by simply altering drawn width. Moving forward, there are two main avenues to explore: decreasing operating voltage strictly through inter-electrode distance scaling, and decreasing operating voltage via more complex alteration of the geometry of the emitter wire. As SOI wafer scale fabrication is a relatively simple and scalable technique, we would prefer to make any design changes compatible with this process.

In this work, an array of hybrid wire-needle and grid electrode geometries were fabricated and characterized to attempt to minimize both corona discharge onset voltage and thrust loss factor. Statistical analysis of this dataset was performed to screen for factors with significant effects. An optimized emitter electrode decreased onset voltage by 22%. Loss factor was found to vary significantly (as much as 30%) based on collector grid geometric parameters without affecting discharge characteristics.

Methods

Electrode Design and Fabrication

Devices are fabricated in a two mask silicon-on-insulator process and individually plasma diced, as described in [18]. The corona emitter wires have nominal cross sections of 40 μm by 40 μm. The silicon resistivity ranges from 1 to 100 Ω·cm.

Emitter wires with periodic protrusions of various shapes and collector grids with varying wire separation and width were fabricated. Figure 3.13 depicts both of these types of geometries. Table 3.2 shows the range of swept features. They include tip angle, spine separation and height, and whether the wire is populated with spines on one or both sides.

Characterization Setup

A Gamma High Voltage supply with 10 kV maximum voltage and 500 μA maximum current is used for electrical testing. A HP benchtop multimeter with a resolution of 100 nA is used for current measurements. A TSI AVM430 hot wire anemometer with a resolution of 0.01 m/s is used for air velocity measurements. The edge of the anemometer inlet is placed within a millimeter of the grid, while the actual hot wire is approximately 2 mm away axially. The anemometer inlet width is about 5 mm, meaning it should collect the full grid outlet airflow without needing to take measurements at multiple points along the

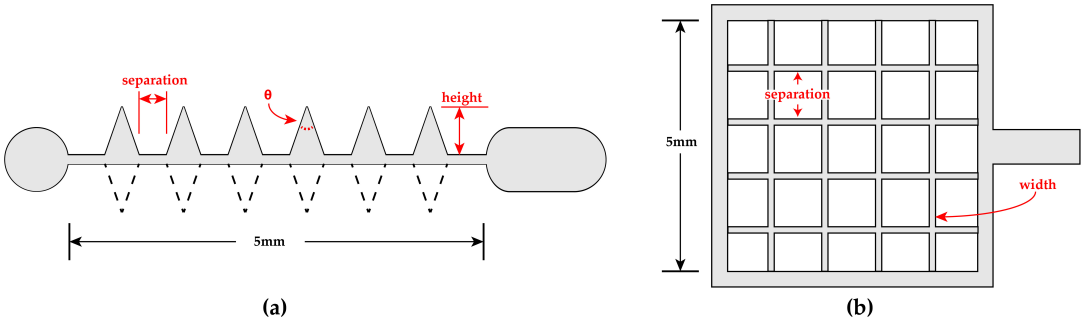

Figure 3.13: (**a**) The emitter wires have triangular protrusions ("spines"). The distance between spines, height, and tip angle are all varied. Some wires are created with spines only along one half of the wire, while others are fully populated. In all cases the cross section of the rectangular portion of the wire is 40 μm by 40 μm; (**b**) Silicon collector grids have varied separation and wire width. The grids are designed to keep the total interior area constant at 25 mm^2. Because the wire width is also controlled, the separation is scaled around the set point to accomplish this. In all cases the thickness of the grid is 40 μm.

Table 3.2: The electrode geometric factors and their values that were investigated in this work.

Emitter Wires				**Collector Grids**	
Separation	**Height**	**Angle**	**Fill**	**Separation**	**Width**
250	250	15	Half	250	10
500	500	30	Full	500	25
750	-	45	-	750	50
1000	-	-	-	1000	-
-	-	-	-	1250	-

channel. A depiction of the test setup is shown in Figure 3.14. Velocity measurements are internally filtered by the anemometer using a moving average with five second time constant. During testing both the current and velocity were allowed to settle (between 5 and 10 s) before recording the data point.

Output force is calculated using simple momentum theory, where $F = \dot{m}v_e = \rho A v_e^2$. The entire interior area of the collector grid (5 mm×5 mm) is used as the outlet area. This assumes a negligible inlet velocity and a uniform outlet velocity (V_e). Previous EHD research showed severe overestimation of thrust by using outlet air velocity as opposed to a scale [62], noting that a single velocity profile is insufficient to accurately calculate the volumetric force. We expect this problem to be less significant both for thrusters of the scale shown here, where the outlet is on the order of the measurement apparatus inlet, and for our test setup, where the outlet flow is ducted by the dielectric standoffs. Previous research

has shown fair agreement between mass flow calculations and more direct methods of thrust measurement for similar electrode arrangements [20].

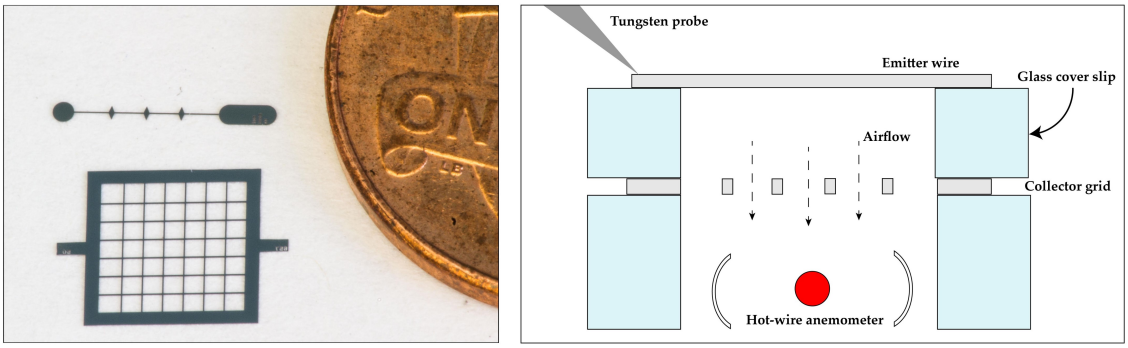

Figure 3.14: (**a**) A pair of fabricated electrodes next to a U.S. one cent coin for scale; (**b**) A schematic view of the characterization setup. The entire setup is contained within a probe station. Distance between the electrodes is set by glass cover slips. The electrode set is elevated off the probe station chuck by glass spacers so that the conductive chuck does not interfere with measurements and so that the hot wire anemometer can be placed underneath the outlet. Not shown is the second tungsten probe tip which makes electrical contact with the collector grid and the third tungsten probe tip which makes mechanical contact with the other side of the wire to keep it stable during testing.

Results and Discussion

The presented data is from a range of fabricated devices. Statistical analysis was performed using JMP by SAS Institute.

Corona Inception Voltage and Current

A total of 21 different electrodes were characterized. In all cases a 500 μm grid separation was used. Electrodes were exchanged when catastrophic failure occurred (see Figure 3.21).

Corona inception voltages and C coefficient were calculated by plotting Equation (2.1) in terms of I/V. This method, as opposed to the method of finding the critical voltage with a μA transition, was deemed more reliable given the current resolution of the test setup. The C coefficient can be used as a rough quality factor when designing for high current discharge devices as long as the breakdown voltage does not decrease significantly between electrodes. R^2 vales above 95% were found in the linear fit for all cases.

Commercial software was used for modelling significance of the varied factors on two effects, V_{crit} and C. An ideal electrode has a low inception voltage and a high C. The

dataset was fit to the models using a standard least squares regression analysis. The results of these fits are shown in Figure 3.15.

Angle, fill (half or full rank of spines), and separation were all found to be statistically significant ($p < 0.05$) factors affecting inception voltage, with tip angle being the dominant factor. Spine height was found to be statistically insignificant. For C, emitter fill and separation were found to be the only two significant factors. These models allow us to generate prediction plots for the quantitative effect of the various factors on the response; these are shown in Figure 3.16.

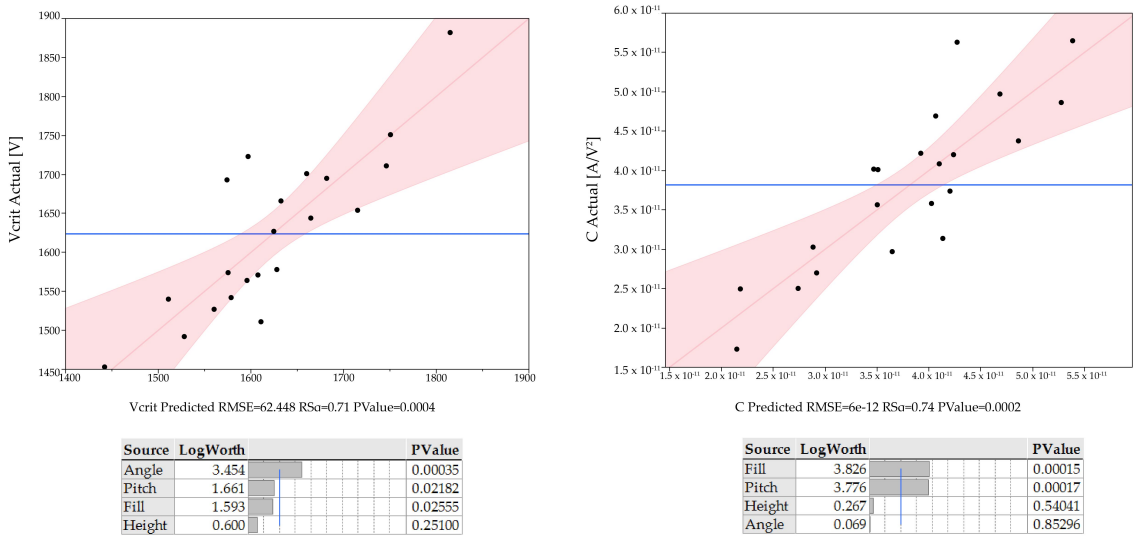

Source	LogWorth	PValue
Angle	3.454	0.00035
Pitch	1.661	0.02182
Fill	1.593	0.02555
Height	0.600	0.25100

(a)

Source	LogWorth	PValue
Fill	3.826	0.00015
Pitch	3.776	0.00017
Height	0.267	0.54041
Angle	0.069	0.85296

(b)

Figure 3.15: Response models generated by least squares regression analysis of the 21 run dataset. A p value below 0.05 generally represents a statistically significant factor (rejection of the null hypothesis). (**a**) The regression model for corona inception voltage; (**b**) The regression model for C coefficient.

By following these trends we can identify the two geometries that should independently have the lowest inception voltage and the highest C. This is confirmed experimentally as shown in Figure 3.17. The lowest measured inception voltage is 1453 V and the highest measured C is 5.65 $\times 10^{-11}$ A/V^2, as compared to the bare wire's 1981 V and 7.30 $\times 10^{-11}$ A/V^2. Noting that tip angle is the dominant driver of inception voltage and does not significantly affect C we can select an "optimized" design. At this point no weighting has been attached to the responses for a true optimization problem to be set up. The electrical characteristics of this geometry compared to the bare wire are also shown in Figure 3.17.

Loss Factor

Loss factor can be determined by plotting the theoretical electrostatic force (Equation (2.13)) versus the force measured using the grid outlet air flow. The slope of this line represents

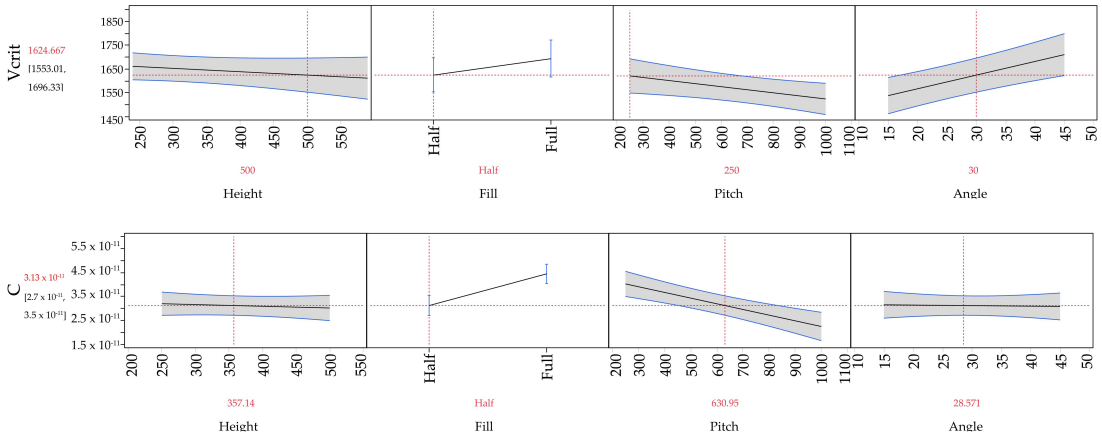

Figure 3.16: Response prediction profiles for the four factors varied in this experiment based on regression analysis for corona inception voltage (**top**) and for C (**bottom**). These plots in conjunction with the significance profiles from Figure 3.15 can be used to select an optimized geometry.

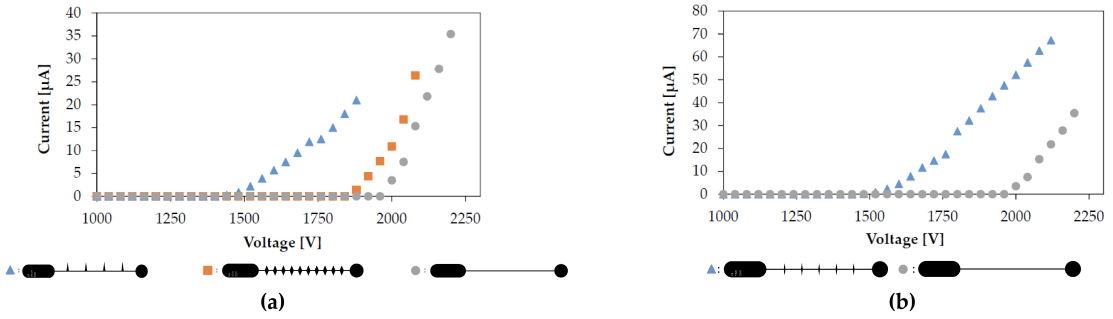

Figure 3.17: All tests performed with a gap distance of 500 μm and a collector grid separation of 500 μm. (**a**) The current-voltage characteristics of the lowest inception voltage configuration, highest C configuration, and a bare wire; (**b**) The current-voltage characteristics of the "optimized" wire, with separation of 750 μm, tip angle of 15°, height of 250 μm, and full fill. This electrode had an inception voltage of 1542 V and a C of 5.63 $\times 10^{-11}$ A/V^2.

the fraction of theoretical force being produced as measured output force in the preferred direction. An ion mobility of 2×10^{-4} m^2·V^{-1}·s^{-1} and the nominal electrode gap distance were used in the theoretical force equation in all cases. Although that means loss factor in this case will also include deviation in ion mobility from this value, that error will presumably be a static offset and it is still a useful tool to examine trends. This method was previously explored in [20], where a loss factor term β was introduced to Equation (2.13).

Grid wire separation is directly related to open area fraction. As shown in Figure 3.18, loss factor was found to be affected by this value without a change in discharge electrical

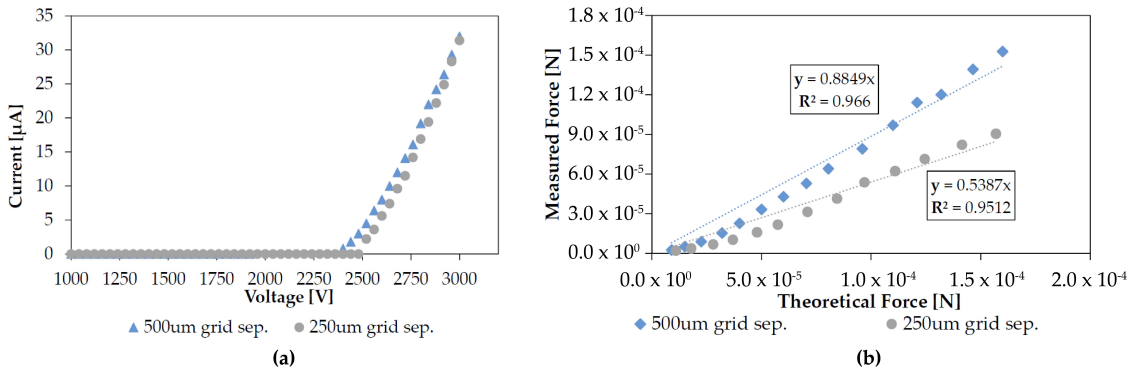

Figure 3.18: (**a**) Changing the grid wire separation from 500 μm to 250 μm had an insignificant effect on discharge characteristics with a bare wire at a 1 mm gap distance; (**b**) Decreasing the wire separation changed the loss factor by over 30%. Because there is no change in IV characteristics the increased losses can presumably be attributed to increased drag.

characteristics for some values of separation. For a 1 mm electrode gap, discharge with a 750 μm wire separation grid was inconsistent and sparkover occurred before discharge for all larger separations. For a 500 mm gap, however, discharge was consistently measured using 500 μm wire separations. At this time it is unclear what causes this discrepancy in stable gap-separation ratio.

Grid wire width was found to have a significant effect on loss factor. For a 500 μm wire separation grid, the open area fraction is about 91% for a 25 μm wire width and about 83% for a 50 μm width. This 8% change in open area fraction resulted in a 20% increase in measured loss factor, as shown in Figure 3.19.

Loss factor was found to be a strong function of electrode gap, as shown in Figure 3.20. With all other factors constant a 50% decrease in electrode gap increased loss factor by over 30%.

Failure Modes

Once the electric field reaches a critical magnitude dielectric breakdown occurs. The high voltage supply used during characterization has a current limit of 500 μA, which is typically reached during these sparkover events. The two most common catastrophic failure modes are for (1) the emitter wire to "pop" and break somewhere in the vicinity of the center or (2) for the collector grid to be physically damaged in the vicinity of the sparkover point. The latter case is shown in Figure 3.21.

The fact that tip angle does not have a statistically significant effect on current generation seems to indicate that the corona plasma is highly localized; this is supported visually by the visible corona plasma being confined to the tips, as shown in Figure 3.22. This contrasts with [24], which noted an effect of the tip angle used for emission on corona discharge

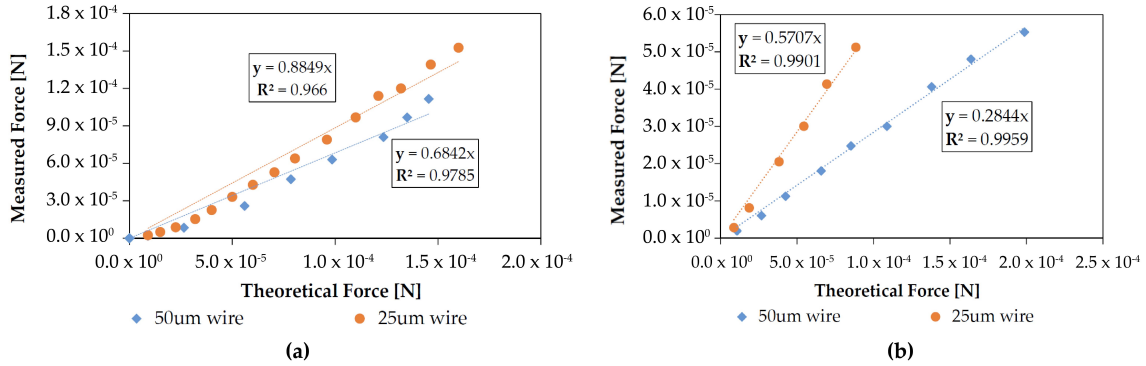

Figure 3.19: Both of these figures are for 500 μm grid wire separations with a bare wire as the emitter electrode. (**a**) Changing the grid wire width from 25 μm to 50 μm at a 1 mm electrode gap increased loss factor by about 20% without a significant effect on discharge current; (**b**) Changing the grid wire width from 25 μm to 50 μm at a 0.5 mm electrode gap increased loss factor by about 19% without a significant effect on discharge current

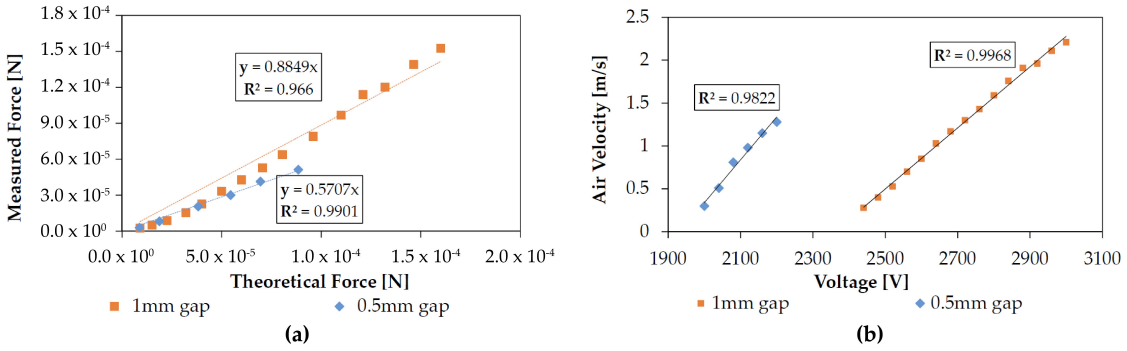

Figure 3.20: (**a**) Changing the electrode gap distance from 1 mm to 500 μm with all else held constant increased loss factor by over 30%. Test performed with a bare wire, a 500 μm grid wire separation, and a 25 μm wire width; (**b**) Measured outlet air velocity versus applied voltage for the two electrode gap distances. As expected by combining Equations (2.13) and (2.15) with the mass flow equation, the voltage-velocity relationship is linear above the corona onset voltage.

current. Further analysis of the dataset shows that there is a significant correlation ($p = 0.01$) between the number of tips and C. Because the height of the spines did not have a clear effect on either the inception voltage or the discharge current, it may be possible to design a new geometry that increases C without affecting onset potential; for example, a move from triangular spines to a triangle-on-a-post.

Increased corona inception voltage for small tip separation may be explained by a shielding effect similar to that noted in both field emission array literature and in multiple-needle

Figure 3.21: A typical failure mode of an electrode set. Permanent damage is sometimes observed following sparkover from a wire tip to the collector grid. This may be due to the relatively high current density following dielectric breakdown causing rapid Joule heating in the grid wires, or due to physical ablation during the high current breakdown. After a destructive event such as this, both electrodes were replaced despite there being no visible damage to the emitter wire.

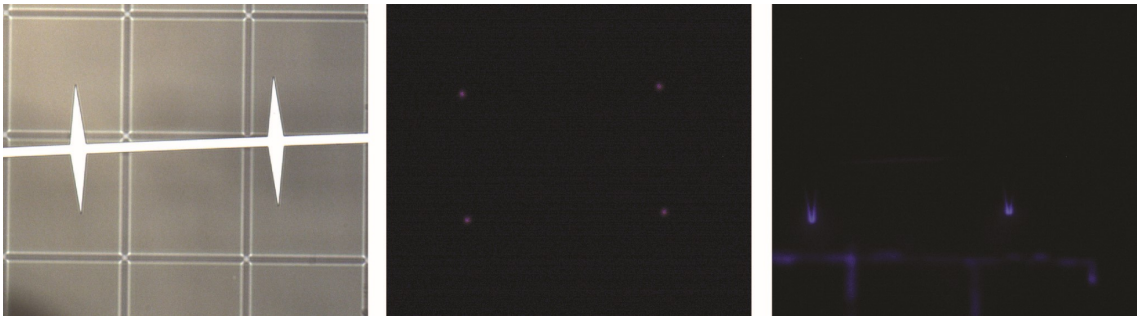

Figure 3.22: The corona discharge is characterized by a purple/violet glow visible in low light conditions. With the probe station door shut during electrical testing it was possible to take still images capturing the corona plasma. The first pane is the device with the light turned on, before testing. In the middle pane the device is at about 2500 V applied potential, where the plasma is clearly localized to the spine tips. The third pane is a still frame taken during a sustained breakdown event after the device had failed around 3000 V.

corona discharge studies. Although we expect to see some coupling between minimum separation to avoid shielding and height of the tips, there is no evidence of that with the currently fabricated device geometries.

Although positive corona discharge is primarily driven by geometry and electrode material choice is unlikely to strongly affect operating voltage, the catastrophic failure mode sometimes exhibited may be related to material properties (e.g., resistivity). Metal emitter electrodes in sub-millimeter corona devices have their own unique failure modes, including mechanical yield [85]. Therefore, instead of switching materials entirely, a first step would be to investigate the effects of silicon doping concentration on device performance. Regardless, in an autonomous microrobot it is unlikely that the power circuitry would be able to supply

current far in excess of the maximum operating point, perhaps negating this issue.

Holding all other factors constant and decreasing the electrode gap distance increased the loss factor by around 30%. We attribute this increase to two related primary reasons: increase in the ionization region to drift region ratio, and increase in the percentage of collisions imparting horizontal momentum components. The former will influence the effective d of Equation (2.13) and the latter will break the assumption that all collision energy generates force in the preferred direction.

As electrode gap is decreased the grid wire separation must also decrease to prevent them from influencing the emitter field. Decreasing the grid wire separation from 500 μm to 250 μm was found to increase loss factor by about 30%. Interestingly, this is roughly the same decrease in open area fraction (about 10%) that caused a 20% loss factor change when grid wire width was varied. This would imply that edge effects at the grid wires and not just obstructed area plays a role in drag through the grid; this theory is supported by literature, where drag through a micromesh decreased when edges were beveled [67].

Contributions and Conclusions

Succinctly, the contributions of this work were:

- Demonstration that simple lithographically-defined asperities can significantly decrease the operating voltage of SOI silicon electrode corona discharge devices.
- A statistical analysis of the geometric factors affecting corona discharge inception voltage as well as subsequent ion current for microfabricated silicon emitters.
- An investigation of the effect of collector electrode geometry on EHD loss factor for various interelectrode distances, which may serve as a design tool for future researchers.

In conclusion, we have explored a method to lithographically define features that can be used to decrease operating voltage without unduly influencing discharge current. Further, we have attempted to test the limits of collector grid geometry scaling, demonstrating changes in loss factor of around 30% with no change in discharge current. Although the hybrid wire-needle design presented herein was successful in decreasing corona onset voltage, the current setup is not optimized for flow through the grid. Future work will investigate the limits of the scaling trends for lithographically defined emitter features in an effort to decrease operating voltage below 1000 V at an acceptable force loss factor; these electrodes will then be incorporated into future designs of flying ionocraft.

Chapter 4

Design and Realization of a Flying Microrobot

A robot must have the capacity for controlled motion. An EHD-powered flying robot will require thrusters in a configuration that allows for attitude and trajectory control, the ability to modulate the thrust, the ability to sense its environment, and the computation power to close a control feedback loop.

A design inspired by the success of the quadcopter, replacing the rotors with EHD thrusters, allows us to sidestep some of the unfavorable scaling laws of propellers while maintaining the ability to transfer domain knowledge from the rich world of quadcopter design and control. Without an aerodynamic control surface (e.g. a propeller or wing) we have effectively decoupled our force output scaling from the characteristic size of the robot.

Research questions to answer:

- Can a quad-thruster be designed with low enough airframe overhead for takeoff, ideally maintaining a high thrust-to-weight ratio?
- Can attitude control be demonstrated using similar control methods to a standard quadcopter?
- Can full robots be assembled reliably enough, and can device lifetime be extended long enough, to make control experimentation possible?
- Can an ionocraft carry a sensor payload that allows for stable flight without external sensing?

4.1 First Takeoff of a Centimeter-scale EHD Quadthruster

This work was published and presented at the 2017 International Conference on Manipulation, Automation, and Robotics at Small Scales (MARSS) [18].

Motivation and Brief Description

With prior work demonstrating the viability of an EHD thruster composed of microfabricated silicon electrodes, the next step was to design a system with the capacity for controlled flight. Assuming that the thrust can be modulated by changing the voltage applied to the emitter wires, the collector grids of four individual thrusters can be biased together. This is the key for creating the simplest feasible quad-thruster ionocraft; the collector grids make up the bulk of the airframe, with connections only for structural support.

Methods

Electrode geometries were chosen based on a combination of lessons learned from previous efforts to create meso-scale EHD thrusters (e.g. limits of repeatable gap scaling for a given emitter radius), availability of a stable fabrication process with the given wafer properties, and feasibility of hand assembly (e.g. minimum size to handle with tweezers). Devices are fabricated in a two mask silicon-on-insulator (SOI) process and individually plasma diced. The active electrode material is all device-side silicon, allowing for a high thrust to weight ratio as the force is a predominantly two dimensional effect. The process flow is depicted in Fig. 4.1. After the backside deep reactive ion etch, the devices are physically removed from the wafer with tweezers and etched with vapor HF to clear the buried oxide layer. Corona discharge is a strong function of electrode geometry; care must be taken in designing the electrodes to prevent early breakdown, reverse corona (where a plasma is formed around the collector), and wasted area. Exterior corners are filleted and only rounded shapes are used in non-functional area, e.g. near the dielectric standoff attachment points.

Fused silica capillary tubing with an inner radius of about $400\mu m$ and a wall thickness of $25\mu m$ is used for the dielectric posts that set the distance between the two electrodes. The device is designed so that they can be fabricated in a stack - a rendered depiction of the device assembly is shown in Fig. 4.2. An aluminum jig is used during the assembly process to assist with placement and alignment of the silica tubes. An assembled ionocraft is about 10mg and 1.8cm by 1.8cm (see Fig. 4.3). It takes roughly thirty minutes to assemble by hand.

During electrical characterization the quad-thruster is weighted down by glass cover slips so it remains stable. High voltage was supplied to the emitter wire by a Gamma High Voltage 10kV supply and current was measured by a benchtop ammeter connected to the collector grid. The power supply is current limited to protect the ammeter.

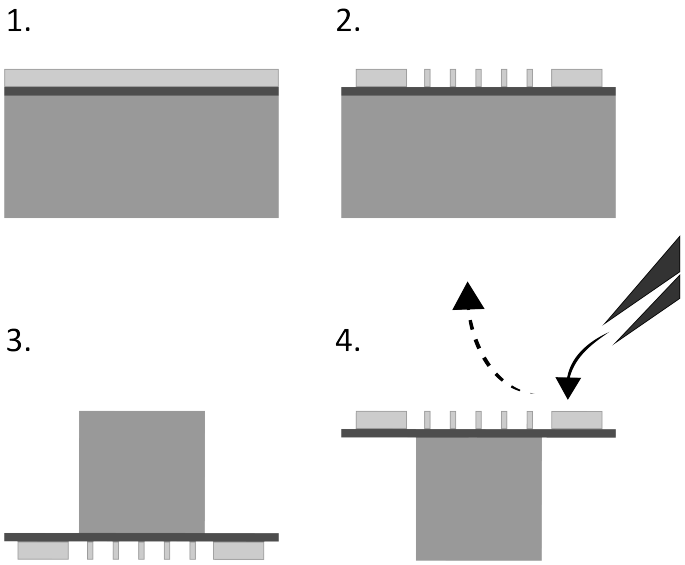

Figure 4.1: The simple two mask silicon-on-insulator (SOI) process to fabricate the silicon electrodes. First the $40\mu m$ device silicon is patterned. The wafer is flipped and loosely bonded to a handle wafer using a thermally conductive grease. The 500 μm handle silicon is aligned, patterned, and then etched to plasma dice the individual devices. Finally, tweezers are used to physically remove the electrodes, breaking the buried oxide in the process. The electrodes are placed into a vapor HF etcher to clear the remaining oxide.

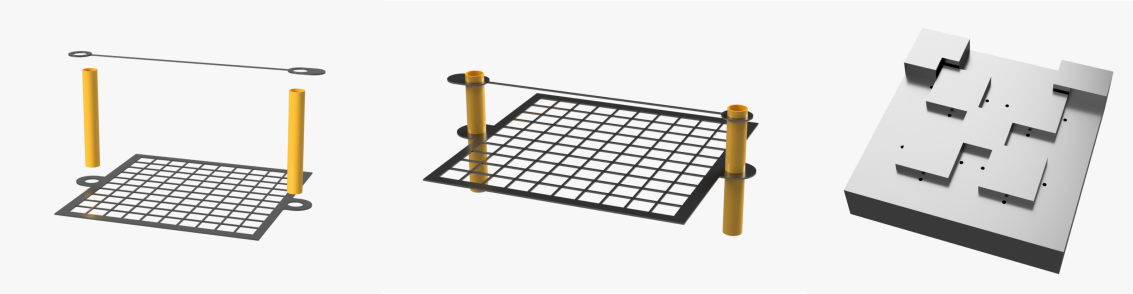

Figure 4.2: Fused silica capillary tubes are inserted vertically through slots in the micro-fabricated silicon electrodes and secured with UV-curable epoxy applied via probe tip. A machined aluminum fixture (far right) provides help with alignment and stability. Tabs on the emitter wire and collector grid (latter not shown) provide a place to attach the power connections using silver epoxy applied via probe tip.

Results and Discussion

The results are shown in Fig. 4.4 for both a full quadthruster, for two grids, and for one grid of the same device. Using Equation 2.13 with the loss factor for a similar electrode

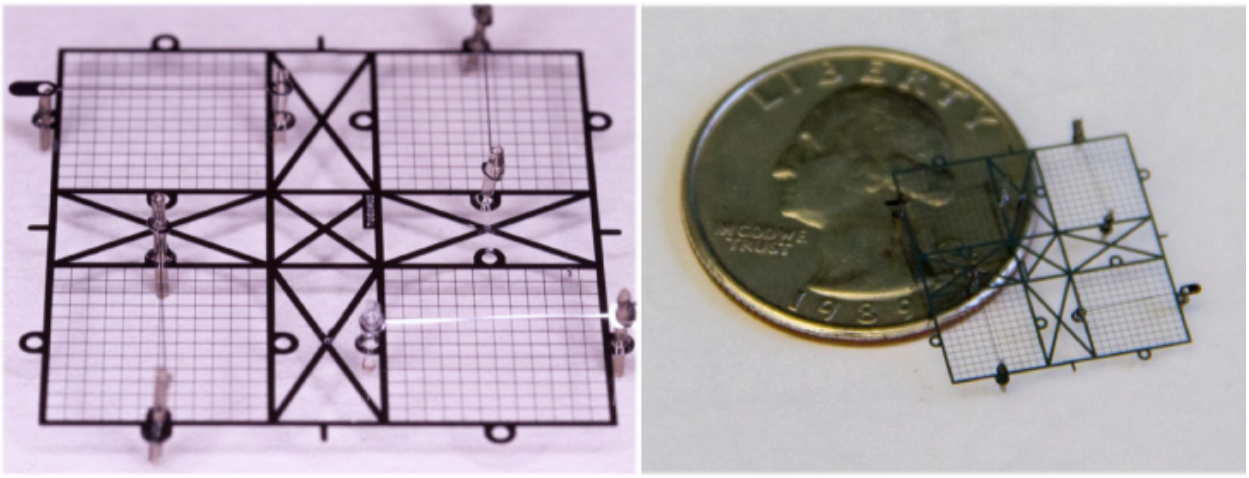

Figure 4.3: These "quad-thrusters" are made of microfabricated silicon electrodes and fused silica capillary tubes and assembled by hand. They are 1.8cm x 1.8cm, 10mg, with four individually addressable electrode sets, and a 1mm electrode gap. They should be capable of producing around 1mN of force for a thrust to weight ratio of about 10.

geometry found in [20] of 50%, a peak force for the quad-thruster of about 1mN is expected, corresponding to a thrust to weight ratio of 10.

Using $60\mu m$ diameter copper wires as the power connections the device was actuated in front of a high speed camera. At about 2400V the ionocraft took flight, reaching a peak altitude of around 5cm before the instability of its attitude caused a power wire to touch the collector grid. This flight is shown in Fig. 4.5. From this video a peak acceleration of about 2 gravities can be calculated, corresponding to a force of about $200\mu N$, far below the theoretical maximum force these devices should be able to provide. During the video the voltage was being slowly increased by hand and, due to the high thrust to weight ratio, the device took off and subsequently crashed before the voltage could be increased to the levels used to measure the maximum thrust point.

The goal of using four individually addressable electrode sets is to allow for attitude control similar to that of a quadcopter. As an initial feasibility test, only two of the four thrusters were actuated. As shown in Fig. 4.6, this created a moment around the center axis and the ionocraft flipped over as predicted. The question of how to control yaw remains open. A traditional quadcopter controls yaw by coupling torque from its rotors to produce a net moment around only one axis; the EHD thruster presented here has no analagous torque component. One possibility is to angle the emitter electrode along the vertical axis in order to produce horizontal force, although this would lead to decreased vertical force.

Contributions and Conclusions

Succinctly, the contributions of this work were:

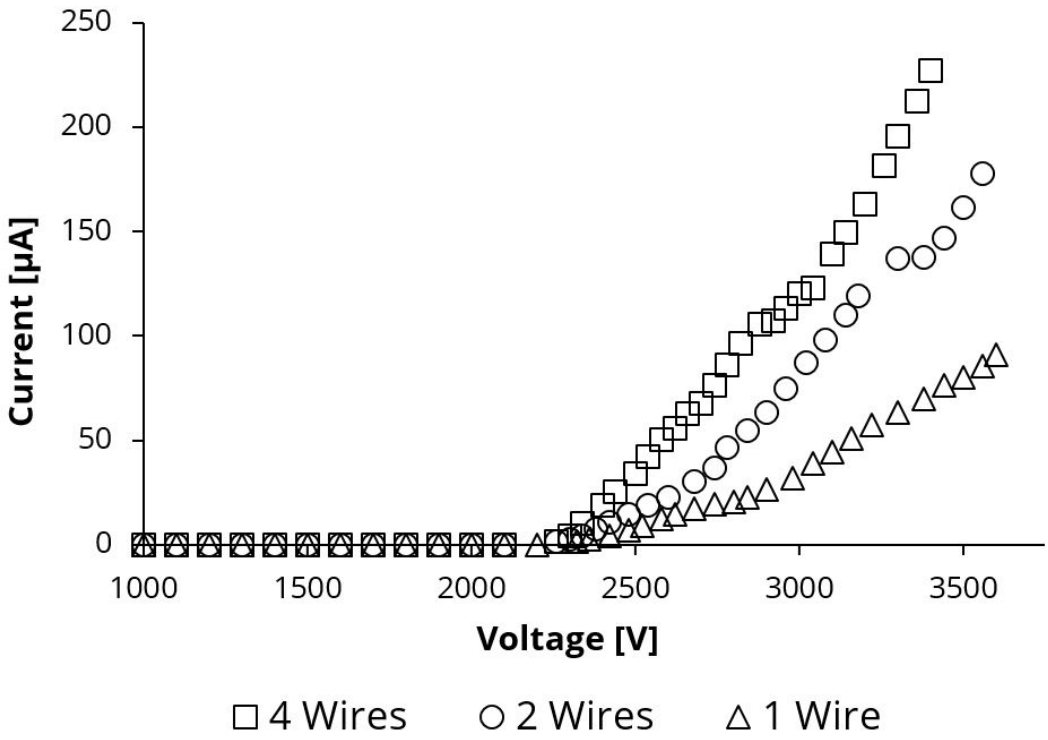

Figure 4.4: Electrical characterization of a quad-thruster with number of actuated wires varied. Calculated corona onset voltage is 2309V with a standard deviation of 50V. Measured currents agreed with geometric prediction (e.g. one wire produces one fourth the current of four wires at a given voltage) to within about 5% on average. Tests concluded when an arc occurred, destroying the wire.

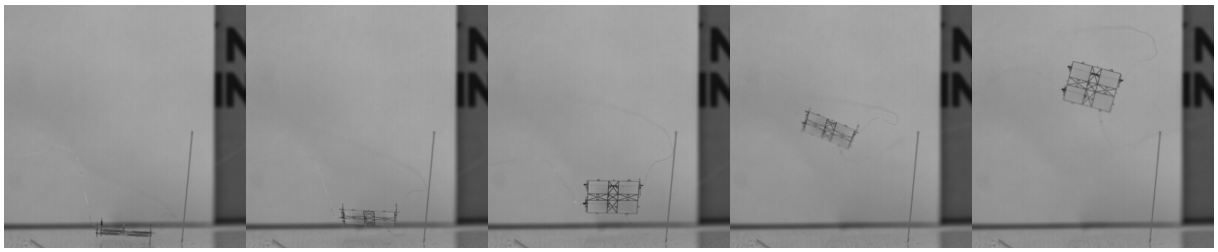

Figure 4.5: Takeoff of a microfabricated ionocraft captured at 1000fps. At about 2400V it took flight silently. The flight ended in around a second when the power connection became tangled with the collector grid, leading to an arc.

- The first takeoff of an EHD powered, centimeter-scale "robot" (as in, has the capacity for controlled flight).
- A feasibility proof for a quad-thruster design with minimal airframe mass overhead,

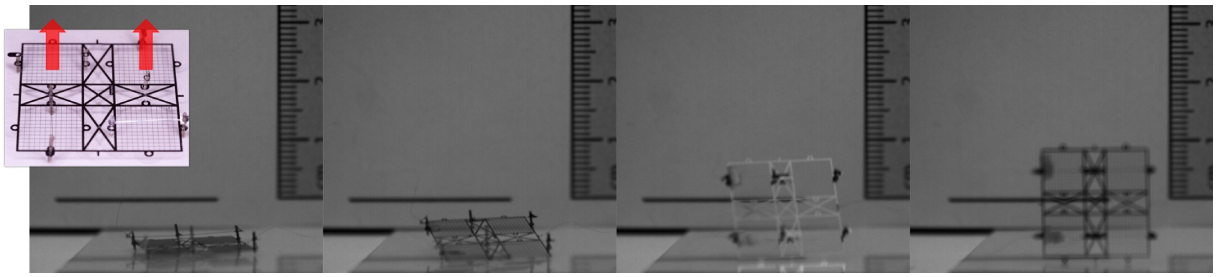

Figure 4.6: By applying voltage to only two of the four grids we can control roll/pitch of the robot. In this video, captured at 1000fps, the ionocraft flips over its center axis when the two rear thrusters are actuated at about 2400V.

enabling the highest thrust-to-weight centimeter-scale flier to date.

- A feasibility proof of using a quad-thruster design for attitude control.

The viability of the quad-thruster design had been proven, but there were major challenges with this iteration. The operating voltage was still too high; lessons learned in lithographic asperity definition for the emitter wires had yet to be incorporated into the design. The assembly was difficult and not very repeatable; having to use a separate spacer to define the inter-electrode spacing led to issues during assembly with uniformity and device survival. The design was fundamentally flawed; having a planar emitter leads to surface breakdown along the dielectric posts and makes it difficult to attach the power tethers without harming performance. All of these problems would have to be solved before it was worth pushing towards controlled flight of an ionocraft.

4.2 Improved Assembly, Lifetime, and Payload Capacity

This work was published and presented at the 2018 Transducers Research Foundation Microsystems Workshop at Hilton Head (HiltonHead).

Motivation and Brief Description

While the initial results of the quad-thruster ionocraft were promising, there was significant room for improvement in terms of thrust density, operating voltage, device lifetime, and assembly repeatability. In this work, a 13.6mg, 1.8cm by 1.8cm ionocraft is shown to take off while carrying a 40mg Flex PCB with 9-axis IMU and associated passives while tethered to a power supply. A new emitter electrode design decreased corona onset voltage by over 30% and takeoff voltage by over 20% from previous efforts. Ease of assembly is an important metric for a future microrobotic platform, as it may be a key driver of scalability and unit

cost. The refined assembly process shown in this work has decreased time per robot to about half an hour, with nearly a 100% success rate, in a process that could easily be automated thanks to its mechanical simplicity. Additionally, a key actuator performance degradation issue, inherent to the energetic plasma of the corona discharge effect, is remedied in a simple and scalable manner (i.e. through a single thin film deposition).

Methods

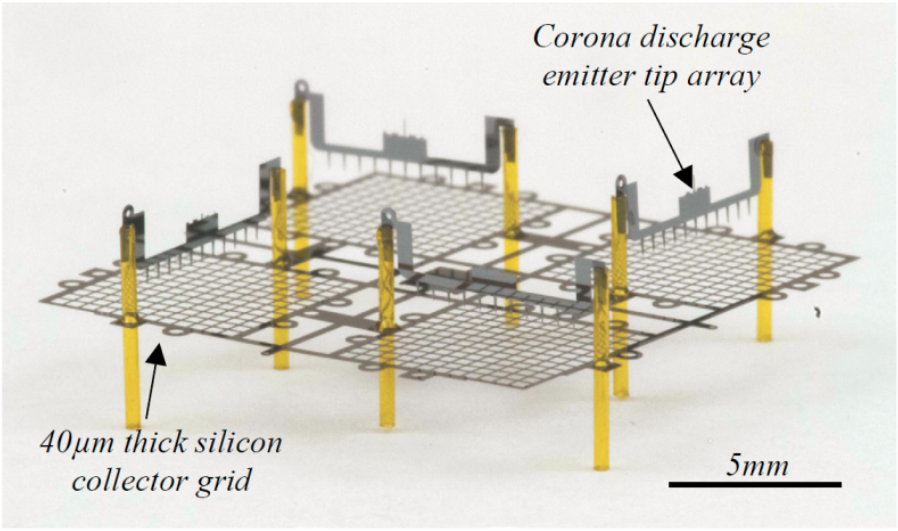

Figure 4.7: Photograph of the assembled ionocraft. With four individual addressable thrusters, it is about 1.8cm by 1.8cm and masses 13.6mg. It is comprised of 13 individual components connected by a combination of mechanical slots and UV-curable epoxy. The design includes various tabs for handling and connection to power tethers.

Silicon electrodes with lithographically defined asperities to decrease corona onset voltage are fabricated in plane, fully released, and then rotated and assembled out of plane. The fabrication process previously reported at MARSS 2017 [18] is adapted to a single mask SOI process in this work to increase device yield and decrease number of fabrication steps. An improved assembly method (Fig. 4.8) differs from prior work in that it: allows the electrodes to be designed for mechanical robustness (to survive assembly); separates the power tether connection point from the collector grid by a lithographically defined amount to prevent surface breakdown along the dielectric post; and allows the inter-electrode gap to be controlled semi-lithographically.

The new emitter electrode design for out of plane rotation requires inserting silicon "shanks" into the silica dielectric standoff tubes. Typically, capillary tubes are cut by hand using a small ceramic tool; while macroscopically these cuts are smooth, they actually often leave jagged or ragged edges. Inserting wires into a poorly cut capillary tube could either

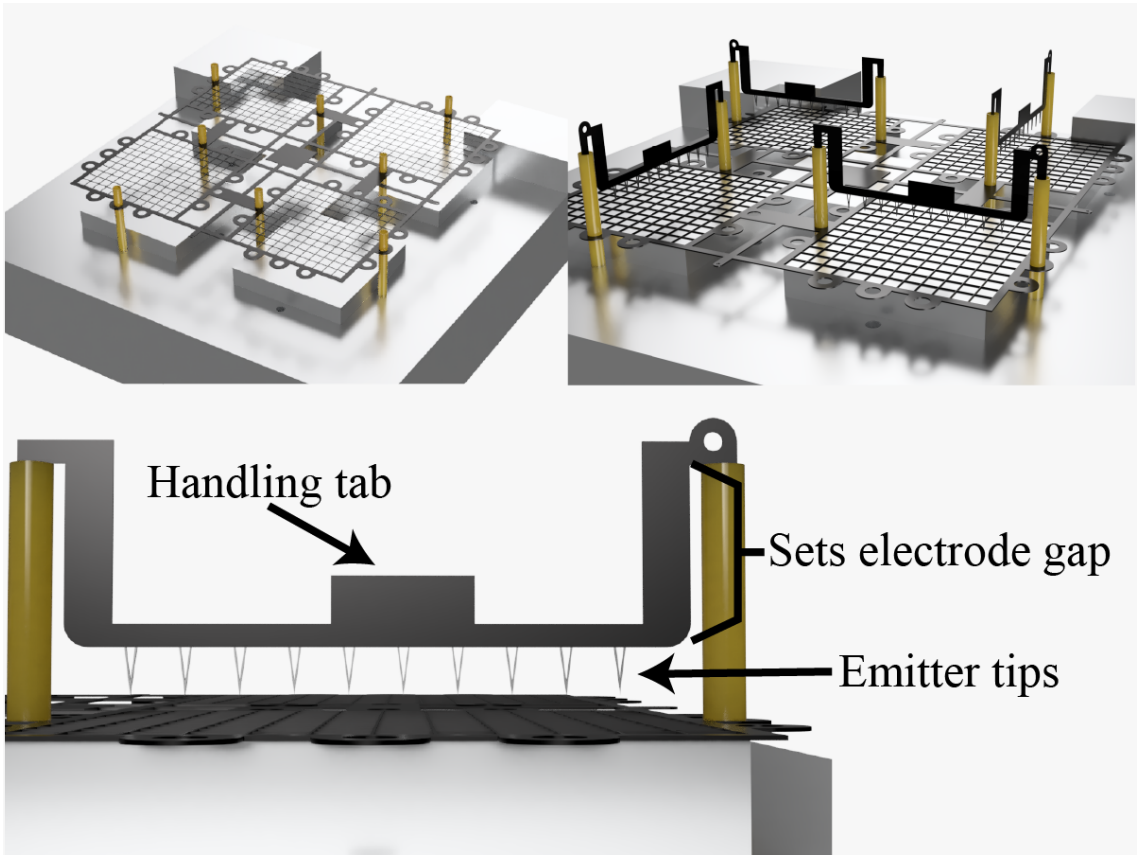

Figure 4.8: 3D model renders of the assembly process. Pre-cut silica tubes are inserted into slots in a CNC-milled aluminum jig. The ionocraft frame is slid down the guiding posts. The emitter wires are rotated out of plane and tapered guides are inserted into the silica tubes. The inter-electrode distance is now determined by a combination of lithography, slot depth, and tube length.

be impossible or result in potential misalignment/non-uniformity of the emitter. A new, surprisingly rare tool was procured to get around this issue. It consists of a mechanical clamping mechanism with a manual set-screw and a diamond cutter mounted on a rotary wheel. Capillary tubes are inserted, the diamond cutter is brought into contact with the surface, and the entire cutter is manually rotated. This results in highly uniform, repeatable cuts. This tool (see Figure 4.9) is also the secret as to why the emitters are shaped with their particular "elbow," and how emitter-collector gap is able to be set semi-lithographically. By setting the tool on a level surface and sliding the capillary tube through until it makes contact prior to clamping and cutting, tubes of 5.67 $\pm$ 0.02 mm are made (n=10, measured by digital micrometer). Various attempts to modify the setup in order to cut shorter tubes have negatively affected uniformity and repeatability.

A Flex PCB board (Fig. 4.10) has been fabricated containing a commercial 9-axis IMU,

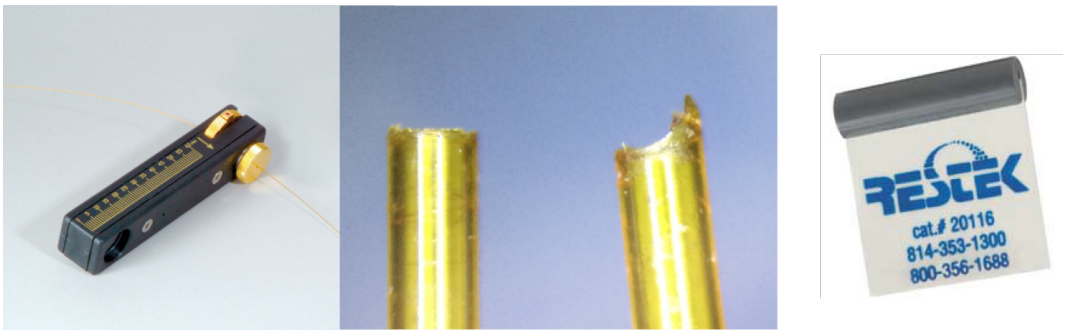

Figure 4.9: *Left:* The rotary blade capillary tube cutter allows for more uniform, repeatable cuts. *Center:* A new tube is shown on the left while a typical edge on one of the old is shown on the right. This was key in the transition towards enabling perpendicular (i.e., emitters pointed towards the collector grids) electrode design. *Right:* The standard ceramic cutting tool used for capillary tubes.

the InvenSense MPU-9250, as well as three associated passives and bonding pads. The board's 5mm by 5.5mm footprint allows it to be placed in a designated central region of the robot airframe without interfering with the surrounding thrusters. The total board mass of about 40mg (including all components) is within the expected payload capacity reported in prior work.

To measure output force, the device under test is mounted on a threaded nylon post fixed directly to a Phidgets 100g Micro load cell. For full quad-thruster ionocrafts there is a dedicated region in the center of the airframe for mounting; single thrusters are mounted using one of the unused silica tube slots along the grid frame. Multiple instruments are controlled via GPIB for synchronized force-current-voltage sweeps.

Results and Discussion

The presented data is from a range of fabricated devices; unless otherwise noted, collected data is from the first trial using each device to reduce the effect of lifetime performance degradation (device lifetime discussed in Section 4.2). There was significant noise in the strain sensor used for force measurement for the values used in this work; presented data is first passed through a low pass filter in the Phidgets data hub and then averaged over 3 seconds of collection (11 data points) for each measurement.

Electrode Geometry

In a widely-used empirically derived equation for corona onset voltage formulated by Peek [70] (discussed further in Section 2.1), for point-to-plane geometries it is found that $V_0 \propto ln(d)$. Decreasing the electrode gap from 500μm to 250μm (Fig. 4.11) was shown to decrease the onset voltage, as found by the 0-intercept of the curve fit to Eq.2, by approximately 400V,

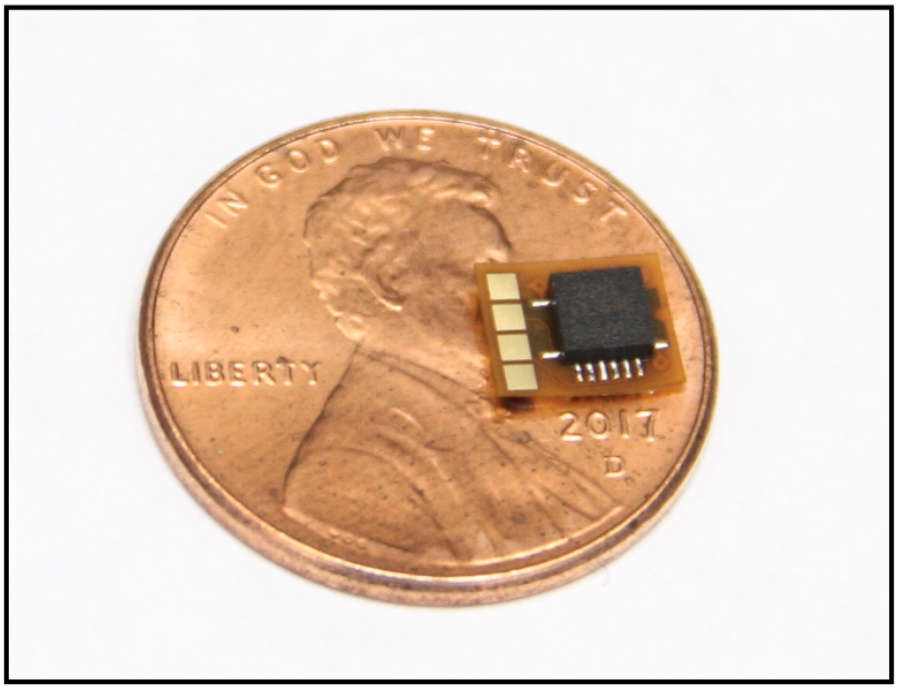

Figure 4.10: Flex PCB IMU board on a U.S. penny. The board is about 5mm by 5.5mm and masses 40mg including all components. It contains an InvenSense MPU-9250 9-axis IMU and three associated passives.

a larger change than predicted by this trend. Although related work already shows deviation from Peek's equations in sub-millimeter corona discharges, this greater deviation at even smaller gaps bears further investigation. The factor relating ion current after corona ignition to the input voltage, C, was shown to increase by about 230%; because current must double to produce the same output force at half the drift distance, this would ideally correspond to a smaller required operating voltage swing for the same force production range.

The 250μm gap device has an extracted β via linear fit of current-force data of 0.33, 44% lower than the extracted value of 0.59 for the 500μm gap, 5-degree device. Although the absolute value of this factor may be incorrect due to likely variation in ion mobility from the assumed $2cm^2/Vs$, the trend is expected from prior work and likely largely due to the effect of aerodynamic drag on the smaller spacing of the 250μm collector grid. Further, device failure (i.e. arcing) occurred before the same maximum force could be produced by the smaller electrode gap, indicating that emitter tip radius, r, should be decreased in an effort to increase the d/r ratio critical for corona discharge.

The onset voltage was not found to change significantly between 5-degree and 10-degree drawn emitter tip angle wires. This could indicate some limit in dimensional scaling following DRIE and current lithography methods, as asperity drawn angle was shown to have a strong effect on onset voltage in prior work [4].

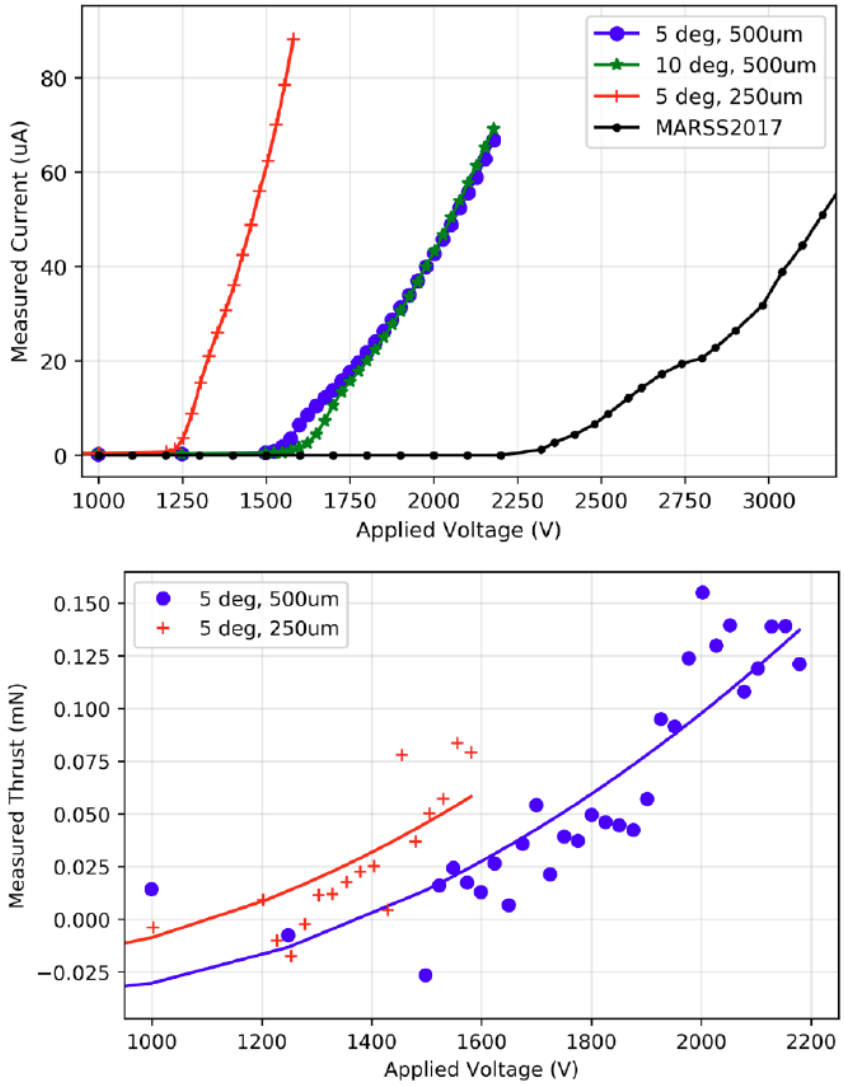

Figure 4.11: Current and force versus voltage curves for thrusters with different electrode gaps or different drawn emitter tip angles. The current-voltage data from MARSS2017 [2] is a 20μm by 40μm cross section silicon "wire" with no lithographically defined asperities at an electrode gap of 1mm. The 250μm electrode gap device uses a collector grid with 250μm spacing. The plotted lines in the force-voltage plot are 2-degree polynomial fit lines.

Thrust Density

Adding more emitter wires per collector grid should have the effect of increasing both C and thrust-to-weight ratio at the cost of additional assembly time. Experiments show that corona discharge current scales approximately linearly with number of emitter wires (Fig. 4.13) at a wire spacing of 3mm for the 2-wire case and 1.5mm for the 3-wire case. Going from one emitter wire per collector grid to three increases C by about 250%, while β decreases from 0.59 to 0.53. The fact that current did not scale linearly may be attributable to assembly or device degradation nonuniformity, and the decrease in beta is within the measurement error for the strain sensor used in this work. As discussed in Section 2.3, we would actually expect β to improve with more emitter wires (given correct neighbor spacing) due to space charge region interactions.

The mass of an additional emitter wire and two silica posts is only 1.5mg while the maximum thrust is increased by approximately 100μN (10mg) per set, showing a large potential boost to thrust-to-weight ratio. Prior work in FEA simulation indicates that the space charge region developed from a single emitter wire's corona discharge spans a horizontal radius approximately equal to the electrode gap distances. This indicates that wire neighbor spacing can be decreased from 1.5mm to 1mm and the maximum number of emitter wires per collector grid could double to 6 without significant neighbor interactions; although this would certainly continue to provide an aerial thrust density and thrust-to-weight ratio benefit, assembly complexity would be prohibitive with the current design.

Device Lifetime

Performance of a corona discharge based EHD thruster can be expected to degrade over time, largely as a result of interactions of the bipolar plasma region with the emitter electrode. Initial experiments saw rapid loss of discharge current over time with a constant applied voltage (Fig. 4.14). Scanning electron micrographs showed large amount of physical damage to the emitter wires, localized to the tips themselves, with a damage radius of around 60μm. With the hypothesis that this damage is a result of energetic ion ablation in the bipolar plasma (a plasma radius of 50μm is often assumed in literature), the tips were sputtered with a 100nm titanium nitride layer, turned over, and sputtered with another 100nm layer (Fig. 4.14, bottom). Subsequent testing saw no degradation of performance in the same time period. It is expected that the new failure mode will be through oxidation of the tips, enhanced by the energetic oxygen plasma.

Takeoff with Sensor Payload

Current flying microrobots are typically payload constrained; either they fail to lift the weight of their own actuators and airframe, or must seek to develop novel sensing schemes and platforms to optimize for mass. The relatively high thrust-to-weight ratio of the ionocraft means that it may be possible to use standard commercial sensors, simplifying development and

implementation. To prove the feasibility of future controlled flight using a commercial sensing package we developed a 40mg FlexPCB with 9-axis IMU as discussed above, attached it to a designated central region in the ionocraft airframe with UV-curable epoxy, and demonstrated take off (Fig. 4.12). This single-emitter design had an unladen takeoff voltage of about 2000V (2100V with IMU); this number should decrease by using multiple emitter wires per thruster, but with the assembly jig used in this work it was difficult to reliably assembly such a version.

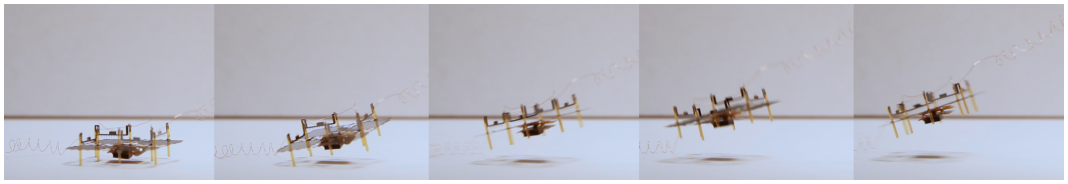

Figure 4.12: An ionocraft with assembled 40mg Flex PCB IMU board attached to the airframe center pad. At about 2100V, the ionocraft is able to take off from the table; the power and ground wires prevent the ionocraft from going any higher. There is only one high voltage line attached here, with connections between the emitter wires done on the ionocraft itself. The IMU board is not wired or active during takeoff in this particular work (see Section 4.3).

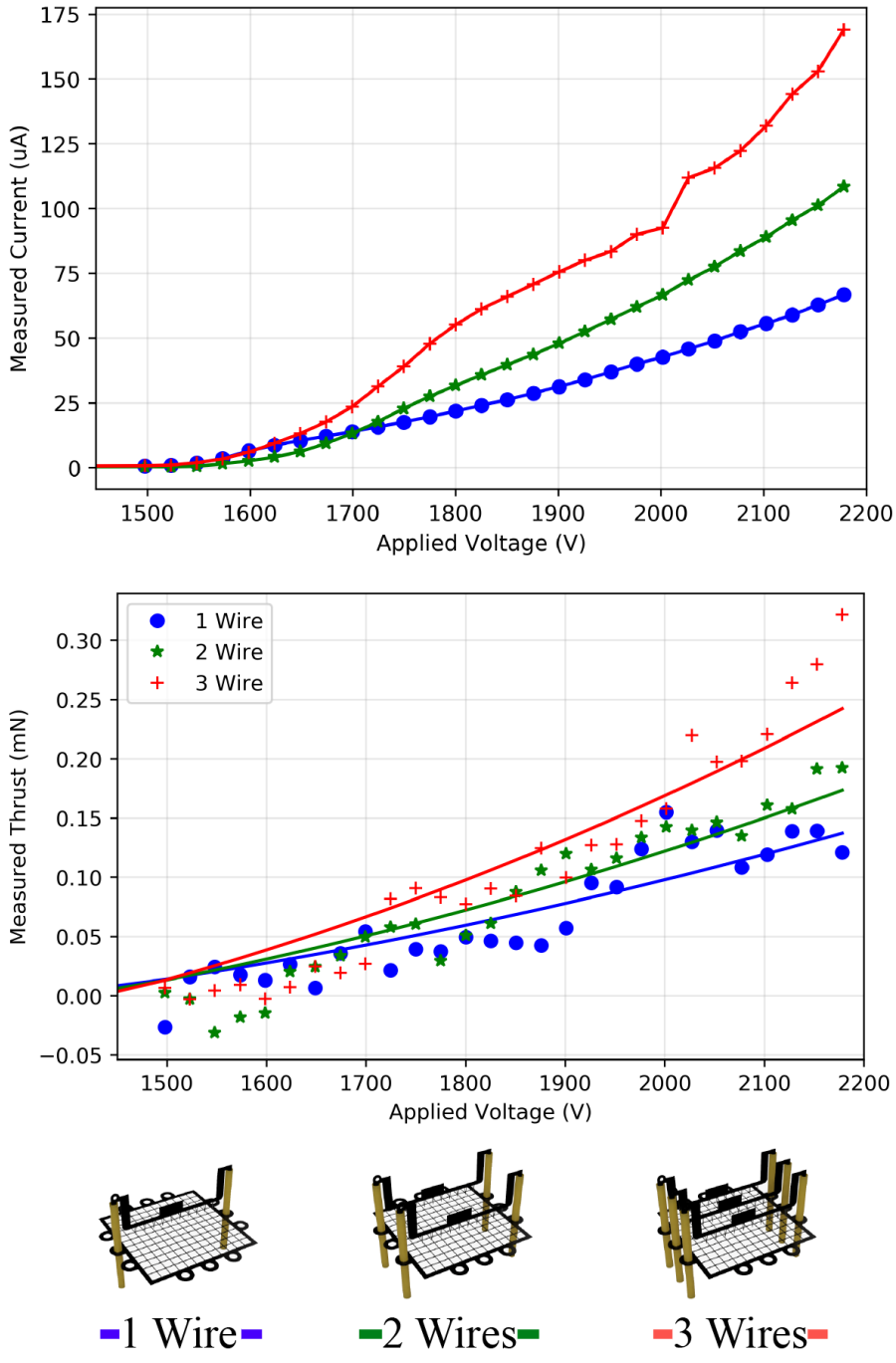

Figure 4.13: Current-voltage and force-voltage curves produced by varying the number of emitter wires in a thruster. Tests are for 5-degree emitter tips, an electrode gap of 500μm, and a collector grid spacing of 500μm. The plotted lines in the force-voltage plot are 2-degree polynomial fit lines.

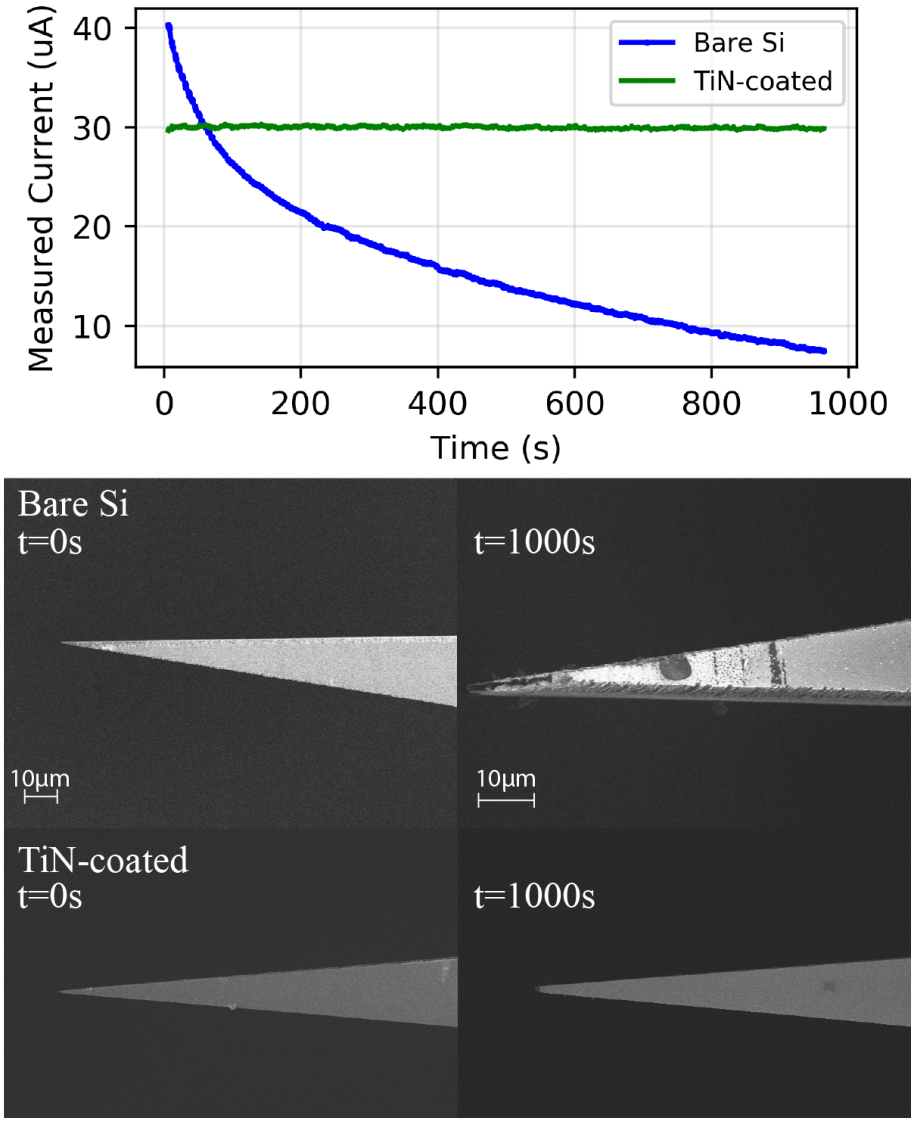

Figure 4.14: Device lifetime quantified by measured ion current versus time at a constant operating voltage. Bare silicon emitter wires saw immediate performance degradation during testing, while wires coated by about 100nm of sputtered TiN had stable performance up to the measured 1000s of operation. Devices are 10-degree tips at a 500μm gap with 1800V applied.

Contributions and Conclusions

Succinctly, the contributions of this work were:

- Demonstration of improved thrust density of EHD actuators via a simple increase in number of emitter wires.
- Significantly decreased operating voltage of a centimeter-scale ionocraft from prior work.
- An improved assembly method for quad-thruster ionocraft that significantly improved repeatability and decreased time per experiment.
- An identification of a limiting factor for device lifetime and a simple, scalable solution.
- First demonstrated takeoff of a centimeter-scale ionocraft while carrying a useful sensor payload.

Although we have validated the use of multiple emitter wires as a way to increase device performance, with the current design each new emitter wire requires both its own pair of silica posts (with associated epoxy) and electrical connection to its neighbors, decreasing benefit to thrust-to-weight ratio. Future work will explore new methods, for example designing mechanical interlocks into the components themselves, to overcome these challenges. As electrode gap continues to decrease in an effort to decrease operating voltage, the effect of decreasing electrode d/r ratio on minimum drift field strength, and therefore efficiency, becomes more pronounced. The devices in this work have efficiencies that range from 2 mN/W to 1 mN/W over their operating range, unacceptably low for a truly autonomous flying robot with any useful mission time; see Section 1.1 for comparisons with existing technology. It may be necessary to increase emitter tip sharpness beyond what is possible with standard lithographic techniques, for example with thermal oxide sharpening, in order to operate ionocraft in higher efficiency regimes by trading off output force.

4.3 Towards Controlled Flight of the Ionocraft

This work was published in the journal Robotics and Automation: Letters [17]. It was made as a dual contribution to the 2018 IEEE International Conference on Intelligent Robots and Systems (IROS), and was presented there.

Motivation and Brief Description

With the validation of the quad-thruster configuration and the various improvements to thrust density, assembly, and lifetime, the next step in creating an autonomous ionocraft was to demonstrate the possibility of closed-loop control. The robot and assembly jig were

both redesigned to incorporate some of the improvements. A high voltage control circuit had to be prototyped to attempt to measure the dynamic response to a time varying signal instead of the standard steady state value previously measured.

For the first time, attitude and acceleration data is continuously collected from takeoff and sustained flight of a 2cm x 2cm, 30mg "ionocraft" carrying a 37mg 9-axis commercial IMU on FlexPCB payload, with external tethers for power and data transfer. The ionocraft's steady state thrust versus voltage profile, dynamic response to a time-varying signal around a high voltage DC bias point, and aerodynamic drag at incident angles around 90 degrees were measured. These experimental measurements, as well as measured IMU sensor noise, were inserted into a Matlab Simulink simulation environment. Simulation shows controlled hovering and planned flight in arbitrary straight trajectories in the X-Y plane.

Methods

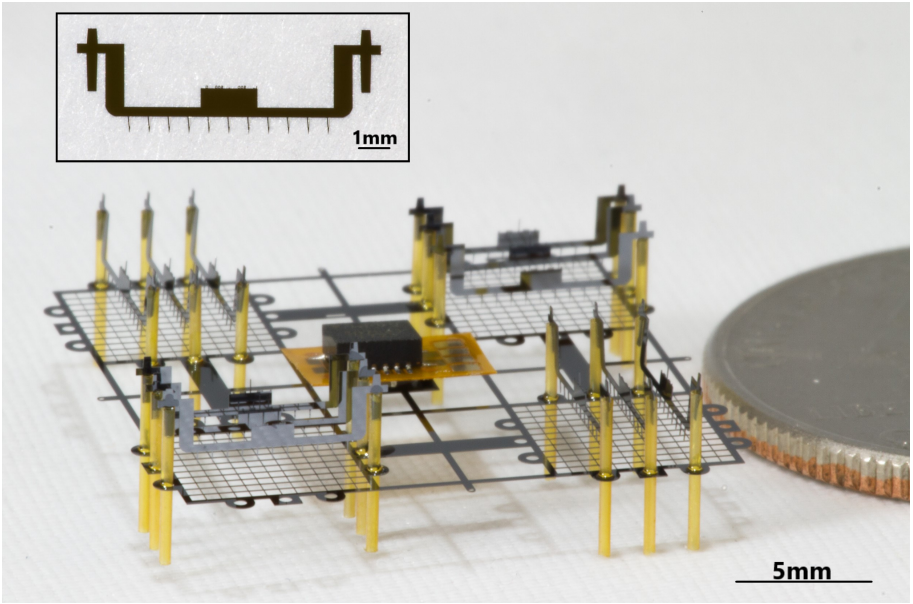

Figure 4.15: An assembled ionocraft next to a United States quarter. The ionocraft itself is approximately 2cm by 2cm and masses 30mg. Also shown is the 37mg FlexPCB board with 9-axis IMU and associated passives attached to the center of the airframe. The ionocraft is built from 41 discrete components, each connected by a combination of mechanical slots and UV-curable epoxy. Inset: A single emitter electrode. The $500\mu m$ long, 5deg tip angle lithographically defined asperities are aligned with the grid and used to reduce operating voltage.

The robots (Figure 4.15) are made using active electrodes fabricated in standard MEMS wafer-scale silicon processes as well as commercially available silica tubing. A silicon-on-insulator wafer with 40μm device thickness forms the substrate for a single-mask deep

reactive ion etch and subsequent vapor-phase hydroflouric acid release etch. Thin tether structures are broken manually to yield fully released, 40μm thick emitter and collector electrodes that can be removed from the wafer surface for assembly. Fused-silica capillary columns, typically used for gas chromatography, are the dielectric standoffs between the electrodes.

Assembly of the robots (Fig. 4.16) involves standard surface-mount technology (SMT) practices performed under a dissection microscope. Electrodes are moved and placed by a combination of a small diameter vacuum wand and tungsten micromanipulator probes. Mechanical connections and alignments are handled by a combination of geometric tolerances and UV-curable epoxy applied via a micromanipulator probe. Electrical connections are formed by silver epoxy applied via a pneumatic fluid dispensing system and cured on a hot plate. A CNC-milled aluminum fixture is used to keep the device in place and provide alignment aid for various components.

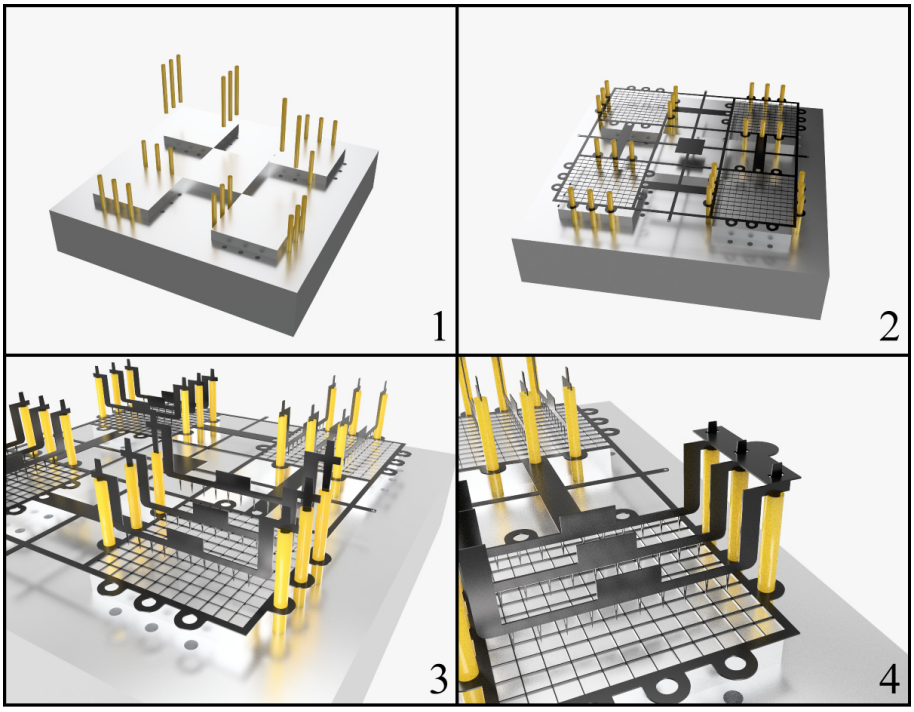

Figure 4.16: 3D model renders of the assembly process. (1) Pre-cut silica tubes are inserted into slots in a CNC-milled aluminum jig. (2) The ionocraft airframe is slid down the guiding posts. (3) The emitter wires are rotated out of plane and tapered guides are inserted into the silica tubes. The distance between the emitter wires and collector grid is now determined by a combination of lithography, the length of the silica tubes, and the depth of the guide slots milled into the jig. (4) Silicon "jumpers" are lowered onto guide posts on the emitter wires. These both help with alignment between adjacent emitter wires and serve as electrical connection points after application of silver epoxy.

A Flex PCB board was designed to contain a commercial 9-axis IMU, the InvenSense MPU-9250, as well as three associated passives and bonding pads. The board's 6mm by 6.5mm footprint allows it to be fixed in place via UV-curable epoxy in a designated central region of the robot airframe without interfering with the surrounding thrusters.

Results and Discussion

Actuator Response

To measure output force, the ionocraft is mounted on an acrylic post fixed directly to a Phidgets 100g Micro load cell. Multiple instruments are controlled via GPIB for synchronized force-current-voltage sweeps.

The canonical expression for electrohydrodynamic force based on an ideal 1D model together with a constant factor, β, is given in (4.1) and discussed in Section 2.2, where d is the ion drift distance and μ is the ion mobility in air (approximately 2e-4 m^2/Vs for N_2^+ in dry air). The β factor accounts for losses in the system that arise as a combination of indirect ion field paths (loss of vertical output force to horizontal momentum transfer), ratio of plasma sheath size to drift gap, and aerodynamic drag on the collector grid,

$$F = \beta \frac{Id}{\mu} \tag{4.1}$$

Sets of emitter wires with both 5 and 10 degree nominal tip angles (tips visible in Fig. 4.15 inset) were fabricated. Decreasing the lithographically defined tip angle from 10 to 5 degrees was shown to decrease corona discharge onset voltage by about 100V without a significant affect on the IV relationship following plasma ignition (Fig. 4.17). Prior work has measured a loss factor of about 50% ($\beta = 0.5$) using similar microfabricated silicon electrodes [20]. Direct measurement of output force as a function of applied voltage and ion current (Fig. 4.17) in this work yield a β of approximately 0.8 for the 5 degree emitter tips and 0.7 for the 10 degree emitter tips.

A 1mN total output force from four 6mm x 6mm collector grids corresponds to a thrust density of about $7N/m^2$, a similar value to prior work despite an increased emitter wire density. It is possible that the emitter wire spacing of approximately 1.5mm is too high and should be brought to a value between 40% and 80% of the electrode gap distance (500μm) for an optimal thrust density increase, as shown in work on larger electrode gap EHD systems [30].

A high voltage amplifier circuit (Fig. 4.18) was created for testing the dynamic response of the ion thrusters. First, a positive DC voltage above the corona discharge initiation is applied to the emitter electrode with the collector electrode held at ground. Next, a $2V_{pp}$ sine wave produced by a function generator at the input of the amplifier is transformed by the amplifier gain of 100 into a high voltage ($200V_{pp}$) signal.

The ionocraft was shown to successfully track sine wave inputs with frequency up to 10Hz (Fig. 4.19). Significant measurement noise, with magnitude higher than the forces

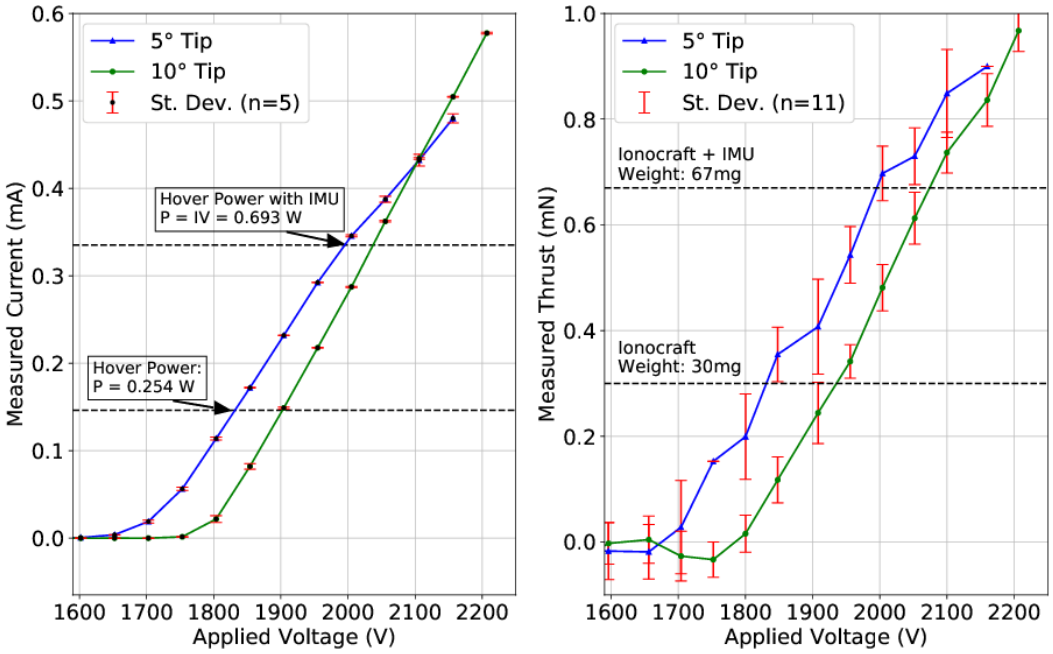

Figure 4.17: Plots showing measured current (left) and measured output force (right) of the ionocraft as a function of its input voltage. The upper horizontal line shows the current (left) and force (right) required for hovering with the IMU onboard. The lower line shows the current and force needed for takeoff without the IMU. While collecting this data, all four of the thrusters were electrically connected. Tip angle refers to the nominal apex angle of the lithographic asperities on the emitter wires.

attempted to be resolved, precluded experimentation without the load cell's custom-built data capture accessory (PhidgetBridge). The sampling frequency limitations of this accessory made experiments at frequencies above 10Hz impossible. Future work will develop a more stable testing platform for >100Hz dynamic response characterization that can resolve forces on the order of $10\mu N$.

Tethered Flight with Onboard Sensor

Takeoff while streaming attitude and acceleration data from the on-board 9-axis IMU was demonstrated (Fig. 4.20). Liftoff occurred at approximately 2000V — over 20% lower than prior work which did not contain an onboard sensor package [18]. There are a total of seven external wires: two high voltage lines to the emitter wires (the two other thrusters are connected internally); power, ground, and two data wires to the IMU FlexPCB; and a separate ground connection to the airframe. A common issue in the field of microrobotics is that the spring force of the external tethers required for power and control tends to overpower the system due to the robot's relatively low mass and output force, preventing

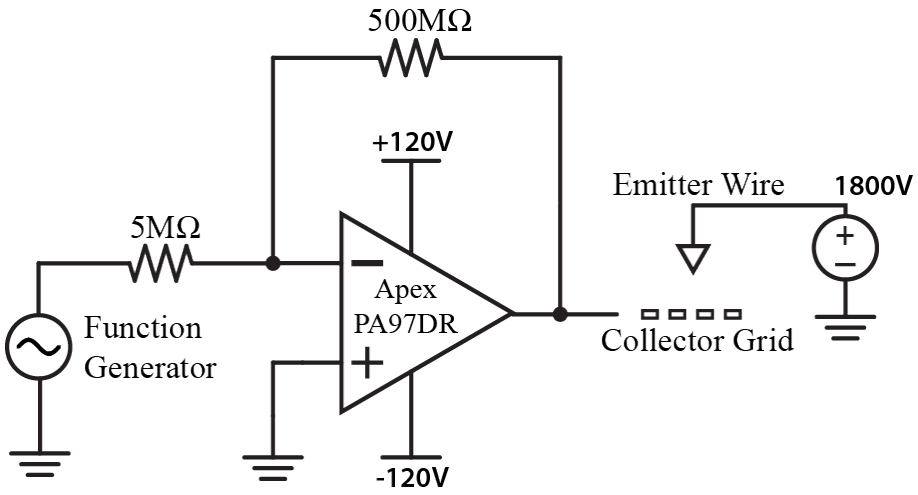

Figure 4.18: Circuit schematic of the actuator dynamic response test setup. A high voltage op-amp is used to modulate the control inputs around a DC bias point by raising and lowering the voltage of the collector grid.

movement. The external wires in this case confer a degree of stability during open-loop flight that prevents an immediate failure like twisting in its own tethers, but the robot is still both unstable (high body angle oscillations) and able to return to landing on the ground when power is no longer applied. Although future work will strive to decrease the number of external tethers and therefore their contribution to body dynamics, the first instances of controlled flight will certainly be under tethered power; this demonstration of takeoff despite the external tether forces is encouraging.

The open-loop flight is synchronized with the streaming sensor readings during post-processing. Takeoff and landing cycles were repeated up to five times with a single robot without failure, although the IMU had to be restarted after a landing where the ionocraft had flipped completely over before touching down.

Aerodynamic Drag

A miniature low-speed wind tunnel, designed using ANSYS FEA software and constructed from a combination of laser cut and 3D printed parts, is used to characterize aerodynamic drag on the ionocraft. The full tunnel is about 1.5 meters long, with a 10cm x 10cm x 20cm test chamber. A manually controlled variable-speed fan is calibrated using a TSI AVM430 hot wire anemometer inserted through an inlet in the test chamber. The ionocraft is mounted on an adjustable acrylic sting using epoxy applied to the center pad of the airframe. The sting attaches directly to a Phidgets 100g Micro load cell.

Experimental measurements of drag force F_D versus wind speed v and angle of incidence θ are fit to a hyperplane, as shown in Fig. 4.21. The region of measurements collected are $v \in [0, 10)$ (m/s) and $\phi = 1 - \theta \in [0, \frac{\pi}{6})$ radians. We model the drag at this wind speed as

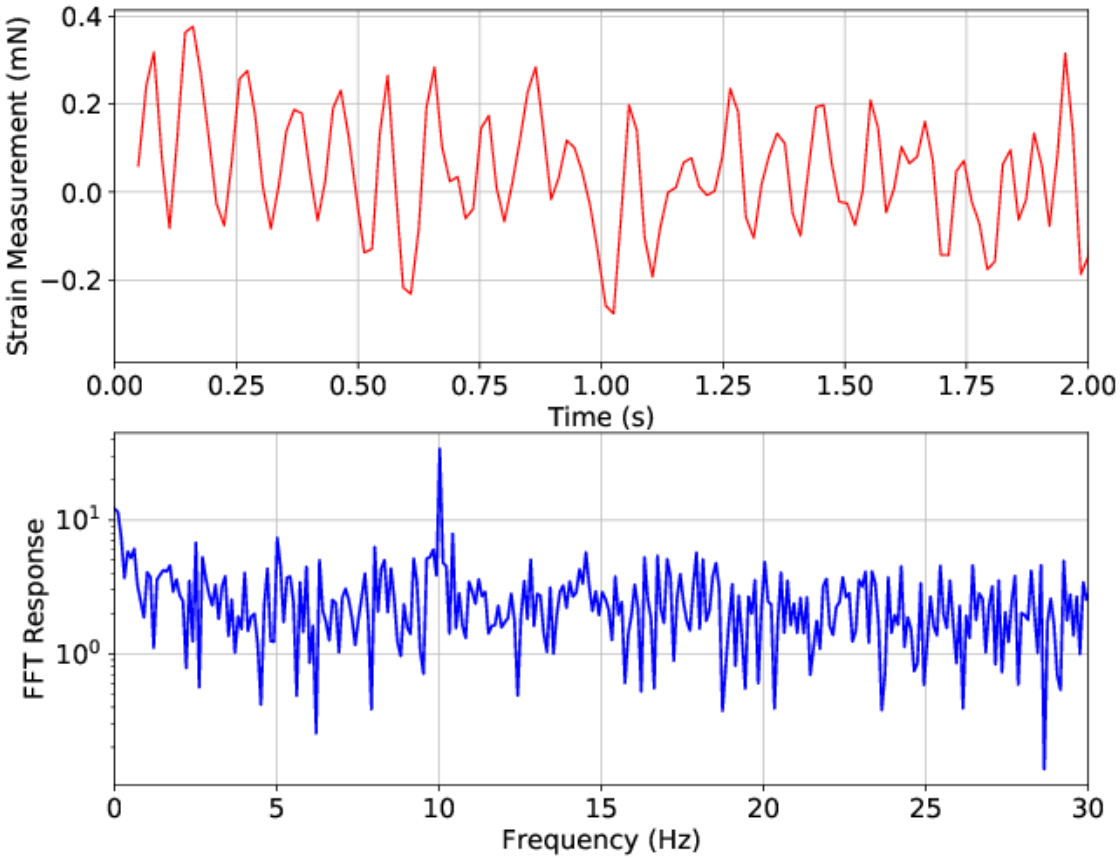

Figure 4.19: The output force from an ionocraft with a 1800V DC bias applied to the emitter wires and a 200V peak-to-peak, 10Hz sine wave applied to the collector grids. The data is collected with a sampling period of 16 ms. Top: Measured output force with DC bias force (approximately 0.22mN) and weight of the ionocraft subtracted, then filtered by a digital 20Hz cutoff low pass filter. Bottom: A Fourier transform of the zero centered, unfiltered strain data shows the distinct 10Hz peak.

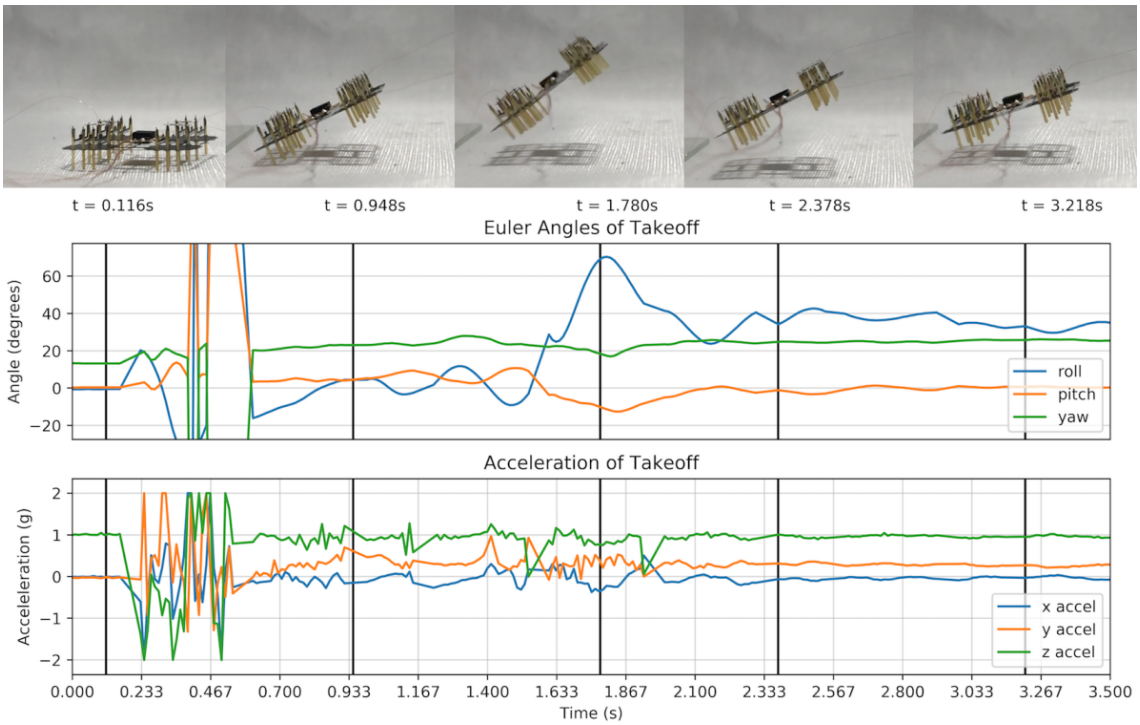

Figure 4.20: Open-loop, uncontrolled takeoff of the ionocraft while carrying an InvenSense MPU-9250, a state of the art 9-axis IMU. The IMU is reporting accelerations and Euler angles at roughly 100Hz, the latter of which is calculated using InvenSense's proprietary MotionFusion algorithm on-board the IMU. Each image of the ionocraft was taken at the time corresponding to the black line below it. Erratic transient response from the IMU at the time of high voltage application indicates that further electromagnetic shielding may be necessary.

being of the form

$$F_D(v) = av^2 + bv \quad [mN] \tag{4.2}$$

where the constants a and b are parameters of ϕ, resulting in the drag function $F_D(v, \phi)$. Fitting the a and b to a first order polynomial to match the common approximations $\sin(\phi) = \phi$, $\cos(\phi) = 1 - \phi$ for $0 \leq \phi \ll 1$, we get a parametric function of the form:

$$F_D(v, \phi) = (a_1\phi + a_2)v^2 + (b_1\phi + b_2)v \quad [mN] \tag{4.3}$$

Fitting with ordinary least squares returns the following parameters:

$$\begin{array}{rclrcl} a_1 & = & -.0558 & b_1 & = & -.0201 \\ a_2 & = & .1305 & b_2 & = & .6275 \end{array}$$

The drag fit yields a maximum vertical (90 degree angle of incidence) airspeed of 1.26 m/s; this corresponds to a drag force of 1mN, which is equal to the maximum thrust the

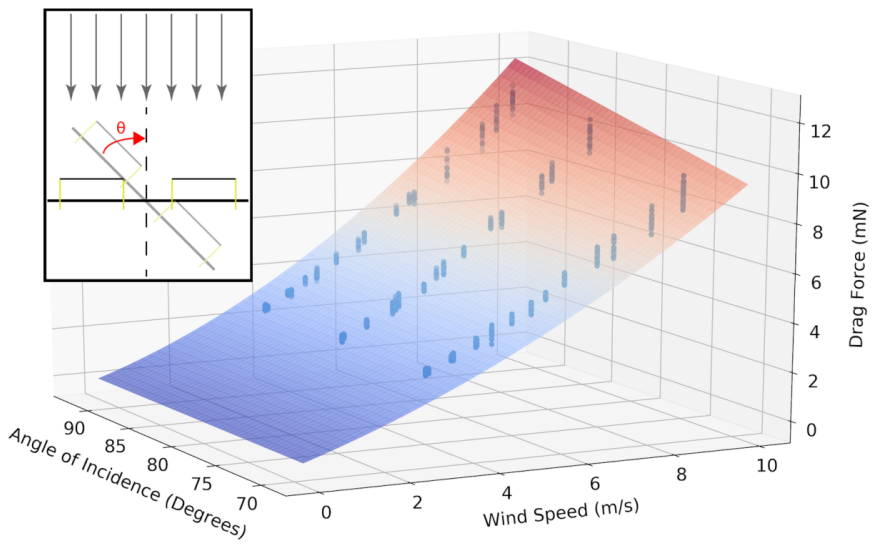

Figure 4.21: Plot of the wind tunnel drag data shown with a fitted hyperplane using (4.3). The upper left diagram shows the definition of angle of incidence.

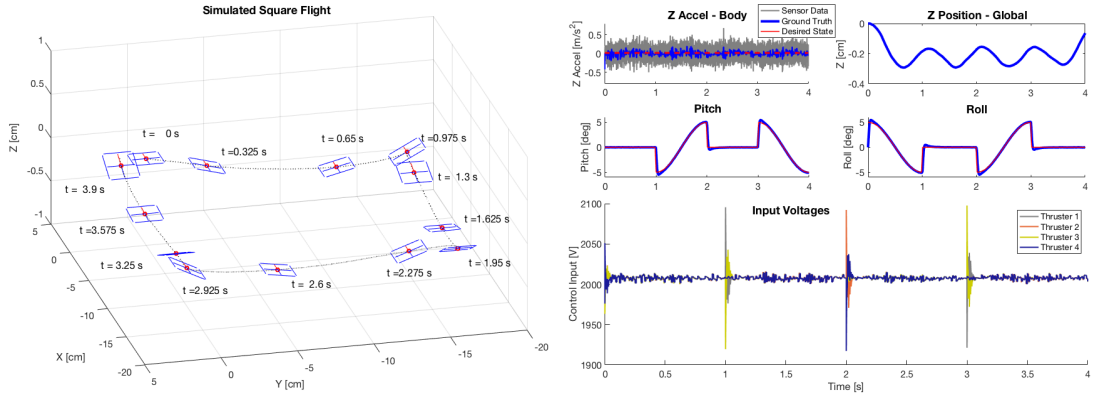

Figure 4.22: Left: A simulated flight of the ionocraft over a 4 second flight about a square. The square is navigated by supplying sinusoidal profiles as desired states to pitch and roll controllers independently, and the trajectory of its center of mass is shown in the dotted black line. Right: Control inputs and state variables for the simulated flight. Note that global Z position is only for evaulating simulation performance, and is not a variable being controlled. The pitch and roll measurements have noise, but the magnitudes are substantially lower than the controlled movement.

ionocraft is capable of producing. The measured values used to create the hyperplane are above 3 m/s due to the difficulty of reliably generating low speed laminar flow in the wind tunnel.

Dynamics Model

The dynamics of a quadcopter are well studied and understood [2, 54]. A quadcopter's four individually controllable thrusters each generate a force F_i resulting in a body fixed-frame z-axis thrust, T, and body fixed-frame torques τ_x, τ_y, and τ_z, as shown in (4.4). The constant c is a coupling factor between the motor forces and the τ_z. The parameters l_x and l_y are defined as the distance from the thruster's center to the body fixed-frame's center of mass in the x and y directions, respectively. We use a north-west-up axis orientation.

Because a quadcopter's four thrusters are propeller based, and therefore generate angular momentum, the coupling factor c is non-zero. It can then be seen that the matrix in (4.4) is full rank, and therefore control of T_z, τ_z, τ_y, and τ_x are decoupled.

$$\begin{bmatrix} T_z \\ \tau_z \\ \tau_y \\ \tau_x \end{bmatrix} = \begin{bmatrix} 1 & 1 & 1 & 1 \\ -c & c & -c & c \\ -l_x & -l_x & l_x & l_x \\ -l_y & l_y & l_y & -l_y \end{bmatrix} \begin{bmatrix} F_1 \\ F_2 \\ F_3 \\ F_4 \end{bmatrix} \tag{4.4}$$

The ionocraft model is the same as the quadcopter model, with one important exception — the ionocraft uses ion thrusters instead of propeller based thrusters (i.e., the ionocraft thrusters do not generate angular momentum) and therefore the coupling constant c is equal to 0. Accordingly, the matrix in (4.4) is *not* full rank and control authority of τ_z (i.e. yaw control) is lost.

The ionocraft thrust forces, assumed to be point forces at the corners of the robot, along with drag, are the only forces applied in the model; the tether wires are not incorporated in the dynamics. The assumption of thrust being a point force holds when the force distribution over the collector grid is uniform; in reality, the EHD force is not axisymmetric but instead expected to decrease with distance from the emitter wires (i.e., in the x direction if the wires are assumed to lie along the y axis) as some function of the device electrostatic solution.

Controller Design

Hovering and basic open loop trajectories only require data streamed from the 9-axis IMU. To hover, the controller regulates $\ddot{z}$, pitch, and roll to zero. The equilibrium input for each individual thruster is $F_{eq} = \frac{mg}{4}$. The outputs $u_{\ddot{z}}$, u_θ, and u_ϕ of the PID controllers (shown in Fig. 4.23) are used to drive the system to desired vertical acceleration, desired pitch, and

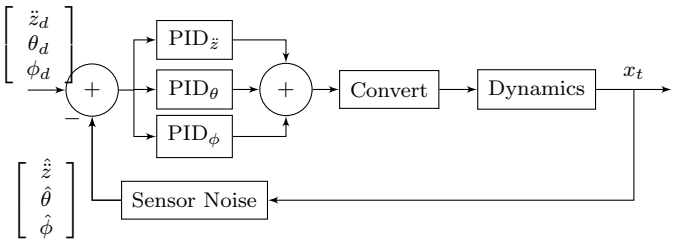

Figure 4.23: Overall structure of the control scheme. The errors between the estimates of vertical acceleration, pitch, and roll ($\hat{\ddot{z}}$, $\hat{\theta}$, and $\hat{\phi}$, respectively) and the desired states $\ddot{z}_d$, θ_d, and ϕ_d are fed through three PID controllers. The outputs of the controllers are then converted into a vector input as shown in (4.5). Not shown is a saturation block that prevents the thrusters from trying to apply more force than the maximum value before breakdown (approximately 0.25 mN per thruster).

desired roll, respectively, where $\vec{F}$ is the vectorized input containing all four thruster forces.

$$\vec{F} = \begin{bmatrix} F_{eq} \\ F_{eq} \\ F_{eq} \\ F_{eq} \end{bmatrix} + \begin{bmatrix} 1 \\ 1 \\ 1 \\ 1 \end{bmatrix} u_{\ddot{z}} + \begin{bmatrix} -1 \\ -1 \\ 1 \\ 1 \end{bmatrix} u_\theta + \begin{bmatrix} 1 \\ -1 \\ -1 \\ 1 \end{bmatrix} u_\phi \tag{4.5}$$

Each thruster has a maximum force it can provide (approximately 0.25mN); this saturation makes each thruster nominally non-linear. The PID controllers are tuned around equilibrium so that the controlled forces stay well away from saturation within tested operation.

Yaw actuation can be achieved by quick, repeated sequences of "pitch and then roll." Simulation demonstrates this approach achieving a yaw rate of up to ±10 deg/s while still maintaining stable hover. This method comes at the cost of up to 10 cm/s X-Y drift because of the lack of simultaneous decoupled control of $\ddot{x}$ and $\ddot{y}$. Future formalization of this "pitch and roll" method with Lie brackets (as in [47]) could lead to a closed-loop nonholonomic yaw controller.

Flight Simulation

The experimental drag data and voltage to force mapping, as well as the sensor noise discussed below, are included in the simulation model. The simulation dynamics time-step is 10μs. This is sufficient, because if the ionocraft rolls or pitches by applying the maximum thrust that it is capable of producing (approximately 0.5 mN by firing two of its thrusters simultaneously and leaving the other two off), it would change roll or pitch angles by fewer than 10^{-4} degrees within one simulation time-step. The measurement and hand-tuned PID

control blocks update at 100Hz, which is the sample rate used when collecting experimental flight data with the MPU-9250 9-axis IMU with the MotionFusion algorithm on [66]. The documented noise power from the IMU on $\ddot{x}, \ddot{y}, \ddot{z} = 300\mu\text{g}/\sqrt{\text{Hz}}$. The noise power on the Euler angles is undocumented for the Digital Motion Processing unit. Direct measurement of the noise power of a stationary signal is $25\text{nrad}/\sqrt{\text{Hz}}$. During the simulation, we increase the Euler angle noise power by a factor of 40x as well as increase the accelerometer noise power by a factor of 10x. These increases provide overestimates of the noise signals in order to better prepare for future controlled flight of a fabricated device outside a laboratory setting.

Open loop maneuvers have been encoded to demonstrate the future potential of controllability over arbitrary shapes in the X-Y plane. The simulation results, shown in Fig. 4.22, shows a square flight pattern, control input, noisy states, and true state variables. Because direct measurements of the global positions X, Y, and Z are unavailable, the global positions drift over time. The raw accelerometer data for $\ddot{z}$ provides a reference for maintaining altitude. However, the global Z position is only controlled by the local $\ddot{z}$ reading, so it does not exactly track gravity when pitch and roll are non-zero. This global Z drift is compensated for by controlling to a desired state of $\ddot{z} = .015\ m/s^2$.

Disturbance characterization of the system is not included because the currently collected drag data does not account for resultant body torques. Without characterizing these moments, any planar disturbance will only cause drift and will not test roll or pitch stability; subsequent drift recovery is not possible with the current implementation due to the lack of global position data.

Separate simulations with variation in force produced by each thruster (e.g. from fabrication variation) at a given controller-outputted input voltage show loss of X-Y controllability above 1% variation and loss of hover functionality at 10% force variation. This is due to the hand-tuned PID controllers and could be improved with either more robust controllers or an in-line calibration method prior to takeoff.

Contributions and Conclusions

Succinctly, the contributions of this work were:

- Force-voltage characterization, both static and dynamic, of the highest thrust density ionocraft to date.
- Aerodynamic drag characterization of a centimeter-scale ionocraft using a low-speed wind tunnel.
- Repeated flight with streaming IMU data and individually addressable thrusters, opening the door for a feedback loop to be closed for the first time.
- Simulated controlled flight of a ionocraft in arbitrary X-Y trajectories using largely empirically derived values for performance.

Validation of using a high voltage time varying signal in tandem with an applied DC bias above the corona discharge initiation point to modulate thrust indicates that a future low mass power and control circuit could use a similar topology to Karpelson et al [44][45]. A low mass optical flow sensor similar to one fabricated in [23] could be used in conjunction with IMU data to stabilize absolute position as well as attitude. Assuming a single Flex PCB could be shared for the 9-axis IMU, control ASIC, driver circuit, and optical flow sensor, a total mass budget on the order of 100mg could be expected. This should be well within the capabilities of future ionocraft designs, opening the door for controlled flight of a 2cm by 2cm microrobot with only high voltage DC bias, low voltage (for ICs), and ground wires, with no external sensors.

The aerial thrust density measured in this work is still far below the theoretical maximum. Further, while increasing the number of emitter wires per thruster improved the maximum force output compared to prior work, it did not come with a large benefit to thrust-to-weight ratio. Future designs should look to maximize thrust density by increasing the number of emitter tips per collector grid and optimizing the tip spacing; they should also include mechanical affordances to decrease the number of required adhesive joints and additional components per emitter wire. Process development to further enhance the electrode geometric asymmetry (e.g., by creating tips with lower radii of curvature) should both decrease the required voltage for flight as well as allow for operation in a higher efficiency regime at the cost of output force.

Chapter 5

A Path to Power Autonomy and Other Future Directions

I believe that the future is filled with important discoveries that will further increase the advantages of EHD while diminishing the downsides. In this section, I will point future researchers in a number of directions that I see as having great potential.

Research questions to answer:

- What near-term possibilities are there for continued scaling of corona-discharge based EHD force?
- What would an autonomous ionocraft system design look like in terms of energy and mass breakdown?
- What major alternative approaches remain relatively underexplored despite their promise?

5.1 A Preface on Efficiency

Theory dictates, from Equations 2.17 and 2.16, that thrust efficiency should scale inversely with thrust in an EHD system. In terms of robot design, this represents a tradeoff in necessary battery energy and power density versus necessary size to produce the required lift force. For example, at an efficiency of 2 mN/W, projected maximum thrust is on the order of 100 N/m^2. Neglecting any mass besides the battery for this simple calculation, this would require storage with a density of at least 5 kW/kg and, for a 250 mg total robot mass, a thruster area of at least 25 square millimeters. At 10 mN/W, a reduction in electric field from 3×10^6 V/m to 5×10^5 V/m, a 1 kW/kg power density is required; the resulting maximum thrust of 2.5 N/m^2 requires 1000 square millimeters to lift 250 mg. Noting the comparisons with other mechanisms in Section 1.1, and due to the fact that thrust scales proportionally to the square of the electric field and efficiency scales only linearly, it would

seem that EHD systems make the most sense when they can take advantage of the highest possible power density storage.

The reality of current designs (e.g., those shown in Chapter 4) is that even 2 mN/W is difficult to achieve in practice for an aggressively scaled ion thruster. Current designs operate in the range between 1 mN/W and 2 mN/W at takeoff. The cause for this is rooted in the d/r ratio discussed in Section 2.1. Even with lithographically defined silicon asperities, the drift field outside the ionization region is relatively high following corona ignition. As the maximum breakdown field increases between the two electrodes as a function of decreasing distance, the theoretical "minimum" thrust efficiency becomes even lower. Ultimately, the only path forward for corona discharge based EHD thrusters is in new emitter designs with much smaller radii of curvature. This may not actually require moving entirely away from DRIE-defined processes in silicon; there are a few reports of "high" aspect ratio silicon nanopillar definition using DRIE (e.g., [11]), although the resultant structure height is probably not large enough for use with an EHD thruster that has a cathode-anode distance in the hundreds of microns. Independently, I have seen silicon wires formed post-DRIE with aspect ratios on the order of 800 (Figure 5.1). Ensuring device lifetime for structures such as these (see Section 4.2) would require careful process development.

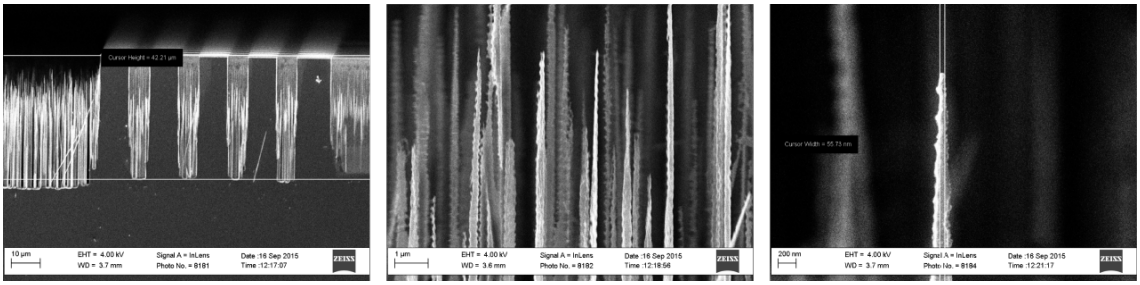

Figure 5.1: Silicon wires remaining post-DRIE, with aspect ratios on the order of 800. It is possible these wires are a result of etching and subsequent redeposition of the oxide hard mask in this process; they demonstrate the possibility of producing structures with high enough aspect ratio and low enough tip radius for potential increase in d/r ratio of an EHD thruster.

5.2 Future Power System Design

High Voltage Circuitry

For future corona discharge based thrusters we will assume that a high voltage DC bias is applied to the common collector electrode such that corona discharge is already initiated. Operating in this manner should be more efficient, as the plasma sustaining voltage is lower than the inception voltage; this indicates that energy is lost in "striking the plasma." In

this case, only a dynamic voltage range corresponding to the useful operating swing of the thrusters is required. For typical electrode geometries this is a range of approximately 300V. Simulation in [17] showed that controlled flight is possible with a thrust modulation bandwidth of 100Hz. Suddenly, the "big, scary" question of how to control a robot using such high voltages has become much more tractable, and it turns out we can borrow from the (quickly growing) body of literature on miniature, low mass drive circuits for piezoelectric actuators.

The first step is to generate the high voltage DC bias. Recent work on high voltage DC conversion, specifically for ion thrusters, has shown impressive power densities [96] (1.2kW/kg) with a step-up ratio of roughly 200 from an initial 200V. Their design consisted of three stages: a full-bridge resonant inverter, a high voltage transformer, and a six-stage Cockcroft-Walton voltage multiplier. Miniaturization of this design would require high voltage CMOS, a low mass transformer, and high voltage diodes. The X-Fab XDM10 process provides high voltage transistors and trench-isolated high voltage diodes (>350V breakdown), and extremely high efficiency DC-DC converters up to 400V have been previously demonstrated in the process [79]. Hand-wound low mass transformers have been demonstrated with a combination of laser cut steel cores and high-gauge wire [45].

Piezoelectric actuators, previously demonstrated for both flying and walking microrobots, require significant electric fields and, especially in the case of the former, high power densities. The Harvard Microrobotic Fly, for example, uses piezoelectric actuators requiring drive voltages in the range of 200-300V [44], in line with what we may expect a future ionocraft to require. Batteries and solar cells with energy densities suitable for microrobots generate output voltages below 5V, and stacking these in series in order to generate high voltage signals may not be possible due to packaging overhead and efficiency degradation (e.g., due to "weak-link" cells). Step-up ratios on the order of 10-100 are therefore required in most conceivable implementations. A large number of circuit topologies can deliver these ratios; selection requires specifically assessing the ability to miniaturize (both in terms of mass and effects on efficiency) and fabricate the circuit. Promising candidates include the tapped-inductor boost converter and bidirectional flyback converter. Steltz et al and Karpelson et al provide overviews of power system design choices for piezoelectric actuators [82], and for flapping wing microrobots more specifically [42]. Implementations for FMAVs with experimental results are given in [44, 43, 45].

Candidate Battery and Solar Cell Technologies

A battery technology can be evaluated based on its specific energy (typically in Wh/kg, or J/cc), with some caution towards ensuring that required discharge rates are feasible for the chosen chemistry and won't significantly degrade lifetime. A large challenge in evaluating batteries is their amenability to miniaturization; for most, it is not immediately clear how scaling will impact performance or packaging overhead percentage when looking at most papers. Thin film batteries being developed for wearable applications share many of the

design constraints as those for microrobots, including high (areal) energy densities, variable and often high potential discharge rates, simple fabrication, and long-term rechargability.

Flexible (i.e., thin film) batteries with high energy densities have been demonstrated; for example, >1 Wh/kg lithium ion [48] as well as 6.98 mWh/cm^2 and over 100 Wh/kg for other lithium ion (graphite and lithium cobalt oxide) batteries [69]. Some of these thin film battery technologies lack proper current densities and discharge rates for use in ionocraft (e.g. about 100μA/cm^2 1C discharge for [48]), but cutting edge batteries approach 2 mA/cm^2 [69]. While the latter case presents an almost ideal candidate for flying microrobots, there is a remaining challenge of fabricating small active area batteries without undue packaging overhead; the impressive performance listed is extracted from a much larger battery. Duduta et al [22] recently demonstrated a thin film lithium-ion battery using laser micromaching techniques that achieved a 2 mAh capacity while massing only 140 mg (roughly 2 cm by 1 cm active area, about 43 Wh/kg density), with a power density on the order of 1 kW/kg. The authors note they have also tested a 0.1 mAh, 14 mg battery with similar power densities.

Carbon nanotube-based thin film supercapacitors are an additional exciting active research topic, with demonstrations of extremely high power densities and reasonable energy densities (on the order of 50 kW/kg and 6 Wh/kg, respectively) [39]. These devices have the benefit of relatively high potential discharge rates (over 1mA/cm ^{2} shown). Lithium-air batteries also represent a promising future direction due to extremely high theoretical energy densities [74].

We can set up a toy problem for a high level evaluation. Assume that ionocraft are deployed with the goal of flying for 5 minutes before recharging. Assuming a drag-limited flight speed of $5m/s$ this corresponds to, roughly, a maximum travel distance of 1.5 km. With a simple model for EHD efficiency as $\kappa/\mu E$, where κ is some term accounting for loss in power transmission between the battery and the propulsion system, we can derive the required energy and power densities of the battery as a function of applied electric field. Assuming energy storage can account for only half of the total robot mass adds an additional factor of 0.5 to the efficiency equation. We will assume thrust is equal to Equation 2.16, with no deviation from the ideal maximum. The results are shown in Table 5.1. Note that the battery from [22] is only on the edge of feasibility for a centimeter-scale (e.g. <100 cm^2) EHD flier, but the battery presented in [69] could enable minutes of flight depending on packaging mass overhead.

Solar Power Area Optimization

EHD represents a direct transduction of electrical power to useful mechanical work; it would be an extremely elegant solution to power the device entirely from solar energy. Wireless takeoff of a flapping wing centimeter-scale robot was recently demonstrated using an external 976 nm laser shining at a high voltage solar cell with 200-suns intensity [36]. It turns out that, on paper, operation at one-sun illumination is not outside the realm of possibility, although it will require progress on quite a few fronts. Multi-junction silicon solar cell arrays fabricated on SOI wafers alongside CMOS circuits have been demonstrated with efficiencies

Table 5.1: Energy storage requirements as a function of various performance parameters for a 5 minute mission assuming battery mass can only account for half of the total robot mass.

Electric Field (V/m)	κ	Required Power Density (kW/kg)	Required Energy Density (Wh/kg)	Size For 250mg Robot (cm^2)
3×10^6	1.0	12	1000	0.3
3×10^6	0.75	16	1333	0.3
1×10^6	1.0	4	333	2.5
1×10^6	0.75	5.3	444	2.5
5×10^5	1.0	2	167	10
5×10^5	0.75	2.7	222	10
1×10^5	1.0	0.4	33	251
1×10^5	0.75	0.5	44	251

greater than 11% and output voltages above 80V [34]. Their 100μW of power generated at a 2.3 mg chip mass corresponds to a power density of only 43.5 W/kg; with aggressive process development (e.g. wafer thinning) it may be possible to increase that number, but unlikely to levels plausible for flight. Printed thin-film solar cells can demonstrate much more impressive energy densities (e.g., >100kW/kg [49] estimated from data), but struggle with stable packages for small cell sizes. Of course, this is still a relatively low areal power density for realistic efficiencies, and would require quite a large flat area to conceivably fly.

The question is, given a "flying postage stamp", what is the correct ratio of solar cell area to EHD thruster area in order to fly in full sunlight indefinitely? It turns out that it is straightforward to find a solution to this question given a specific solar cell efficiency.

Assuming a constant average thickness for thruster and solar areas and that no area can be both solar and a thruster, then:

$$m_t = \phi A_t = \phi \alpha_t A_{tot} \tag{5.1}$$

$$m_s = \psi A_s = \psi \alpha_s A_{tot} \tag{5.2}$$

Where ϕ and ψ are the respective areal densities, α is the fraction of total area devoted to that subsystem, and where the subscript t corresponds to thruster and s corresponds to solar.

Assuming we want to maximize payload capacity with respect to area of the thruster, then we need to balance produced force with the force due to gravity on the mass of solar and thrusters:

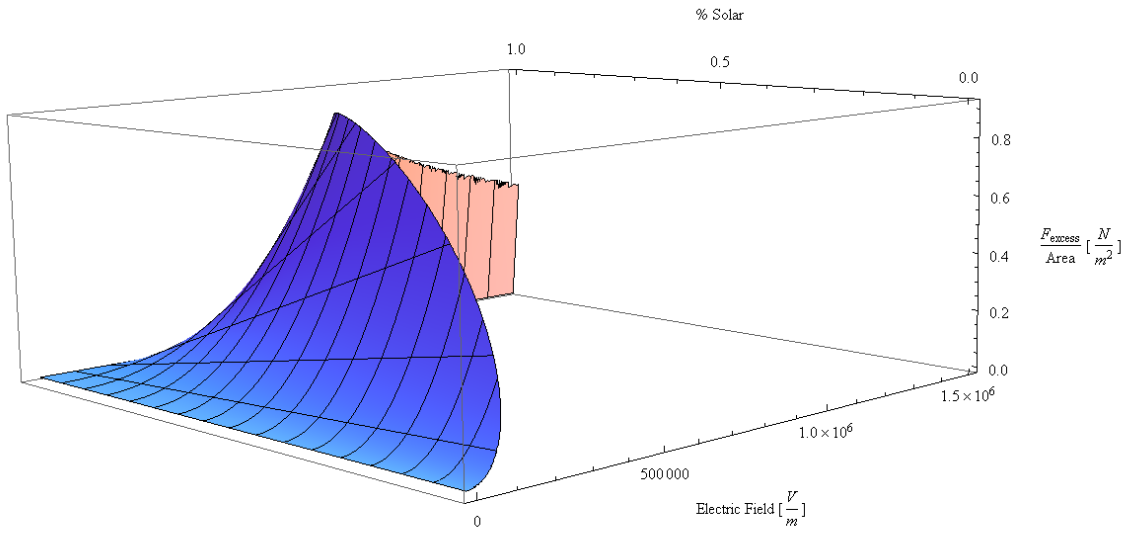

Figure 5.2: Surface plot of Equation 5.4 in the region satisfying Equation 5.8.

$$F = \frac{9}{8}\epsilon_0 A_t E^2 \tag{5.3}$$

$$F_{excess}/A_{tot} = \frac{9}{8}\alpha_t \epsilon_0 E^2 - 9.8\phi\alpha_t - 9.8\psi\alpha_s \tag{5.4}$$

Note that this assumes a space-charge limited current. We also need to take into account the power consumption of the thrusters versus the power generation from solar. Assuming our goal is to fly in full sunlight directly from solar power, and that we can neglect any conversion efficiency (or that those losses are bundled into the solar efficiency):

$$P_t = IV = \frac{9}{8}\epsilon_0 \mu A_t E^3 \tag{5.5}$$

$$P_s = P_{inc} A_s \theta_s \tag{5.6}$$

$$P_s \geq P_t \tag{5.7}$$

$$A_s/A_t \geq \frac{\frac{9}{8}\epsilon_0 \mu}{P_{inc}\theta_s} E^3 \tag{5.8}$$

Where θ_s is the solar conversion efficiency. We want to maximize the excess force while satisfying our power generation requirements.

There is another (more "algebraic") way to attack this problem. Again, assume $m_t = \phi A_t$ and $m_s = \psi A_s$ (Equation 5.1):

$$P_s = \frac{P_{inc}\theta_s}{\chi} m_s = \delta m_s \tag{5.9}$$

$$P_s = P_t = \frac{9}{8}\epsilon_0 \mu A_t E^3 = \frac{\frac{9}{8}\epsilon_0 \mu m_t}{\phi} E^3 \tag{5.10}$$

$$E^3 = \frac{P_s \phi}{\frac{9}{8}\epsilon_0 \mu m_t} \tag{5.11}$$

$$F = \frac{9}{8}\epsilon_0 A_t E^2 = \frac{9}{8}\epsilon_0 (\frac{\phi P_s}{\frac{9}{8}\epsilon_0 \mu m_t})^{2/3} \frac{m_t}{\phi} = (\frac{\frac{9}{8}\epsilon_0}{\phi})^{1/3} (\frac{\delta}{\mu})^{2/3} (m - m_t)^{2/3} (m_t)^{1/3} \tag{5.12}$$

$$(\frac{\frac{9}{8}\epsilon_0}{\phi})^{1/3} (\frac{\delta}{\mu})^{2/3} = \rho \tag{5.13}$$

$$\frac{dF}{dm_t} = \rho \frac{m - 3m_t}{3m_t^{2/3}(m - m_t)^{1/3}} \tag{5.14}$$

$$\frac{dF}{dm_t} = 0 \Rightarrow m = 3m_t \tag{5.15}$$

This optimization by mass results in the same finding as the prior optimization by area; we see that when attempting to fly based on direct solar power, the ratio of solar to thruster area, and therefore mass, is independent of the design and equal to 2.

5.3 Multi-stage Thrusters

The output force of an EHD thruster is related to the ion current density. Typically we treat the ion current as arising solely through drift in the applied electric field, but in reality there is also a component of current due to the freestream air velocity. In theory, by stacking multiple thrusters "in series," the output force will scale superlinearly for a given voltage due to increased inlet air speed.

Concretely, the expanded equation for output force is given in:

$$j = \rho(u + \mu_i E) \tag{5.16}$$

$$T = \frac{F}{A} = \frac{jd}{\mu_i} = \frac{\rho(u + \mu_i E)L}{\mu_i} \tag{5.17}$$

where ρ is the ion charge density and u is the freestream air velocity. Note that in the space charge limited case the same maximum current applies, and there will be no benefit from this effect. If we assume a sub-maximal electrical field intensity of $5e5V/m$, then ion velocity is approximately $100m/s$. If every stage can be expected to increase the fluid speed by approximately $5m/s$ this represents a possible route towards scaling device thrust per

volume. It should also be noted, however, that thrust efficiency in terms of $\frac{N}{W}$ is expected to decrease with inlet air velocity, as in Equation 2.18.

An alternative would be multiple collector electrodes per each thruster in a "triode" or even "tetrode" style. Initial results from prior work of Masuyama [56] is promising. In this case, we would be effectively increasing the drift distance of the emitted ions by staging our electrodes such that ions bypass collectors. This can be accomplished through clever geometric design. Note that, although a good deal of literature exists for proper multi-stage electrode design in vacuum tubes and field emitter arrays, it is not directly applicable; often they assume semi-ballistic emission trajectories of electrons, whereas with the number of ion-neutral collisions occurring when operating at atmosphere, ions will more readily follow their direct field lines.

As in [56], the force produced by a multi-collector thruster can be approximately described with:

$$F = \frac{I_1 d_1}{\mu} + \frac{I_2 d_2}{\mu} = \frac{I_1(d_1 + \chi d_2)}{\mu} \tag{5.18}$$

where χ is a factor that relates the two currents ($\chi = I_2/I_1$) and is governed by the fraction of ions that bypass the intermediate collector electrode. Masuyama showed some promising results (i.e., a χ of 0.3 prior to failure), but also noted difficulty in arriving at the correct geometric and applied voltage parameters to make use of this effect. It is evident that in the space charge limited case this will result in a higher output force for the same input power, and hence a higher thrust efficiency. Ultimately, I believe this is an extremely promising route, but one that will require a good deal of experimental work before showing any substantial benefit.

Research questions to answer:

- Can a multi-stage thruster be constructed such that the force benefits outweigh additional mass and drag?
- Is there an assembly technique or electrode design that leads to a sublinear mass scaling with number of stacked thrusters?

5.4 Designs With Airfoils

Ion-engine Powered Microgliders

Although natural systems typically operate in a flapping rather than soaring regime at the Reynolds numbers expected for a centimeter scale ionocraft, there has been some interest in investigating centimeter-scale gliders. Any amount of lift from wings is beneficial; with the already high thrust to weight ratio of EHD, a fixed wing design may prove the fastest route

towards autonomous operation. Recent work at the meter scale has seemingly validated this claim [96].

The vehicle would be designed similarly to a training glider, with a long fuselage providing stability for thin airfoils. It will use two MEMS elevons [46] mounted on the tail to control pitch and roll. Yaw can be controlled by differential actuation of the wing-mounted thrusters. The ion thrusters will be placed along the leading edges of the wings. An approximate design is depicted in Figure 5.3. Previous work on an elevon-controlled MAV glider found lift to drag ratios in the range of five to ten from a 10 cm-span airfoil operating at a Reynolds number of around 7000 [93]. Until wind tunnel measurements are performed using sample airfoils, we will base our design on an estimated lift to drag ratio of five. Assuming the same thickness of airfoil and fuselage material as in [93] but halving the area, we can assume a combined airfoil and fuselage mass of about 100mg. Each microfabricated control surface can be brought to about 8mg with process optimization. The electronics package will be mounted on the side of the fuselage, close to the center of mass.

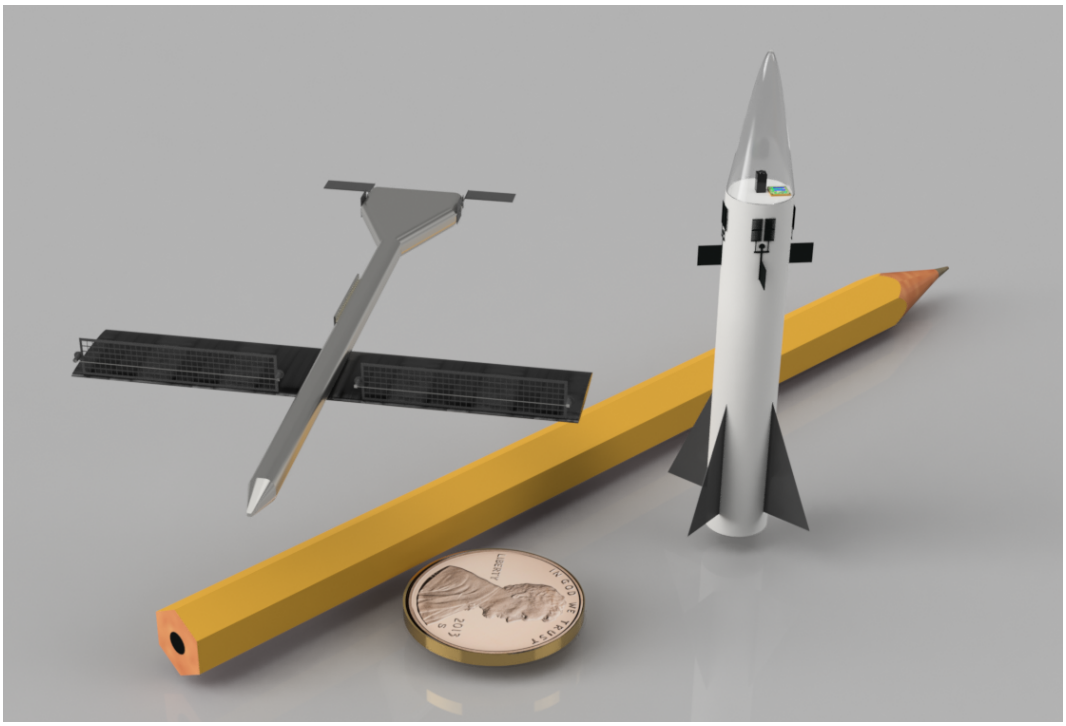

Figure 5.3: Rendered depictions of the proposed pico air vehicle platforms in [16]. On the left is an atmospheric ion thruster powered fixed wing vehicle.

Assuming we want to operate at a thrust efficiency of 10 mN/W, our operating drift field from Equ. 2.18 will be $500kV/m$ and our theoretical thrust from Equation 2.13 is therefore approximately $2.5N/m^2$; a four-fold reduction in thrust from that measured in prior work (Section 3.2). For our vehicle mass of 216mg and an estimated lift to drag ratio of 5 we

require about $400\mu N$ of EHD force. With thin film lithium cobalt oxide - graphite batteries (as in [69]) that have a power density of $1W/g$ and our thrust efficiency of $10N/W$ we require about 40mg of battery. Assuming an areal energy density of $1.4J/mm^2$ without packaging, this means we need about 150 square millimeters of battery for a flight time of one hour. If the thrust to weight ratio of our ion thrusters scales proportionally to the decreased drift field we can expect a ratio of about 5; this means we will need a minimum of about 60mg and 240 square millimeters of thruster, producing about $600\mu N$ of force, for a total 1:1 vehicle thrust to weight ratio after accounting for lift. For maneuvering, the drift field of the thrusters can be increased at the cost of efficiency and therefore flight time.

Research questions to answer:

- How can atmospheric ion thrusters be assembled and/or affixed along the edges of a airfoil?
- How large would a fixed-wing vehicle need to be before it is possible to carry commercial batteries for power?

Autorotation for Dispersion

One of the motivating application spaces for flying microrobots is that of distributed air quality monitoring. Imagining a plane flying overhead and dropping ten thousand ionocraft out the back; they slowly drift down to the ground, rotating like maple seeds, while periodic updrafts both natural and from their ion thrusters carry them far and wide. This would be a truly biomimetic mechanism of spreading our wireless sensor networks, replicating the successful reproductive strategy of countless trees and flowers.

Prior work has investigated airborne deployment of fully passive autorotating sensor nodes [87, 73]. The nodes themselves were roughly 12cm tip to tip, with a 2cm $\times$ 2cm "brain" at the root and a PCB wing reinforced with metal traces. The experiments were largely successful in demonstrating feasibility. Many of the challenges that did arise had to do with the fully passive nature of the nodes; they had no way to course correct, if autorotation was slow to start due to release, they had no way to extend their lifetime; and once landed the nodes were often lost due to obstructions blocking communication and solar power. An actuated "robotic samara" monowing has also been demonstrated [72]. It is roughly 20cm $\times$ 20cm and uses a brushless DC motor-based propeller for thrust. Servo-actuation of the airfoil allows for controlled flight and sustained hover.

At small sizes and masses, both animal wings and seeds make a shift from membrane wing based flight to bristle-based structures, as leading edge vortices become less reliable. Recent work shows the ability of microfabricated devices to replicate the floating ability of dandelion seeds [14] by generation of a floating vortex above the airfoil. Although it is unclear how such a device could be actuated (or what the correct mounting orientation for the ion thruster would even be), it represents a very interesting and mechanically simple path towards increased dispersal of miniature ionocraft-based motes.

Research questions to answer:

- Does an SOI silicon airfoil possess enough mechanical rigidity for autorotation at the centimeter scale?
- Do etch holes in an SOI silicon airfoil affect the behavior of a biomimetic autorotator?
- Can the total payload mass of a useful sensor and thruster device be made low enough to allow for bristle-based dispersal methods (e.g., dandelion seeds)?
- Where is the correct place on the device to apply thrust in order to increase dispersion for both autorotating and bristle-based devices?

5.5 Field Emission for EHD

Electrohydrodynamic thrust merely depends on the presence of ions in an applied electric field; it does not necessarily matter how the ions are generated. As interelectrode gaps continue to decrease, Townsend avalanche breakdown (i.e., the primary mechanism for corona discharge) ceases to be the dominant ionization route. Instead, at gaps on the order of 10‘s of microns, field emission begins to take over.

At a high level, field emission refers to the ejection of electrons from a bulk material into a non- or weakly- conductive medium through quantum tunneling. The tunneling is assisted by, typically, strong applied electric fields that “shape” the potential gap until the probability of tunneling for conduction band electrons is high enough. Field emission is therefore a strong function of the emitter material work function and the dielectric medium properties.

A field emission based EHD thruster would operate with electrons injected by the cathode into some drift gap, where they would attach to O_2 molecules, which would then be accelerated to a collector anode (Figure 5.4). This would decouple the ion drift field from the ion generation, circumventing the challenge with thrust efficiency due to $\frac{d}{r}$ ratio in a corona discharge based system. The challenge would then become one of fabricating atmospherically stable field emitters, injecting electrons into the drift gap without undue losses to the field emitter gate electrode, and ensuring that electron attachment occurs prior to traversal through some large fraction of the gap; electron drift is wasted as thrust.

Field Emission Models

A relatively simple equation approximated from the Fowler-Nordheim cold metal cathode tunneling equation is given in 5.19. This equation is commonly used to extract characteristic parameters of field emission sources thanks to its close approximation of proper current-voltage characteristics[59].

$$I/V^2 = A \cdot exp(-B/V) \tag{5.19}$$

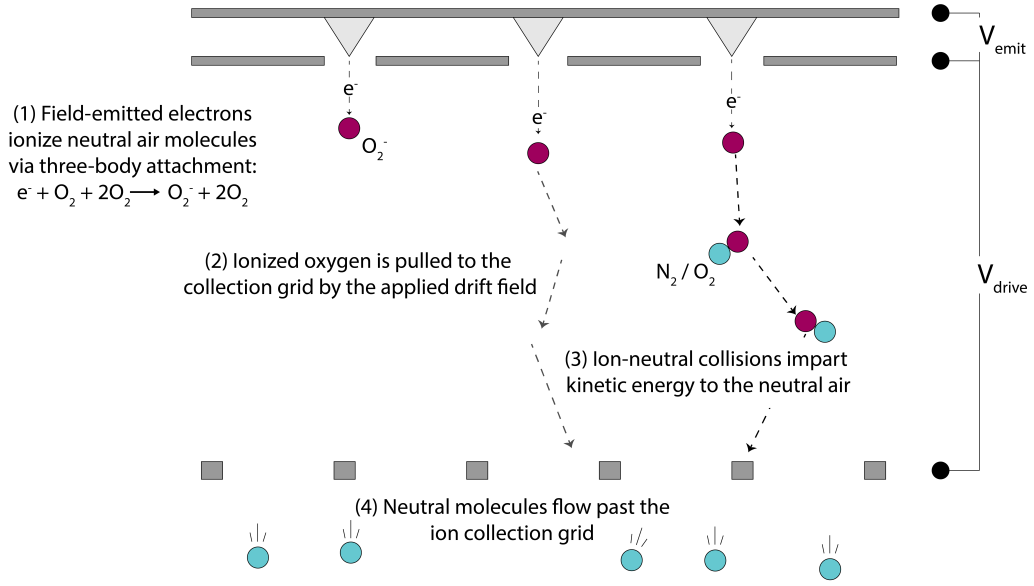

Figure 5.4: A multi-stage EHD thruster based on field emitted electrons.

with

$$A = 1.42 \cdot 10^{-}6 \cdot \alpha \cdot \beta^2/\phi \cdot exp(10.4/\phi^{0.5}) \tag{5.20}$$

$$B = 6.44 \cdot 10^7 \cdot \phi^{3/2}/\beta \tag{5.21}$$

where ϕ is the emitter work function in eV, V is the turn-on voltage in volts, I is current in amperes, α is emitter area in cm^2, and β is

$$\beta = \kappa_{tip}/d_{cathode-anode} \tag{5.22}$$

in cm^{-1}. Because data about the fabricated emission sources is confined to tip radius and tip depth, the emitter tip can be modeled as a "hemisphere on a post" to yield an enhancement factor κ [27].

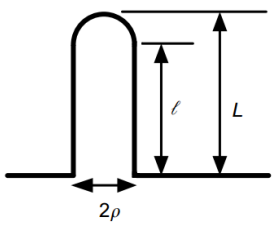

Figure 5.5: Hemisphere on a post geometry for field emission modeling. Adapted from [27].

$$\kappa_{tip} = 1.2(2.15 + (L/\rho_{tip}))^{0.90} \tag{5.23}$$

Using 5.23 with 5.22 and 5.19 yields a theoretical current-voltage characteristic curve by supplying only field emitter tip radius of curvature and depth, distance from anode to cathode, and material work function (2.6 for bare silicon [31]) — see Figure 5.7.

Electron Attachment

Beyond low voltage field emission, the objective of this work would be to predictably produce negative ions in a separate device section. As this will be performed at STP, it is expected that the three-body attachment reaction will dominate [80].

$$e + O_2 + (O_2, H_2O) \longrightarrow O_2^- + (O_2, H_2O) \tag{5.24}$$

Although the related theory is beyond the current scope, prior work has found experimental attachment times that agree with this assertion [80]. Given a critical attachment time for the three-body reaction and the drift velocity of the electrons, it is possible to predict the amount of unattached electrons (and therefore generated ions) from a given stream of emitted electrons. An important unit of measure for this study is the Townsend (Td), where 1Td = $10^{-21}V/m^2$. The Townsend is a measure of the "reduced electric field" and is found from the ratio E/N where E is the electric field and N is the concentration of neutral particles present within that field. This allows direct comparison between different experimental conditions, especially pressure. For example, the drift velocity of an electron at 1Td measured at 1/100 of atmospheric pressure will be identical to the drift velocity measured at atmospheric pressure. Using the fundamental relationship $PV = Nk_bT$, note that the number of neutral particles is $2.68 \cdot 10^{25} molecules/m^3$. This means that an electric field of $2.68 \cdot 10^4 V/m$ at STP will yield 1Td of reduced electric field.

With the data from [80], it is possible to predict a decay curve for the field emitted electrons in a device. Assuming a reduced electric field of 1Td in the second stage of the device, an electron drift velocity of $6.35 \cdot 10^4 cm/s$ is expected [32]. Multiplying this critical attachment time by the drift velocity yields the critical attachment length, λ, and the fraction of unattached electrons in the stream should decay according to standard probabilistic theory as a function of $e^{-\lambda/x}$ where x is the distance traveled — see Figure 5.6. Noting that over 95% of the electrons will have attached within 0.5mm at 1Td. The necessary voltage to achieve an electric field of $2.68 \cdot 10^4 V/m$ at the distance of 0.5mm is then only 13.4V.

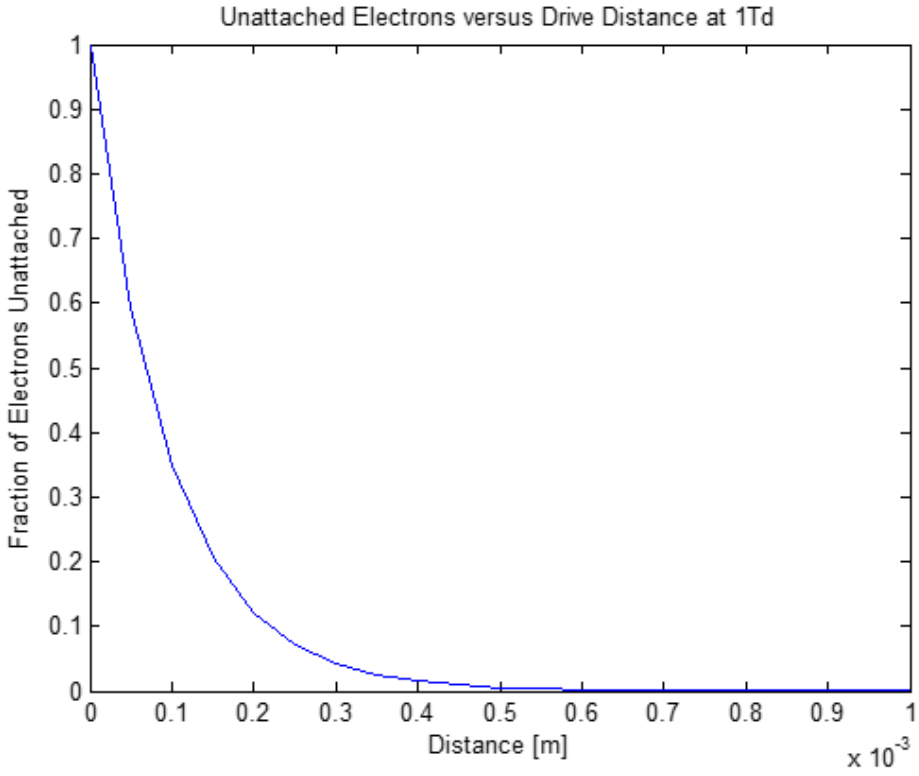

Figure 5.6: Unattached electron fraction as a function of distance at 1Td and STP.

Low Turn-on Voltage Field Emitter Arrays

In this section we will assume silicon field emission arrays are desired due to fabrication simplicity and availability of standard processes. Turn on voltage for field emission here has been defined as the point where the current reaches 1fA/tip in 5.19. For the Bosch DRIE process, post-fabrication tip sharpnesses can be expected to range from 10nm to 30nm with tip depths from 180nm to 800nm [59]. Using the Fowler-Nordheim equation allows us to predict the turn-on voltage for field emission as a function of these parameters with some high degree of confidence for a silicon field emission device. Depending on the actual dimensions of the tips produced from, for example, the SOIMUMPS Bosch DRIE process, turn on voltages of 400V to 1000V are expected with a 1 μm cathode-anode distance. It should be noted that much lower turn-on voltages have been demonstrated (e.g., on the order of 10V [21]), but these devices had extremely small cathode-anode distances and often required more complicated fabrication processes.

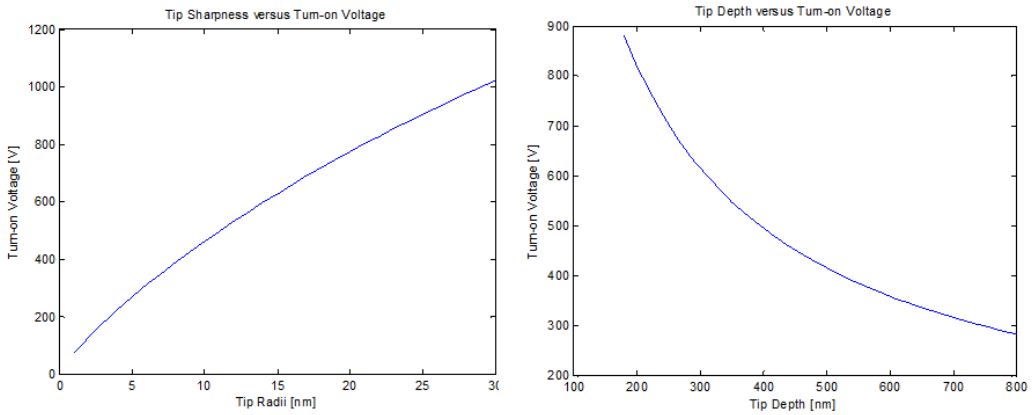

Figure 5.7: Field emission turn-on voltage simulation as a function of tip sharpness and tip depth model parameters. Assumed parameters: $1\mu m$ cathode-anode distance, $240nm$ tip depth (left), $20nm$ tip sharpness (right).

Thermal oxide sharpening of the post-fabrication tips would allow for even lower turn-on voltages. Although engendering a more complicated process flow, this change would allow for atomically sharp emission tips and lower the theoretical turn-on voltage to under 50V, which agrees with experimental data from [59] and [38].

A Possible Device Design

Silicon Field Emitter Array Fabrication

Gated silicon field emitter arrays are fabricated in a process adapted from [15], shown in Figure 5.8. A standard silicon wafer is used as a substrate. First, a 250nm thermal oxide layer is grown on the wafer. The oxide is selectively etched using a relatively anisotropic ICP etcher (primarily C_4F_8) to define discs of roughly 1μm diameter. A timed SF_6 RIE etches the silicon, undercutting the oxide discs but not so much that they are released. A buffered HF dip then removes the remaining oxide. The remaining "pyramids" of silicon have relatively dull tips, depending on the disc undercut; they are then thermal oxide sharpened (e.g. via dry oxidation at 950degC for 4hr, as in [55]). About 0.5μm of high-temperature oxide is then deposited via LPCVD, following by about 0.3μm of doped polysilicon. A timed CMP removes the polysilicon "bump", exposing oxide. Pads and structure isolation is now defined via photolithography and an RIE etch of the polysilicon. Finally, a timed BHF dip reveals the gated silicon field emitter tips.

Fabrication was a challenge due primarily to the timed RIE etch for undercutting the oxide discs and defining the initial sharpness, as well as the timed CMP step having poor wafer uniformity. No electrical characterization was performed for these devices, but it does represent a relatively straightforward fabrication process for high-density silicon field emitter arrays possible in the Berkeley Marvell Nanolab.

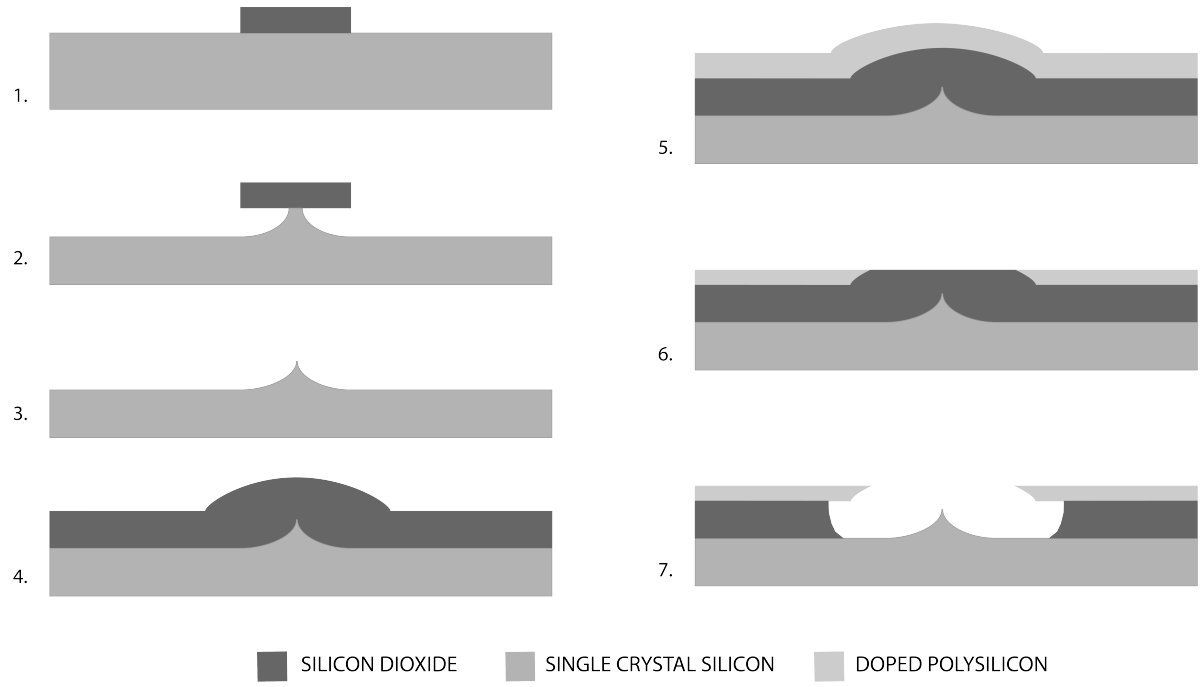

Figure 5.8: Silicon field emitter array process flow. 1. A thermal oxide layer is grown and selectively etched. 2. A timed RIE etch undercuts the oxide discs, leaving silicon pyramids. 3. A buffered HP dip leaves blunted tips; subsequent thermal oxide sharpening sharpens them. 4. High-temperature oxide is deposited to set the cathode-anode distance. 5. A layer of doped polysilicon (i.e., the gate material), is deposited. 6. CMP flattens the resulting polysilicon "bump" and reveals the previously deposted oxide. 7. A timed BHF dip reveals the gated silicon field emitter tips.

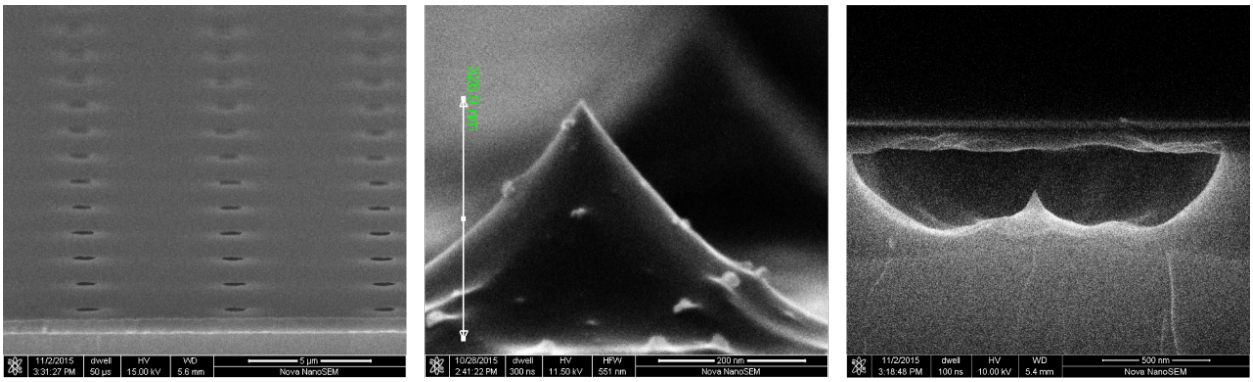

Figure 5.9: Silicon field emitter arrays fabricated in the Marvell Nanolab. It would be expected that field emission devices with these geometries would be unstable when used in air unless hermetically sealed under vacuum prior to operation.

Graphene Encapsulation

Field emitter performance rapidly degrades when operated in atmosphere due to absorption onto the emitter surface altering the effective radius and/or work function, as well as ion bombardment following ionization events within the emitter - gate gap. Some success in atmospheric operation has been demonstrated with field emitters having an emitter - gate gap smaller than the mean free path of electrons in air (on the order of 100nm). This means that impact ionization events between the emitted electrons and neutral air are unlikely, preventing degradation due to ion ablation. Field emission devices designed in this manner typically have extremely low turn-on voltages (e.g. 15V), but complicated and technically difficult fabrication processes and relatively low current densities. Graphene gate encapsulation may provide a path forward towards operating silicon field emitter arrays stably in atmosphere.

It turns out that graphene is highly transparent to electrons of specific energies [50]. At the same time, it has also been shown to be a near-perfect hermetic sealing material [91]. Transmission efficiency of over 95% has been shown for electron energies on the order of 0.5keV. Ultra-low voltage field emission devices, such as those created for atmospheric operation with nanometer-scale emitter - gate gaps, would produce electrons with insufficient energy to bypass the graphene efficiently. Silicon field emitter arrays, with onset voltages on the order of 100 to 1000V, are perfect. Relatively straightforward fabrication processes have been demonstrated for dry-transfer of graphene membranes over cavities [84]. Field emission triodes using transmission through graphene gates have been demonstrated [50].

Collector (Anode) Integration

Ideally the entire triode device would be constructed in a single process, but failing that, the next best thing would be for the anode electrode to be fabricated on a separate wafer with lithograhically-defined alignment structures. One simple idea is to use an SOI wafer and define collector grids in the device layer as shown in Chapters 3 and 4, then perform a backside through-etch of the handle wafer inside the "frame" of the grid. Care would have to be taken to prevent oxide breakthrough and subsequent destruction of the device layer grid electrode. The inter-electrode gap would then be set by the original handle wafer thickness; typical ranges that are able to be processed in the Berkeley Nanolab range from 400μm to 650μm. The obvious issue with this process is that it exposes silicon inside the ion drift gap. There is some numerical work indicating that a floating potential sidewall does not significantly affect performance with the correct geometry choices. Another option would be to deposit a dielectric coating prior to the oxide release of the collector grid; paralyene-C has been shown to be resistant to vapor phase HF for SOI processing [33].

Following wafer bonding or individual electrode manual bonding, there is now an additional consideration; how to get more air into the device. Either the field emission array process would have to be modified to include through-etches for air intake slots, or non-sealing standoffs would need to be place prior to bonding the anode.

Research questions to answer:

- Can an air-stable FEA be made with high enough current density?
- Can electrons be ejected through a graphene field emitter gate with the correct energy distribution to maximize electron attachment reactions for subsequent EHD force generation?
- Can a meso-scale integration method be devised for the collector electrode with enough precision to reliably create drift gaps on the order of 100μm?

Chapter 6

Conclusion

In the near future, swarms of millimeter scale robots will be vital and common tools in industrial, commercial, and personal settings. By enabling applications spanning from distributed gas and chemical sensing, to tangible 3D interfaces, to dynamic wearable devices, providing mobility platforms to low-power sensing and actuation nodes will push us that much closer to the dream of ubiquitous computing.

In this thesis I have presented a new path forward towards providing mobility for centimeter-scale flying robots. Unlike the majority of research in this area, the mechanism of propulsion is not biomimetic, but instead using electrohydrodynamics. It has unparalleled potential for robust construction, high thrust-to-weight ratio, and retaining functionality through a wide range of Reynolds numbers. The thrust itself is scale invariant, indicating a favorable scaling to low-mass systems. Just as importantly, the mechanism is relatively underexplored for propulsion; I believe that the future is filled with important discoveries that will further increase the advantages of EHD while diminishing the downsides. Much like the automobile has no natural analogue, we may end up with flying robots unlike anything found in nature.

I believe that I have laid out a solid foundation for understanding the underlying mechanisms behind corona discharge-based electrohydrodynamic thrust. Some of the early presented work shows that centimeter-scale ionocraft capable of lifting their own weight are possible with both simple rapid prototyped designs as well as microfabricated electrodes. I have demonstrated successfully that EHD is a viable mechanism for high thrust-to-weight ratio flight at this scale while overcoming various challenges associated with meso-scale assembly, electrode lifetime, and design robustness (e.g., to unwanted dielectric breakdown pathways). Finally, I have made strides towards controlled flight of a tethered quad-thruster ionocraft, with proof of concept displays of attitude control and simulated control with largely empirically derived device parameters. I hope that the final chapter of the dissertation provides some guidance for future researchers as to possible directions to take the work on these flying microrobots.

Ultimately, although my dissertation work is enough to demonstrate that atmospheric ion thrusters are viable for centimeter-scale robots, there is still a large gap between that conclusion and having a functional artificial insect. The remaining work is far beyond what

is able to be accomplished by a single graduate student, or even a single research group; it will require parallel effort in further actuator development, sparse computation control, meso-scale fabrication and assembly, power electronics miniaturization, and development of microrobot-specific ASICs, to name a few — and that's just to develop a usable robot platform.

In the future, I want to expand my focus to include research on multi-agent coordination and control, heterogeneous robot systems, and human-swarm interaction. This effort is inherently interdisciplinary and will require pulling from the domains of classical robotics, fundamental device and materials research, human-computer interaction, and distributed machine learning, to name a few. As such, it represents a tremendous opportunity for collaboration, for training a new generation of interdisciplinary investigators, and for forging new ties between the worlds of industry, academia, and design.

Bibliography

[1] Kazimierz Adamiak and Pierre Atten. "Simulation of corona discharge in point–plane configuration". In: *Journal of electrostatics* 61.2 (2004), pp. 85–98.

[2] Erdinc Altug, James P Ostrowski, and Camillo J Taylor. "Control of a quadrotor helicopter using dual camera visual feedback". In: *The International Journal of Robotics Research* 24.5 (2005), pp. 329–341.

[3] PO Bedolla, G Vorlaufer, P Sequard-Base, A Vernes, and F Franek. "Altitude dependence of electrohydrodynamic flow in an electrostatic lifter". In: *Journal of Electrostatics* 87 (2017), pp. 32–44.

[4] H Bondar and F Bastien. "Effect of neutral fluid velocity on direct conversion from electrical to fluid kinetic energy in an electro-fluid-dynamics (EFD) device". In: *Journal of Physics D: Applied Physics* 19.9 (1986), p. 1657.

[5] John Brandt and Michael Selig. "Propeller performance data at low reynolds numbers". In: *49th AIAA Aerospace Sciences Meeting including the New Horizons Forum and Aerospace Exposition*. 2011, p. 1255.

[6] Davide Cagnoni, Francesco Agostini, Thomas Christen, Nicola Parolini, Ivica Stevanović, and Carlo De Falco. "Multiphysics simulation of corona discharge induced ionic wind". In: *Journal of Applied Physics* 114.23 (2013), p. 233301.

[7] Francis X Canning, Cory Melcher, and Edwin Winet. "Asymmetrical capacitors for propulsion". In: (2004).

[8] J-S Chang, Phil A Lawless, and Toshiaki Yamamoto. "Corona discharge processes". In: *IEEE Transactions on plasma science* 19.6 (1991), pp. 1152–1166.

[9] Junhong Chen and Jane H Davidson. "Electron density and energy distributions in the positive DC corona: interpretation for corona-enhanced chemical reactions". In: *Plasma Chemistry and Plasma Processing* 22.2 (2002), pp. 199–224.

[10] Junhong Chen and Jane H Davidson. "Model of the negative DC corona plasma: comparison to the positive DC corona plasma". In: *Plasma chemistry and plasma processing* 23.1 (2003), pp. 83–102.

[11] Chang-Hwan Choi and Chang-Jin Kim. "Fabrication of a dense array of tall nanostructures over a large sample area with sidewall profile and tip sharpness control". In: *Nanotechnology* 17.21 (2006), p. 5326.

[12] Edward A Christenson and Paul S Moller. "Ion-neutral propulsion in atmospheric media." In: *AIAA Journal* 5.10 (1967), pp. 1768–1773.

[13] Beelee Chua, Anthony S Wexler, Norman C Tien, Debbie A Niemeier, and Britt A Holmen. "Electrical mobility separation of airborne particles using integrated microfabricated corona ionizer and separator electrodes". In: *Journal of Microelectromechanical Systems* 18.1 (2009), pp. 4–13.

[14] Cathal Cummins, Madeleine Seale, Alice Macente, Daniele Certini, Enrico Mastropaolo, Ignazio Maria Viola, and Naomi Nakayama. "A separated vortex ring underlies the flight of the dandelion". In: *Nature* 562.7727 (2018), p. 414.

[15] Meng Ding, Guobin Sha, and Akintunde I Akinwande. "Silicon field emission arrays with atomically sharp tips: Turn-on voltage and the effect of tip radius distribution". In: *IEEE Transactions on Electron Devices* 49.12 (2002), pp. 2333–2342.

[16] Daniel S Drew, Brian Kilberg, and Kristofer SJ Pister. "Future mesh-networked pico air vehicles". In: *Unmanned Aircraft Systems (ICUAS), 2017 International Conference on*. IEEE. 2017, pp. 1075–1082.

[17] Daniel S Drew, Nathan O Lambert, Craig B Schindler, and Kristofer SJ Pister. "Toward Controlled Flight of the Ionocraft: A Flying Microrobot Using Electrohydrodynamic Thrust With Onboard Sensing and No Moving Parts". In: *IEEE Robotics and Automation Letters* 3.4 (2018), pp. 2807–2813.

[18] Daniel S Drew and Kristofer SJ Pister. "First takeoff of a flying microrobot with no moving parts". In: *Manipulation, Automation and Robotics at Small Scales (MARSS), 2017 International Conference on*. IEEE. 2017, pp. 1–5.

[19] Daniel S Drew and Kristofer SJ Pister. "Geometric optimization of microfabricated silicon electrodes for corona discharge-based electrohydrodynamic thrusters". In: *Micromachines* 8.5 (2017), p. 141.

[20] Daniel Drew, Daniel S Contreras, and Kristofer SJ Pister. "First thrust from a microfabricated atmospheric ion engine". In: *Micro Electro Mechanical Systems (MEMS), 2017 IEEE 30th International Conference on*. IEEE. 2017, pp. 346–349.

[21] A. a. G. Driskill-Smith, D. G. Hasko, and H. Ahmed. "Nanoscale field emission structures for ultra-low voltage operation at atmospheric pressure". In: *Applied Physics Letters* 71.21 (Nov. 1997), pp. 3159–3161. ISSN: 0003-6951, 1077-3118. DOI: 10.1063/1.120276. URL: http://scitation.aip.org/content/aip/journal/apl/71/21/10.1063/1.120276 (visited on 12/19/2013).

[22] Mihai Duduta, Sebastien de Rivaz, David R Clarke, and Robert J Wood. "Ultra-Lightweight, High Power Density Lithium-Ion Batteries". In: *Batteries & Supercaps* 1.4 (2018), pp. 131–134.

[23] Pierre-Emile J Duhamel, Néstor O Pérez-Arancibia, Geoffrey L Barrows, and Robert J Wood. "Biologically inspired optical-flow sensing for altitude control of flapping-wing microrobots". In: *IEEE/ASME Transactions on Mechatronics* 18.2 (2013), pp. 556–568.

[24] A Eifert, T Baier, and S Hardt. "Small onset voltages in negative corona discharges using the edges of gold and aluminum foils as nano-structured electrodes". In: *Applied Physics Letters* 103.2 (2013), p. 023114.

[25] Henry A Erikson. "On the nature of the negative and positive ions in air, oxygen and nitrogen". In: *Physical Review* 20.2 (1922), p. 117.

[26] James Q Feng. "An analysis of corona currents between two concentric cylindrical electrodes". In: *Journal of Electrostatics* 46.1 (1999), pp. 37–48.

[27] Richard G Forbes, C.J Edgcombe, and U Valdr. "Some comments on models for field enhancement". In: *Ultramicroscopy* 95 (May 2003), pp. 57–65. ISSN: 0304-3991. DOI: 10.1016/S0304-3991(02)00297-8. URL: http://www.sciencedirect.com/science/article/pii/S0304399102002978 (visited on 12/03/2013).

[28] Nobuhiro Fujioka, Yoshihiro Tsunoda, Akira Sugimura, and Kenji Arai. "Influence of humidity on variation of ion mobility with life time in atmospheric air". In: *IEEE transactions on power apparatus and systems* 4 (1983), pp. 911–917.

[29] Emmanouil D Fylladitakis, Michael P Theodoridis, and Antonios X Moronis. "Review on the history, research, and applications of electrohydrodynamics". In: *IEEE Transactions on Plasma Science* 42.2 (2014), pp. 358–375.

[30] Christopher K Gilmore and Steven RH Barrett. "Electrohydrodynamic thrust density using positive corona-induced ionic winds for in-atmosphere propulsion". In: *Proc. R. Soc. A* 471.2175 (2015), p. 20140912.

[31] Robert Gomer. "Work Function in Field Emission. Chemisorption". In: *The Journal of Chemical Physics* 21 (10 Dec. 23, 2004), pp. 1869–1876. ISSN: 0021-9606, 1089-7690. DOI: 10.1063/1.1698681. URL: http://scitation.aip.org/content/aip/journal/jcp/21/10/10.1063/1.1698681 (visited on 11/13/2013).

[32] R Hegerberg and ID Reid. "Electron Drift Velocities in Air". In: *Australian Journal of Physics* 33.2 (Jan. 1980), pp. 227–238. URL: http://www.publish.csiro.au/paper/PH800227a (visited on 12/08/2013).

[33] Akio Higo, K Takahashi, H Fujita, Y Nakano, and H Toshiyoshi. "A novel Parylene/Al/Parylene sandwich protection mask for HF Vapor release for micro electro mechanical systems". In: *Solid-State Sensors, Actuators and Microsystems Conference, 2009. TRANSDUCERS 2009. International*. IEEE. 2009, pp. 196–199.

[34] Seth Hollar, Anita Flynn, Colby Bellew, and KSJ Pister. "Solar powered 10 mg silicon robot". In: *Micro Electro Mechanical Systems, 2003. MEMS-03 Kyoto. IEEE The Sixteenth Annual International Conference on*. IEEE. 2003, pp. 706–711.

[35] Bert Hölldobler, Edward O Wilson, et al. *The ants*. Harvard University Press, 1990.

[36] Johannes James, Vikram Iyer, Yogesh Chukewad, Shyamnath Gollakota, and Sawyer B Fuller. "Liftoff of a 190 mg Laser-Powered Aerial Vehicle: The Lightest Wireless Robot to Fly". In: *2018 IEEE International Conference on Robotics and Automation (ICRA)*. IEEE. 2018, pp. 1–8.

[37] Nels E Jewell-Larsen, Sergey V Karpov, Igor A Krichtafovitch, Vivi Jayanty, Chih-Peng Hsu, and Alexander V Mamishev. "Modeling of corona-induced electrohydrodynamic flow with COMSOL multiphysics". In: *Proceedings ESA Annual Meeting on Electrostatics, Minneapolis, Minnesota*. Citeseer. 2008.

[38] R.g. Joiner, R.g. Joiner, and A.I. Akinwande. "Silicon field emission arrays with atomically sharp tips: turn-on voltage and the effect of tip radius distribution". In: *IEEE Transactions on Electron Devices* 49 (12 Dec. 2002), pp. 2333–2342. ISSN: 0018-9383. DOI: 10.1109/TED.2002.805230. URL: http://ieeexplore.ieee.org/lpdocs/epic03/wrapper.htm?arnumber=1178002 (visited on 12/02/2013).

[39] Martti Kaempgen, Candace K Chan, J Ma, Yi Cui, and George Gruner. "Printable thin film supercapacitors using single-walled carbon nanotubes". In: *Nano letters* 9.5 (2009), pp. 1872–1876.

[40] NA Kaptsov. "Elektricheskie yavleniya v gazakh i vakuume". In: *Moscow, OGIZ* (1947).

[41] Zeev Karpas, Zvi Berant, and Oded Shahal. "Effect of temperature on the mobility of ions". In: *Journal of the American Chemical Society* 111.16 (1989), pp. 6015–6018.

[42] Michael Karpelson, Gu-Yeon Wei, and Robert J Wood. "A review of actuation and power electronics options for flapping-wing robotic insects". In: *Robotics and Automation, 2008. ICRA 2008. IEEE International Conference on*. IEEE. 2008, pp. 779–786.

[43] Michael Karpelson, Gu-Yeon Wei, and Robert J Wood. "Driving high voltage piezoelectric actuators in microrobotic applications". In: *Sensors and actuators A: Physical* 176 (2012), pp. 78–89.

[44] Michael Karpelson, Gu-Yeon Wei, and Robert J Wood. "Milligram-scale high-voltage power electronics for piezoelectric microrobots". In: *Robotics and Automation, 2009. ICRA'09. IEEE International Conference on*. IEEE. 2009, pp. 2217–2224.

[45] Michael Karpelson, Robert J Wood, and Gu-Yeon Wei. "Low power control IC for efficient high-voltage piezoelectric driving in a flying robotic insect". In: *VLSI Circuits (VLSIC), 2011 Symposium on*. IEEE. 2011, pp. 178–179.

[46] Brian G Kilberg, Daniel S Contreras, Joseph Greenspun, and Kristofer SJ Pister. "Mems aerodynamic control surfaces for millimeter-scale rockets". In: *Manipulation, Automation and Robotics at Small Scales (MARSS), 2017 International Conference on*. IEEE. 2017, pp. 1–5.

[47] Ilya Kolmanovsky and N Harris McClamroch. "Developments in nonholonomic control problems". In: *IEEE control systems* 15.6 (1995), pp. 20–36.

[48] Min Koo, Kwi-Il Park, Seung Hyun Lee, Minwon Suh, Duk Young Jeon, Jang Wook Choi, Kisuk Kang, and Keon Jae Lee. "Bendable inorganic thin-film battery for fully flexible electronic systems". In: *Nano letters* 12.9 (2012), pp. 4810–4816.

[49] Balthazar P Lechêne, Martin Cowell, Adrien Pierre, James W Evans, Paul K Wright, and Ana C Arias. "Organic solar cells and fully printed super-capacitors optimized for indoor light energy harvesting". In: *Nano Energy* 26 (2016), pp. 631–640.

[50] Chi Li, Matthew T Cole, Wei Lei, Ke Qu, Kai Ying, Yan Zhang, Alex R Robertson, Jamie H Warner, Shuyi Ding, Xiaobing Zhang, et al. "Highly electron transparent graphene for field emission triode gates". In: *Advanced Functional Materials* 24.9 (2014), pp. 1218–1227.

[51] Zhiwei Liu, Xiaojun Yan, Mingjing Qi, and Liwei Lin. "Electrostatic flapping wings with pivot-spar brackets for high lift force". In: *Micro Electro Mechanical Systems (MEMS), 2016 IEEE 29th International Conference on*. IEEE. 2016, pp. 1133–1136.

[52] Zhiwei Liu, Xiaojun Yan, Mingjing Qi, Yi Yang, Xiaoyong Zhang, and Liwei Lin. "Lateral moving of an artificial flapping-wing insect driven by low voltage electromagnetic actuator". In: *Micro Electro Mechanical Systems (MEMS), 2017 IEEE 30th International Conference on*. IEEE. 2017, pp. 777–780.

[53] JJ Lowke and F D'Alessandro. "Onset corona fields and electrical breakdown criteria". In: *Journal of Physics D: Applied Physics* 36.21 (2003), p. 2673.

[54] Robert Mahony, Vijay Kumar, and Peter Corke. "Multirotor aerial vehicles". In: *IEEE Robotics and Automation magazine* 20.32 (2012).

[55] RB Marcus, TS Ravi, T Gmitter, K Chin, D Liu, WJ Orvis, DR Ciarlo, CE Hunt, and J Trujillo. "Formation of silicon tips with¡ 1 nm radius". In: *Applied Physics Letters* 56.3 (1990), pp. 236–238.

[56] K. Masuyama and S. R. H. Barrett. "On the performance of electrohydrodynamic propulsion". In: *Proceedings of the Royal Society A: Mathematical, Physical and Engineering Sciences* 469.2154 (Apr. 2013), pp. 20120623–20120623. ISSN: 1364-5021, 1471-2946. DOI: 10.1098/rspa.2012.0623. URL: http://rspa.royalsocietypublishing.org/cgi/doi/10.1098/rspa.2012.0623 (visited on 09/27/2013).

[57] James Clerk Maxwell. *A treatise on electricity and magnetism*. Vol. 1. Clarendon press, 1881.

[58] Ankur M Mehta and Kristofer SJ Pister. "Warpwing: A complete open source control platform for miniature robots". In: *Intelligent Robots and Systems (IROS), 2010 IEEE/RSJ International Conference on*. IEEE. 2010, pp. 5169–5174.

[59] Veljko Milanovic, Lance Doherty, Dana A. Teasdale, Siavash Parsa, and Kristofer SJ Pister. "Micromachining technology for lateral field emission devices". In: *Electron Devices, IEEE Transactions on* 48 (1 2001), pp. 166–173. (Visited on 11/07/2013).

[60] Andrew Moiseff, Gerald S Pollack, and Ronald R Hoy. "Steering responses of flying crickets to sound and ultrasound: mate attraction and predator avoidance". In: *Proceedings of the National Academy of Sciences* 75.8 (1978), pp. 4052–4056.

[61] Nicolas Monrolin, Olivier Praud, and Franck Plouraboué. "Revisiting the positive DC corona discharge theory: Beyond Peek's and Townsend's law". In: *Physics of Plasmas* 25.6 (2018), p. 063503.

[62] Eric Moreau, Nicolas Benard, Jean-Daniel Lan-Sun-Luk, and Jean-Pierre Chabriat. "Electrohydrodynamic force produced by a wire-to-cylinder dc corona discharge in air at atmospheric pressure". In: *Journal of Physics D: Applied Physics* 46.47 (2013), p. 475204.

[63] Eric Moreau and Gerard Touchard. "Enhancing the mechanical efficiency of electric wind in corona discharges". In: *Journal of Electrostatics* 66.1 (2008), pp. 39–44.

[64] Yash Mulgaonkar, Michael Whitzer, Brian Morgan, Christopher M Kroninger, Aaron M Harrington, and Vijay Kumar. "Power and weight considerations in small, agile quadrotors". In: *Micro-and Nanotechnology Sensors, Systems, and Applications VI*. Vol. 9083. International Society for Optics and Photonics. 2014, 90831Q.

[65] GV Naidis. "Conditions for inception of positive corona discharges in air". In: *Journal of Physics D: Applied Physics* 38.13 (2005), p. 2211.

[66] *Nine-Axis MEMS MotionTracking Device, MPU-9250*. MPU-9250. TDK InverSense. Jan. 2014.

[67] TJ O'Hern and JR Torczynski. "Reynolds number dependence of the drag coefficient for laminar flow through fine-scale photoetched screens". In: *Experiments in fluids* 15.1 (1993), pp. 75–81.

[68] Andojo Ongkodjojo Ong, Alexis R Abramson, and Norman C Tien. "Electrohydrodynamic microfabricated ionic wind pumps for thermal management applications". In: *Journal of Heat Transfer* 136.6 (2014), p. 061703.

[69] Aminy E Ostfeld, Abhinav M Gaikwad, Yasser Khan, and Ana C Arias. "High-performance flexible energy storage and harvesting system for wearable electronics". In: *Scientific reports* 6 (2016).

[70] Frank William Peek. *Dielectric phenomena in high voltage engineering*. McGraw-Hill Book Company, Incorporated, 1920.

[71] Leonid Pekker and Marcus Young. "Model of ideal electrohydrodynamic thruster". In: *Journal of Propulsion and Power* 27.4 (2011), pp. 786–792.

[72] Darryll J Pines, J Sean Humbert, James E Hubbard, Evan R Ulrich, Imraan Faruque, and Jared Grauer. "Control model for robotic samara: Dynamics about a coordinated helical turn". In: *Journal of guidance, control, and dynamics* 33.6 (2010), pp. 1921–1927.

[73] Paul Pounds, Timothy Potie, Farid Kendoul, Surya Singh, Raja Jurdak, and Jonathan Roberts. "Automatic distribution of disposable self-deploying sensor modules". In: *Experimental Robotics*. Springer. 2016, pp. 535–543.

[74] Md Arafat Rahman, Xiaojian Wang, and Cuie Wen. "A review of high energy density lithium–air battery technology". In: *Journal of Applied Electrochemistry* 44.1 (2014), pp. 5–22.

[75] Glen C Rains, Jeffery K Tomberlin, and Don Kulasiri. "Using insect sniffing devices for detection". In: *Trends in biotechnology* 26.6 (2008), pp. 288–294.

[76] Myron Robinson. "A history of the electric wind". In: *American Journal of Physics* 30.5 (1962), pp. 366–372.

[77] Myron Robinson. "Movement of air in the electric wind of the corona discharge". In: *Transactions of the American Institute of Electrical Engineers, Part I: Communication and Electronics* 80.2 (1961), pp. 143–150.

[78] Louis A Rosenthal and Donald A Davis. "Electrical characterization of a corona discharge for surface treatment". In: *IEEE Transactions on Industry Applications* 3 (1975), pp. 328–335.

[79] Randall L Sandusky and Alexander Hölke. "High voltage capacitive voltage conversion". In: *2018 IEEE 30th International Symposium on Power Semiconductor Devices and ICs (ISPSD)*. IEEE. 2018, pp. 512–515.

[80] A. V. Shutov, I. V. Smetanin, A. A. Ionin, A. O. Levchenko, L. V. Seleznev, D. V. Sinitsyn, N. N. Ustinovskii, and V. D. Zvorykin. "Direct measurement of the characteristic three-body electron attachment time in the atmospheric air in direct current electric field". In: *Applied Physics Letters* 103 (3 July 16, 2013), p. 034106. ISSN: 0003-6951, 1077-3118. DOI: 10.1063/1.4813601. URL: http://scitation.aip.org/content/aip/journal/apl/103/3/10.1063/1.4813601 (visited on 12/06/2013).

[81] Milan Simek and Martin Clupek. "Efficiency of ozone production by pulsed positive corona discharge in synthetic air". In: *Journal of Physics D: Applied Physics* 35.11 (2002), p. 1171.

[82] Erik Steltz, M Seeman, Srinath Avadhanula, and Ronald S Fearing. "Power electronics design choice for piezoelectric microrobots". In: *Intelligent Robots and Systems, 2006 IEEE/RSJ International Conference on*. IEEE. 2006, pp. 1322–1328.

[83] M Tabrizchi, T Khayamian, and N Taj. "Design and optimization of a corona discharge ionization source for ion mobility spectrometry". In: *Review of scientific instruments* 71.6 (2000), pp. 2321–2328.

[84] K Takahashi, H Ishida, and K Sawada. "Vacuum-sealed microcavity formed from suspended graphene by using a low-pressure dry-transfer technique". In: *Applied Physics Letters* 112.4 (2018), p. 041901.

[85] R Tirumala, Y Li, DA Pohlman, and DB Go. "Corona discharges in sub-millimeter electrode gaps". In: *Journal of Electrostatics* 69.1 (2011), pp. 36–42.

[86] Arthur Mannering Tyndall and GC Grindley. "The mobility of ions in air.-Part I. Negative ions in moist air". In: *Proc. R. Soc. Lond. A* 110.754 (1926), pp. 341–358.

[87] Samuel Valdes, Ignacio Urza, Paul Pounds, and Surya Singh. "Samara: low-cost deployment for environmental sensing using passive autorotation". In: *Robotics: Science and Systems Workshop on Robotics for Environmental Monitoring*. Citeseer. 2012.

[88] Meta Virant-Doberlet and Andrej Cokl. "Vibrational communication in insects". In: *Neotropical Entomology* 33.2 (2004), pp. 121–134.

[89] Quang Vuhuu and RP Comsa. "Influence of gap length on wire-plane corona". In: *IEEE Transactions on Power Apparatus and Systems* 10 (1969), pp. 1462–1475.

[90] Hsiu-Che Wang, Nels E Jewell-Larsen, and Alexander V Mamishev. "Thermal management of microelectronics with electrostatic fluid accelerators". In: *Applied Thermal Engineering* 51.1 (2013), pp. 190–211.

[91] Michal Wojcik, Margaret Hauser, Wan Li, Seonah Moon, and Ke Xu. "Graphene-enabled electron microscopy and correlated super-resolution microscopy of wet cells". In: *Nature communications* 6 (2015), p. 7384.

[92] TKS Wong and SG Ingram. "Observational of Fowler-Nordheim tunnelling at atmospheric pressure using Au/Ti lateral tunnel diodes". In: *Journal of Physics D: Applied Physics* 26.6 (1993), p. 979.

[93] RJ Wood, S Avadhanula, E Steltz, M Seeman, J Entwistle, A Bachrach, G Barrows, S Sanders, and RS Fearing. "Design, fabrication and initial results of a 2g autonomous glider". In: *Industrial Electronics Society, 2005. IECON 2005. 31st Annual Conference of IEEE*. IEEE. 2005, 8–pp.

[94] Robert J Wood. "The first takeoff of a biologically inspired at-scale robotic insect". In: *IEEE transactions on robotics* 24.2 (2008), pp. 341–347.

[95] Robert J Wood, Ben Finio, Michael Karpelson, Kevin Ma, Nestor Osvaldo Perez-Arancibia, Pratheev S Sreetharan, Hiroto Tanaka, and John Peter Whitney. "Progress on picoair vehicles". In: *The International Journal of Robotics Research* 31.11 (2012), pp. 1292–1302.

[96] Haofeng Xu, Yiou He, Kieran L Strobel, Christopher K Gilmore, Sean P Kelley, Cooper C Hennick, Thomas Sebastian, Mark R Woolston, David J Perreault, and Steven RH Barrett. "Flight of an aeroplane with solid-state propulsion". In: *Nature* 563.7732 (2018), p. 532.

[97] T Yamamoto and HR Velkoff. "Electrohydrodynamics in an electrostatic precipitator". In: *Journal of Fluid Mechanics* 108 (1981), pp. 1–18.

[98] Lin Zhao and Kazimierz Adamiak. "EHD flow in air produced by electric corona discharge in pin–plate configuration". In: *Journal of electrostatics* 63.3-4 (2005), pp. 337–350.

[99] Yang Zou, Weiping Zhang, and Zheng Zhang. "Liftoff of an Electromagnetically Driven Insect-Inspired Flapping-Wing Robot". In: *IEEE Transactions on Robotics* 32.5 (2016), pp. 1285–1289.

Appendix A

Appendix A: The Meso-ionocraft Mask Collection

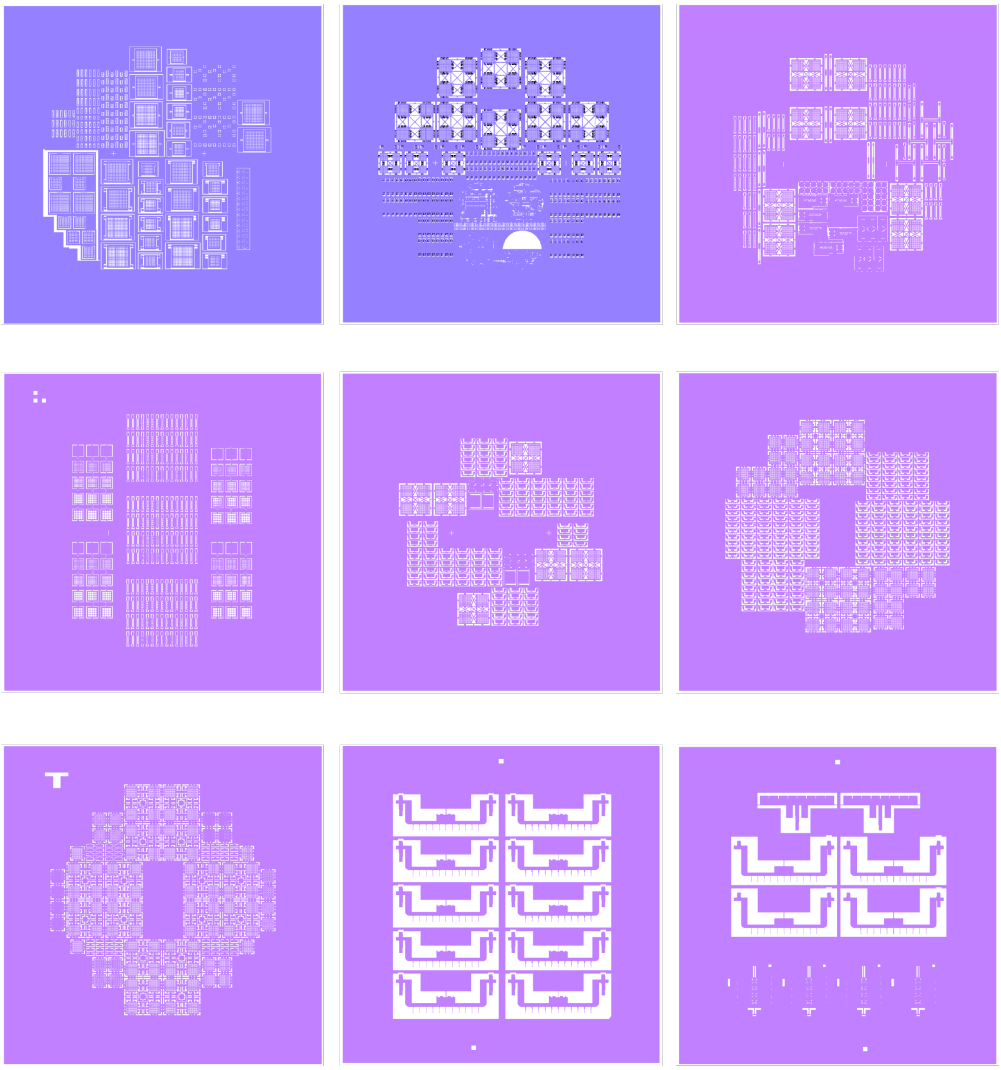

Figure A.1: Since a fateful meeting in Kris's office, where I decided to refocus from field emission devices and move back to meso-scale corona discharge based thrusters, I made fairly rapid progress. Here is the menagerie of photolithography masks (device-side only) that made it happen. Is it art?